bioRxiv preprint doi: https://doi.org/10.1101/2025.10.09.681382; this version posted October 10, 2025. The copyright holder for this preprint (which was not certified by peer review) is the author/funder, who has granted bioRxiv a license to display the preprint in perpetuity. It is made available under a CC-BY 4.0 International license.

Kinase KEY1 controls pyrenoid condensate size throughout the cell cycle by disrupting phase separation interactions

Authors:

Shan He[1,2,3,11], Linnea M. Lemma[2,4,11], Alejandro Martinez-Calvo[5,6,7], Guanhua He[1], Jessica H. Hennacy[1], Lianyong Wang[1,8], Sabrina L. Ergun[1,2], Ashwani K. Rai[1], Colton Wang[1], Luke Bunday[1], Angelo Kayser-Browne[1], Quan Wang[9,10], Clifford P. Brangwynne[2,4,7], Ned S. Wingreen[1,5,9]✉, Martin C. Jonikas[1,2,4]✉

[1]Department of Molecular Biology, Princeton University, Princeton, NJ 08544, USA

[2]Howard Hughes Medical Institute, Princeton University, Princeton, NJ 08544, USA

[3]Current address: Department of Botany, University of Wisconsin-Madison, Madison, WI 53706, USA

[4]Omenn-Darling Bioengineering Institute, Princeton University, Princeton, NJ 08544, USA

[5]Princeton Center for Theoretical Science, Princeton University, Princeton, NJ 08544, USA

[6]Department of Physics, Princeton University, Princeton, NJ 08544, USA

[7]Department of Chemical and Biological Engineering, Princeton University, Princeton, NJ 08544, USA

[8]Current address: Institute for Plant-Human Interface, Northeastern University, Boston, MA 02120, USA

[9]Lewis-Sigler Institute for Integrative Genomics, Princeton University, Princeton, NJ 08544, USA

[10]Current address: Laboratory of Chemical Physics, National Institute of Diabetes and Digestive and Kidney Diseases, National Institutes of Health, Bethesda, MD 20892, USA

[11]These authors contributed equally to this work: Shan He, Linnea Lemma

✉e-mail: mjonikas@princeton.edu, wingreen@princeton.edu

bioRxiv preprint doi: https://doi.org/10.1101/2025.10.09.681382; this version posted October 10, 2025. The copyright holder for this preprint (which was not certified by peer review) is the author/funder, who has granted bioRxiv a license to display the preprint in perpetuity. It is made available under a CC-BY 4.0 International license.

Abstract

Biomolecular condensates spatially organize cellular functions, but the regulation of their size, number, dissolution, and re-condensation is poorly understood. The pyrenoid, an algal biomolecular condensate that mediates one-third of global CO_2 fixation, typically exists as one large condensate per chloroplast, but during cell division it transiently dissolves and reconfigures into multiple smaller condensates. Here, we identify a kinase, KEY1, in the model alga *Chlamydomonas reinhardtii* that regulates pyrenoid condensate size and number dynamics throughout the cell cycle and is necessary for normal pyrenoid function and growth. Unlike wild type, *key1* mutant cells have multiple smaller condensates throughout the cell cycle that fail to dissolve during cell division. We show that KEY1 localizes to the condensates and promotes their dissolution by disrupting interactions between their core constituents, the CO_2-fixing enzyme Rubisco and its linker protein EPYC1, through EPYC1 phosphorylation. We develop a biophysical model that recapitulates KEY1-mediated condensate size and number regulation and suggests a mechanism for controlling condensate position. These data provide a foundation for the mechanistic understanding of the regulation of size, number, position, and dissolution in pyrenoids and other biomolecular condensates.

bioRxiv preprint doi: https://doi.org/10.1101/2025.10.09.681382; this version posted October 10, 2025. The copyright holder for this preprint (which was not certified by peer review) is the author/funder, who has granted bioRxiv a license to display the preprint in perpetuity. It is made available under a CC-BY 4.0 International license.

Main

In the past decade, the formation of biomolecular condensates has emerged as a ubiquitous principle by which cells colocalize proteins, RNA, and other biomolecules and enhance their functions[1-4]. Biomolecular condensates, such as the nucleolus[5], P granules[1], and purinosomes[6], facilitate diverse functions[7-20] from ribosome biogenesis[21] to metabolic regulation[22, 23]. Condensates form through liquid-liquid phase separation, a process by which cellular proteins and/or nucleic acids spontaneously assemble into droplets[2, 14, 24-27].

The size of condensates impacts biological function, as is particularly evident in the context of metabolic compartmentalization, where enzyme-containing condensates show maximal efficiency of metabolic reactions only in a specific range of sizes[28, 29]. Furthermore, aberrant condensate sizes are associated with disease, such as in the case of enlarged nucleoli in pancreatic cancer[30, 31].

Considering the impact of condensate size on function, there has been significant interest in understanding how condensate size is determined and regulated. The size distributions of some condensates appear to be passively governed by scaling laws[5, 32], surface tension[33, 34], or diffusion-limited dynamics[35]. Experimental studies show that the sizes of some condensates are regulated by the control of nucleation[36] or building-block availability[37] and synthesis[38], and the regulated one-time dissolution of many condensates is well established[39, 40].

Recently, theoretical mechanisms have been proposed for how cells could actively control condensate size by regulating the relative rates of dissolution and condensation[41-50]. While such active control of condensate size has been demonstrated in a synthetic system[51], it has not been clearly established to occur in living cells.

The pyrenoid is a large, singular biomolecular condensate[52] found in the chloroplast of eukaryotic algae[53, 54], where it mediates approximately one-third of global CO_2 assimilation[55]. The pyrenoid condensate tightly clusters the CO_2-fixing enzyme Rubisco[56] around a localized source

bioRxiv preprint doi: https://doi.org/10.1101/2025.10.09.681382; this version posted October 10, 2025. The copyright holder for this preprint (which was not certified by peer review) is the author/funder, who has granted bioRxiv a license to display the preprint in perpetuity. It is made available under a CC-BY 4.0 International license.

of CO_2, enhancing Rubisco's activity[57]. In the leading unicellular model alga *Chlamydomonas reinhardtii* (Chlamydomonas), the pyrenoid condensate is formed through multivalent interactions between Rubisco and the intrinsically disordered linker protein EPYC1 (Fig. 1a)[55, 58, 59]. Mutants that fail to condense a singular pyrenoid have growth defects under conditions that require efficient CO_2 delivery to Rubisco, including under ambient air[55, 59-62], making the pyrenoid one of the few condensates for which the functional significance of condensate formation is currently understood. During cell division, the size, number, dissolution, and re-condensation of pyrenoid condensates are highly dynamic and appear to be tightly regulated: the mother cell's single condensate rapidly dissolves and multiple smaller condensates appear before coarsening into a single condensate in each descendant cell[52]. However, the mechanisms regulating these behaviors remain unknown.

In this study, we use genetics, cell biology, *in vitro* reconstitution, and mathematical modeling to elucidate the biological and biophysical mechanisms underpinning the regulation of the pyrenoid condensate phase behaviors, including size and dissolution. We discover that a protein kinase, KEY1, regulates pyrenoid condensate size throughout the cell cycle and mediates the dissolution of the pyrenoid condensate during cell division. KEY1 functions in the condensate and is targeted to it via a common Rubisco-binding motif. KEY1 phosphorylates EPYC1 on its Rubisco binding sites, disrupting the Rubisco-EPYC1 interactions that drive phase separation. We show that the observed changes in pyrenoid size, number, and dissolution can be recapitulated with a minimal mathematical model of condensate regulation by kinase-driven protein fluxes. Our findings identify a central molecular regulator of pyrenoid phase behaviors and elucidate a mechanism for the regulation of size, number, and dissolution of condensates.

Results

The candidate protein kinase KEY1 physically interacts with EPYC1

bioRxiv preprint doi: https://doi.org/10.1101/2025.10.09.681382; this version posted October 10, 2025. The copyright holder for this preprint (which was not certified by peer review) is the author/funder, who has granted bioRxiv a license to display the preprint in perpetuity. It is made available under a CC-BY 4.0 International license.

During Chlamydomonas cell division, pyrenoid condensate dissolution and condensation each occur within 5-10 minutes[52], a timescale commonly associated with post-translational regulation[63, 64]. Moreover, several phosphopeptides of the Rubisco linker protein EPYC1 were previously identified through proteomics[65-68]. We therefore hypothesized that pyrenoid condensate phase behaviors are regulated at least in part through phosphorylation of EPYC1.

To test this hypothesis, we sought to identify the kinase that phosphorylates EPYC1. Our top candidate was Cre01.g008550 (Extended Data Fig. 1a), encoding a predicted dual-specificity protein kinase[69] that physically interacted with EPYC1 in a previous large-scale protein-protein interaction study[70]. Based on the results presented below, we name this kinase **K**inase of **E**P**Y**C1 (KEY1). We replicated the immunoprecipitation of KEY1 by EPYC1 (Fig. 1b) and also observed that EPYC1 co-precipitated with KEY1 when the latter was used as a bait (Fig. 1c; Supplementary Table 1), validating the physical interaction between KEY1 and EPYC1.

KEY1 is necessary for normal pyrenoid size, number, and function

To investigate whether KEY1 regulates phase behaviors of the pyrenoid condensate, we characterized two *key1* intron-insertion mutant alleles, which we refer to as *key1-1* and *key1-2*, that we obtained from the CLiP mutant library[71] (Chlamydomonas Resource Center IDs: LMJ.RY0402.107748 and LMJ.RY0402.168949, respectively; Extended Data Fig. 1b-h; Supplementary Table 2; Methods). *key1-1* had lower *KEY1* mRNA transcript abundance (~3% of wild type; Extended Data Fig. 1i) than *key1-2* (~70% of wild type). Using transmission electron microscopy, we observed more than one pyrenoid condensate in *key1-1* mutant cells, in contrast to the wild-type cells, which typically possessed a single condensate (Fig. 1d,e).

As transmission electron microscopy can only examine a thin slice of a cell, to enable accurate quantification of the size and number of pyrenoid condensates in each cell, we visualized the pyrenoid condensates through Venus-tagged Rubisco small subunit (RBCS1-Venus) in both wild-type cells and *key1-1* mutant cells[55, 72]. We observed that the *key1-1* mutant had multiple smaller

bioRxiv preprint doi: https://doi.org/10.1101/2025.10.09.681382; this version posted October 10, 2025. The copyright holder for this preprint (which was not certified by peer review) is the author/funder, who has granted bioRxiv a license to display the preprint in perpetuity. It is made available under a CC-BY 4.0 International license.

pyrenoid condensates in contrast to the singular large pyrenoid condensate that forms at the base of the cup-shaped chloroplast in wild-type cells (Fig. 1f,g; Supplementary Video 1). Reintroducing the *KEY1* gene under the endogenous *KEY1* promoter into the mutant background restored the singular large pyrenoid (Fig. 1h; Supplementary Video 1), establishing that the multiple-small-condensate phenotype was due to a disruption of *KEY1*.

On average, the *key1-1* mutant cells had more condensates per cell compared to the wild-type and rescued strain (Fig. 1i; $p < 10^{-6}$, *t*-test). The largest condensate was smaller on average in *key1-1* mutant cells than in wild-type or *key1-1;KEY1-SNAP*[73, 74] rescued cells (Fig. 1j; $p < 0.002$, *t*-test), and the distribution of the size of the largest condensate was broader, suggesting a defect in the regulation of pyrenoid size. These results establish that KEY1 is essential for normal pyrenoid condensate size and number.

To determine if KEY1 activity affected pyrenoid function, we performed a spot test growth assay. We found that compared to wild-type cells, the *key1-1* and *key1-2* mutant cells exhibited growth defects in Tris-Phosphate (TP) medium under low CO_2 (0.04%, air level) and very low CO_2 (0.004%) conditions, where cells require a functional pyrenoid in order to grow, but not under high CO_2 or on Tris-Acetate-Phosphate medium in the dark, where cells do not require a functional pyrenoid to grow[55, 75, 76] (Fig. 1k). These growth defects were partially rescued in the *key1-1* mutant after reintroducing the *KEY1* gene tagged with Venus-3×FLAG or SNAP-3×FLAG tags, driven by the endogenous *KEY1* promoter. The incomplete rescue at very low CO_2 could be due to the presence of the tags or due to suboptimal regulation since the constructs insert at random sites in the genome. Together, these results indicate that KEY1 is necessary for normal pyrenoid size, number, and function.

Pyrenoid dissolution and re-condensation often occur via a multiple-small-condensate intermediate

bioRxiv preprint doi: https://doi.org/10.1101/2025.10.09.681382; this version posted October 10, 2025. The copyright holder for this preprint (which was not certified by peer review) is the author/funder, who has granted bioRxiv a license to display the preprint in perpetuity. It is made available under a CC-BY 4.0 International license.

To understand how KEY1 controls the size and number of the pyrenoid condensate, we first investigated pyrenoid dynamics during cell division, when the pyrenoid rapidly dissolves and re-condenses, undergoing changes in size and number[52]. We observed cell division in wild-type cells whose cell cycles we synchronized using a diurnal light cycle in liquid photoautotrophic culture (Extended Data Fig. 2a; Methods)[77-79]. Under our growth conditions, at the transition from light to dark, each wild-type mother cell typically divided twice in rapid succession to produce four descendant cells. During this process, as we reported previously[52], the pyrenoid condensate of a given mother cell typically underwent two sequential dissolution and condensation cycles, dissolving before each chloroplast division and condensing shortly after (Fig. 2a-c; Extended Data Fig. 2b-d; Supplementary Videos 2,3). Both phase-separating components of the pyrenoid condensate exhibited highly correlated dissolution dynamics in wild-type cells, with each component fluorescently tagged (Supplementary Video 4).

Notably, we frequently observed that during dissolution of the major condensate, new, smaller condensates appeared elsewhere in the chloroplast and grew (Fig. 2b, Supplementary Video 2), which, as described in the modeling section below, we propose is a manifestation of an active biophysical system that regulates condensate size. After full dissolution, as previously described[52], we frequently observed the appearance of multiple small condensates that gradually ripened to yield one condensate per chloroplast (Fig. 2a,b; Supplementary Video 2).

KEY1 is necessary for pyrenoid size, number, and dissolution dynamics during cell division

During cell division, *key1-1* cells did not show any of the size, number, or dissolution dynamics we observed in wild-type cells. The condensate sizes and numbers in the *key1-1* mutant did not change appreciably over cell division (Fig. 2d-f; Supplementary Video 2). Moreover, the condensates of the *key1-1* mutant failed to dissolve during cell division, as evidenced by the lack of diffuse material in the stroma outside of the condensates when they were visualized by either

bioRxiv preprint doi: https://doi.org/10.1101/2025.10.09.681382; this version posted October 10, 2025. The copyright holder for this preprint (which was not certified by peer review) is the author/funder, who has granted bioRxiv a license to display the preprint in perpetuity. It is made available under a CC-BY 4.0 International license.

EPYC1-Venus (Fig. 2d-f; Supplementary Video 2) or Rubisco-Venus (Extended Data Fig. 2e-g; Supplementary Video 3). The wild-type pyrenoid condensate size, number, and dissolution dynamics were partially recovered in the *key1-1;KEY1-SNAP* rescue strain (Extended Data Fig. 2h-k); incomplete recovery could be due to non-native regulation of KEY1 or the presence of the SNAP tag and may explain the remaining growth defect of the *key1-1;KEY1-SNAP* at very low CO_2 (Fig. 1k). These results indicate that KEY1 is necessary for normal pyrenoid condensate size, number, and dissolution dynamics during cell division.

KEY1 suppresses the appearance of ectopic condensates during growth

Pre-division *key1-1* mutant chloroplasts typically contained more than four condensates, which were distributed among the descendant cells so that, on average, the number of condensates per cell decreased during cell division (Fig. 2d,e). This decrease in the number of condensates per cell during cell division indicates that the extra condensates observed in *key1-1* mutants must be produced during a different part of the diurnal growth cycle.

Indeed, we observed that small ectopic pyrenoid condensates formed in the chloroplast of the *key1-1* mutant cells during the light portion of the diurnal cycle and grew thereafter (Extended Data Fig. 3a,d,e; Supplementary Video 5). By contrast, in wild-type cells, the one condensate per cell grew during the light portion of the diurnal cycle[80] (Extended Data Fig. 3f), and we did not observe the appearance of such ectopic condensates (Extended Data Fig. 3b,c,g). Thus, our results indicate that ectopic condensates in the *key1-1* mutant appear during cell growth and KEY1 inhibits their formation in wild-type cells by either preventing nucleation or dissolving them while they are too small to be detected by microscopy (see also the Modeling section below).

KEY1 is necessary for EPYC1 phosphorylation

To understand how KEY1 regulates condensate size and suppresses ectopic condensates, we sought to characterize its molecular activity. We hypothesized that KEY1 phosphorylates EPYC1,

bioRxiv preprint doi: https://doi.org/10.1101/2025.10.09.681382; this version posted October 10, 2025. The copyright holder for this preprint (which was not certified by peer review) is the author/funder, who has granted bioRxiv a license to display the preprint in perpetuity. It is made available under a CC-BY 4.0 International license.

based on KEY1's annotation as a protein kinase[69], its co-precipitation with EPYC1 (Fig. 1b,c), and the previous observations of EPYC1 phosphopeptides[65-68].

To test if KEY1 is needed for EPYC1 phosphorylation, we investigated the phosphorylation state of EPYC1 in *key1* mutants using Phos-tag gels, which separate proteins based on their extent of phosphorylation[81, 82]. EPYC1 from the cell lysates of both *key1-1* and *key1-2* showed higher mobility than EPYC1 from wild-type cell lysate in a Phos-tag gel-based western blot (Fig. 3a). The *key1-1* mutant strain with constructs expressing KEY1 fused to a Venus or SNAP tag exhibited the lower-mobility EPYC1 bands observed in the wild type (Fig. 3a), indicating that the higher mobility of EPYC1 in the *key1-1* mutant is due to the absence of KEY1 activity in this strain. Phosphatase treatment caused the EPYC1 band from wild-type lysates to run with higher mobility similar to that in the *key1-1* mutant, confirming that the observed lower mobility of EPYC1 in wild type is due to phosphorylation (Fig. 3b). By contrast, phosphatase treatment of the *key1-1* lysate led to no observable shift in mobility, establishing that in the *key1-1* mutant EPYC1 has no detectable phosphorylation (Fig. 3b). Together, these observations indicate that KEY1 is necessary for EPYC1 phosphorylation *in vivo*.

We sought to determine whether the phenotypes of the *key1-1* mutant are due to deficient phosphorylation of EPYC1 specifically, as KEY1 may also phosphorylate other proteins in addition to EPYC1. We therefore transformed an *epyc1* mutant strain with a construct encoding a mutant EPYC1 where all the serines and threonines were changed to alanines (Extended Data Fig. 4a). In this *epyc1;EPYC1^{phosphonull}-Venus* line, wild-type KEY1 is still present and could still phosphorylate other potential targets, but it cannot phosphorylate the mutant EPYC1. We observed that this *epyc1;EPYC1^{phosphonull}* strain exhibited multiple EPYC1 condensates (Extended Data Fig. 4b-d) similar to the EPYC1 condensates of the *key1-1;EPYC1-Venus* strain (Fig. 1g), indicating that the multiple-pyrenoid phenotype in *key1-1* mutant cells is due to defects in EPYC1 phosphorylation. Together, our results so far indicate that KEY1 regulates pyrenoid size, number, and dynamics by directly or indirectly phosphorylating EPYC1.

bioRxiv preprint doi: https://doi.org/10.1101/2025.10.09.681382; this version posted October 10, 2025. The copyright holder for this preprint (which was not certified by peer review) is the author/funder, who has granted bioRxiv a license to display the preprint in perpetuity. It is made available under a CC-BY 4.0 International license.

KEY1 directly phosphorylates specific sites on EPYC1

To characterize KEY1's activity *in vitro*, we used purified KEY1 from *Escherichia coli* (*E. coli*) and insect cells (Extended Data Fig. 5a,b). This purified KEY1 was active, as treating the *key1-1* cell lysate with purified KEY1 caused EPYC1 to run at lower mobility similar to that observed in wild-type cells (Fig. 3b). To determine whether KEY1 can directly phosphorylate EPYC1, we incubated this purified KEY1 with purified EPYC1-tagged with GFP from *E. coli* in the presence of ATP[58, 83]. The KEY1-treated EPYC1 migrated more slowly on a Phos-tag gel than mock-treated EPYC1 (Fig. 3c and Extended Data Fig. 5c,d), indicating that KEY1 can directly phosphorylate EPYC1 *in vitro*.

Since the specific binding interface between EPYC1 and Rubisco is known[59], we wondered whether KEY1 phosphorylation impacts this interface. We used mass spectrometry to determine the phosphorylation sites on EPYC1-Venus-3×FLAG purified from unsynchronized cells with a wild-type background (Fig. 3d). The results identified 13 distinct phosphorylated EPYC1 peptides. Because EPYC1 is a repeat protein, some of these peptides align onto multiple sites of the EPYC1 sequence; thus, our data indicate that up to 24 serines or threonines on EPYC1 are phosphorylated. Thirteen of the phosphorylated EPYC1 residues were on or directly adjacent to the Rubisco-binding regions (Fig. 3d)[59], suggesting that phosphorylation of EPYC1 could impact EPYC1-Rubisco binding.

When we phosphorylated purified EPYC1-GFP from *E. coli in vitro* with 3 μM purified KEY1 (Extended Data Fig. 5d), we observed a similar pattern of phosphorylation (Fig. 3e,g) to what we had observed on EPYC1 phosphorylated *in vivo* (Fig. 3d), indicating that KEY1 can directly phosphorylate nearly all of the sites observed to be phosphorylated *in vivo*. When we treated EPYC1-GFP *in vitro* with a lower (115 nM) concentration of KEY1 (Extended Data Fig. 5d), we observed preferential phosphorylation at sites in the Rubisco-binding region (Fig. 3f,g). For peptides where we observed both unphosphorylated and phosphorylated variants, the proportion

bioRxiv preprint doi: https://doi.org/10.1101/2025.10.09.681382; this version posted October 10, 2025. The copyright holder for this preprint (which was not certified by peer review) is the author/funder, who has granted bioRxiv a license to display the preprint in perpetuity. It is made available under a CC-BY 4.0 International license.

of phosphorylated variants increased with the concentration of KEY1 (Fig. 3h,i). Together with the observed lack of EPYC1 phosphorylation in the *key1* mutants (Fig. 3a,b), these results establish that KEY1 is the primary kinase of EPYC1 *in vivo* and suggest that KEY1 preferentially phosphorylates the Rubisco-binding regions of EPYC1.

The extent of EPYC1 phosphorylation changes diurnally

If the phosphorylation of EPYC1 by KEY1 underlies the dynamic diurnal phase behaviors of the pyrenoid condensate, we would expect the extent of EPYC1 phosphorylation to change over the course of the diurnal cycle. Indeed, we observed diurnal changes in the extent of EPYC1 phosphorylation in cells grown in a 12h light:12h dark cycle (Fig. 3j,k). EPYC1 was minimally phosphorylated from the middle of the night through the early morning (hours 18 through 2 of the cycle), with a single high-mobility band. During the day from mid-morning to dusk (hours 3 through 12) EPYC1 was phosphorylated at intermediate levels, with both high- and low-mobility species. At the beginning of the night (hours 13 and 14 of the cycle), the phosphorylation level reached its maximum, with a single low-mobility band. We speculate that these diurnal changes in the extent of EPYC1 phosphorylation reflect a lower level of phosphorylation needed to dissolve ectopic condensates during growth during the day (hours 3 through 12; Fig. 3k) and a higher level of phosphorylation needed to dissolve the pyrenoid condensate during cell division (hours 13 and 14; Fig. 3k).

The two diurnal increases in the extent of EPYC1 phosphorylation (at hours 3 and 13) were each preceded by a peak in *KEY1* mRNA levels measured in a previous study: one in the early morning (hour 0.5) and the other at the end of the day (hour 11, Fig. 3l)[79], This observation suggests that transient increases in *KEY1* mRNA may result in increases in total KEY1 activity, which could contribute to the observed changes in the EPYC1 phosphorylation extent.

bioRxiv preprint doi: https://doi.org/10.1101/2025.10.09.681382; this version posted October 10, 2025. The copyright holder for this preprint (which was not certified by peer review) is the author/funder, who has granted bioRxiv a license to display the preprint in perpetuity. It is made available under a CC-BY 4.0 International license.

KEY1-phosphorylated EPYC1 promotes the dissolution of Rubisco-EPYC1 condensates *in vitro*

The requirement of KEY1 for pyrenoid condensate dissolution during cell division (Fig. 2; Extended Data Fig. 2) and the observation that KEY1 is the primary kinase of EPYC1 (Fig. 3a-i) suggested that phosphorylated EPYC1 promotes pyrenoid condensate disassembly. To test this idea, we used a previously-established assay that uses microscopy to look for the formation of phase-separated condensates by Chlamydomonas-purified Rubisco and *E. coli*-purified EPYC1-GFP[58, 83]. We measured the *in vitro* phase diagrams of Chlamydomonas Rubisco combined with mock-treated or KEY1-phosphorylated EPYC1-GFP (Fig. 4a-d). Our mock-treated EPYC1-GFP was minimally phosphorylated (Fig. 3c,g; Extended Data Fig. 5d) and formed condensates in agreement with our previous study (Fig. 4c)[83]. By contrast, EPYC1-GFP treated with KEY1 did not phase separate at any tested concentration (Fig. 4d). We conclude that phosphorylation of EPYC1 by KEY1 promotes the dissolution of Rubisco-EPYC1 condensates.

Phosphorylation of EPYC1 by KEY1 disrupts EPYC1 binding to Rubisco

We next sought to determine how EPYC1 phosphorylation promotes dissolution of the Rubisco-EPYC1 condensate. Our previous study determined that small complexes can form between an individual Rubisco and one or more EPYC1 molecules in the dilute phase (Fig. 4e)[83]. Thus, one possibility is that EPYC1 phosphorylation could promote the formation of such small Rubisco-EPYC1 complexes (Fig. 4e, Hypothesis 1), which would inhibit the interaction network required for condensation[52, 83, 84]. An alternative hypothesis is that EPYC1 phosphorylation could favor dissolution of the condensate by disrupting binding between EPYC1 and Rubisco (Fig. 4e, Hypothesis 2).

To distinguish between these two hypotheses, we studied the effect of phosphorylation on EPYC1 binding to Rubisco in the dilute phase using Fluorescence Correlation Spectroscopy[83] (Methods). In this assay, the binding of EPYC1-GFP (60 kDa) to Rubisco (550 kDa) can be

bioRxiv preprint doi: https://doi.org/10.1101/2025.10.09.681382; this version posted October 10, 2025. The copyright holder for this preprint (which was not certified by peer review) is the author/funder, who has granted bioRxiv a license to display the preprint in perpetuity. It is made available under a CC-BY 4.0 International license.

298 detected as a decrease in the diffusion coefficient of EPYC1-GFP[83]. The diffusion coefficient of
299 unphosphorylated EPYC1-GFP decreased from 60 $\mu m^2/s$ to 41 $\mu m^2/s$ when Rubisco was added
300 (Fig. 4f), indicating that EPYC1 and Rubisco bound and formed small Rubisco-EPYC1
301 complexes, as expected from previous findings[83]. However, when we repeated the experiment
302 with KEY1-phosphorylated EPYC1-GFP, we observed no change in the diffusion coefficient of
303 EPYC1 when Rubisco was added, indicating no formation of small Rubisco-EPYC1 complexes
304 (Fig. 4f). Taken together, these findings show that KEY1 phosphorylation of EPYC1 directly
305 disrupts the binding between Rubisco and EPYC1 to favor condensate dissolution (Fig. 4e,
306 Hypothesis 2).
307
308 **Phosphorylated EPYC1 is enriched in the dilute phase *in vivo***
309 Further consistent with our observations, we found that *in vivo*, unphosphorylated EPYC1 is
310 enriched in the pyrenoid condensate, while phosphorylated EPYC1 is enriched in the dilute phase.
311 We mechanically lysed unsynchronized wild-type cells and centrifuged the cell lysate to separate
312 the pyrenoid condensate in the pellet from the dilute phase in the supernatant (Fig. 4g)[58, 70]. We
313 observed an enrichment of unphosphorylated EPYC1 in the pellet, to which the pyrenoid
314 condensate fractionates[55, 58], whereas we observed an enrichment of phosphorylated EPYC1 in
315 the soluble supernatant (Fig. 4g). This result suggests that KEY1-phosphorylated EPYC1
316 partitions into the dilute phase.
317
318 **KEY1 localizes to the pyrenoid condensates throughout the cell cycle**
319 Depending on where KEY1 localizes, the kinase could be acting to influence the size, number,
320 and dissolution of the pyrenoid condensates via fundamentally different biophysical mechanisms:
321 1) KEY1 could localize to the dilute phase—throughout the chloroplast stroma outside the
322 pyrenoid condensate—to directly control the amount of phosphorylated EPYC1; 2) KEY1 could
323 relocalize from the dilute phase to the condensate specifically during cell division, to induce

bioRxiv preprint doi: https://doi.org/10.1101/2025.10.09.681382; this version posted October 10, 2025. The copyright holder for this preprint (which was not certified by peer review) is the author/funder, who has granted bioRxiv a license to display the preprint in perpetuity. It is made available under a CC-BY 4.0 International license.

dissolution at that time; 3) KEY1 could localize to the condensate at all times and induce dissolution through changes in concentration or activity. To distinguish these mechanisms, we investigated the dynamic subcellular localization of KEY1. In unsynchronized cultures, KEY1-SNAP localized to the pyrenoid and sometimes also to the pyrenoid periphery (Fig. 5a). In synchronized cultures, we found that fluorescently tagged KEY1 localizes to the pyrenoid condensate throughout the cell cycle (Extended Data Fig. 6). Its persistent localization to the condensate suggests that KEY1 regulates pyrenoid dissolution and re-condensation not through changes in its localization but instead through temporal changes in its concentration and/or activity.

A Rubisco-binding motif localizes KEY1 to condensates and is necessary for function

We hypothesized that KEY1 is targeted to the condensate by its predicted N-terminal Rubisco-binding motif (Fig. 5b,c; Supplementary Video 6)[85]. Many pyrenoid-localized proteins, including EPYC1, possess a common Rubisco-binding motif[85]. This motif was previously found to be necessary for targeting a pyrenoid-resident protein to the pyrenoid and was sufficient for enriching a chloroplast stromal protein in the pyrenoid[85]. To determine if KEY1's predicted Rubisco-binding motif can bind to Rubisco, we tested whether a peptide containing this motif could bind to Rubisco using a surface plasmon resonance assay. We detected binding, indicating that KEY1 contains a bona fide Rubisco-binding motif that could potentially contribute to KEY1's localization to the pyrenoid condensate (Fig. 5d; Extended Data Fig. 7).

To test whether the motif was necessary for KEY1's localization, we expressed KEY1-SNAP with a mutated Rubisco-binding motif in the *key1-1* mutant strain expressing RBCS1-Venus (Fig. 5a). In this *key1-1;RBCS1-Venus;KEY1$^{\Delta RBM}$-SNAP* strain, KEY1$^{\Delta RBM}$ signal did not partition into the pyrenoid condensates, indicating that the Rubisco-binding motif is necessary for KEY1 localization to the pyrenoid condensates (Fig. 5a; Extended Data Fig. 8a-e).

bioRxiv preprint doi: https://doi.org/10.1101/2025.10.09.681382; this version posted October 10, 2025. The copyright holder for this preprint (which was not certified by peer review) is the author/funder, who has granted bioRxiv a license to display the preprint in perpetuity. It is made available under a CC-BY 4.0 International license.

To determine whether the localization of KEY1 affects its kinase activity on EPYC1, we analyzed EPYC1 phosphorylation in the *key1-1;RBCS1-Venus;KEY1$^{\Delta RBM}$-SNAP* strain. In this strain, we observed decreased phosphorylation of EPYC1 relative to the control expressing KEY1 with a wild-type Rubisco-binding motif (Fig. 5e). Consistent with the decreased phosphorylation of EPYC1, the multiple-pyrenoid phenotype was not rescued in this strain (Fig. 5a; Extended Data Fig. 8f). To verify that this mutation did not substantially impact KEY1's kinase activity, we confirmed that KEY1$^{\Delta RBM}$ is still able to phosphorylate EPYC1 (Extended Data Fig. 8g). These results indicate that correct localization of KEY1 is needed for its normal activity in phosphorylating EPYC1 and maintaining a singular pyrenoid condensate.

Taking sum of our experimental data, we propose a model for KEY1's regulation of EPYC1 phosphorylation and its partitioning between the condensed and dilute phase (Fig. 5f). Unphosphorylated EPYC1 forms condensates with Rubisco. A Rubisco-binding motif localizes KEY1 to the pyrenoid condensate throughout the cell cycle, where it phosphorylates EPYC1, decreasing its binding affinity to Rubisco and promoting its partitioning to the dilute phase. We speculate that at least one unidentified phosphatase acts on EPYC1 in the dilute phase, promoting its partitioning into the condensate. While the identification of such a phosphatase is beyond the scope of the present study, evidence supporting its potential existence includes the presence of low-phosphorylation EPYC1 species at various time points during the diurnal cycle (Fig. 3k) and the rapid re-condensation of the pyrenoid condensate after cell division (Fig. 2a-c; Supplementary Videos 2,3).

Modeling suggests potential mechanisms underpinning KEY1 regulation of pyrenoid size, positioning, and phase dynamics

We sought to understand how the local molecular interactions of EPYC1, KEY1, and the putative EPYC1 phosphatase could produce the observed pyrenoid condensate size and number dynamics. We hypothesized that the molecular interactions between these components could

bioRxiv preprint doi: https://doi.org/10.1101/2025.10.09.681382; this version posted October 10, 2025. The copyright holder for this preprint (which was not certified by peer review) is the author/funder, who has granted bioRxiv a license to display the preprint in perpetuity. It is made available under a CC-BY 4.0 International license.

produce an active system with the emergent property of size control through the previously-theorized enrichment-inhibition mechanism[41]. In this mechanism, a kinase localizes to the condensate and converts its building blocks into a dissolution-promoting form (in our case, phosphorylated EPYC1), while a phosphatase localized to the dilute phase converts the building blocks into a condensation-promoting form (in our case, unphosphorylated EPYC1), resulting in a stable condensate size determined by the ratio of kinase to phosphatase activities.

To investigate this hypothesis, we developed a minimal continuum mathematical model of pyrenoid condensate dynamics. For simplicity, we represented the EPYC1-Rubisco system through EPYC1 only, capturing the propensity of unphosphorylated EPYC1 to cluster via interaction with Rubisco as an effective self-interaction (Methods). Specifically, we considered a suspension of EPYC1 in a solvent, where EPYC1 can exist in two states: 1) unphosphorylated EPYC1, which we denote as *sticky*, and 2) phosphorylated EPYC1, which we denote as *non-sticky* (Fig. 6a). Sticky EPYC1 tends to condense via self-attractive interactions and form clusters. Non-sticky EPYC1 does not condense and thus tends to dissolve the clusters, favoring a configuration where EPYC1 is uniformly dispersed. The diffusive fluxes of sticky and non-sticky EPYC1 are driven by gradients of their chemical potentials, which we obtained from Flory-Huggins free energies (Methods).

To model the phosphorylation of EPYC1 by KEY1, we introduced a rate of switching from sticky to non-sticky EPYC1. We also included a rate of switching from non-sticky to sticky while holding the total amount of EPYC1 constant, to simulate the activity of the unidentified phosphatase (Fig. 6a). For simplicity, we assumed that these switching rates are spatially uniform and depend only on time—e.g., to model changes of KEY1 levels during the cell cycle. Thus, our model is simpler than the enrichment-inhibition mechanism[41] in which switching rates vary in space due to spatial variations of kinase and phosphatase concentrations. We also assumed that the diffusion coefficients of both sticky and non-sticky EPYC1 are equal and constant (Methods). Thus, in this minimal model, for a fixed amount of EPYC1 with a fixed self-attractive interaction

bioRxiv preprint doi: https://doi.org/10.1101/2025.10.09.681382; this version posted October 10, 2025. The copyright holder for this preprint (which was not certified by peer review) is the author/funder, who has granted bioRxiv a license to display the preprint in perpetuity. It is made available under a CC-BY 4.0 International license.

401 strength, the dimensionless parameters controlling the phase behaviors of EPYC1 are the ratio
402 between kinase and phosphatase activities and the ratio between the switching times and the
403 time for EPYC1 to diffuse over the chloroplast (Methods).

404 We performed numerical simulations in a two-dimensional geometry with no-flux boundaries,
405 mimicking the shape of the Chlamydomonas chloroplast (Methods, Supplementary Videos 7-13).
406 Additionally, we conducted simulations using a square geometry with periodic conditions and
407 obtained similar results (Supplementary Video 14; Methods).

408 ***Dissolution, re-condensation, and size control during cell division:*** We first sought to
409 determine whether this simple model could recapitulate the observed phase behaviors of the
410 pyrenoid condensate during cell division. From the peak in *KEY1* mRNA expression immediately
411 preceding cell division (Fig. 3l)[79] and EPYC1 phosphorylation during cell division (Fig. 3k, hours
412 13-14), we speculated that KEY1 activity increases leading up to cell division and declines
413 thereafter. Thus, in the model we varied the kinase activity, i.e., the switching rate from sticky to
414 non-sticky, following this inferred pattern (Fig. 6b). We observed that an initially stable large
415 condensate fully dissolved, and eventually re-condensed again into a singular condensate (Fig.
416 6c; Supplementary Video 7), recapitulating what we observed *in vivo* (Fig. 2a-c). These results
417 support the idea that the observed dissolution and condensation during cell division could be
418 driven by changes in the EPYC1 phosphorylation/dephosphorylation rate.

419 Importantly, as observed *in vivo* (Fig. 2a,b), the dissolution and re-condensation each
420 proceeded via intermediates that contained multiple smaller condensates (Fig. 6c-ii,iv,v and
421 Supplementary Video 7), which we propose to be the manifestation of the EPYC1-KEY1-
422 phosphatase system acting as a condensate size regulation mechanism. A state of multiple stable
423 condensates has been observed theoretically in previous models of active condensates and
424 experimentally in reactive mixtures, where the presence of nonequilibrium chemical reactions
425 between system components can suppress coarsening[41-47, 51, 86]. In our system, competing kinase
426 and phosphatase activities establish a preferred condensate radius where the flux of non-sticky

bioRxiv preprint doi: https://doi.org/10.1101/2025.10.09.681382; this version posted October 10, 2025. The copyright holder for this preprint (which was not certified by peer review) is the author/funder, who has granted bioRxiv a license to display the preprint in perpetuity. It is made available under a CC-BY 4.0 International license.

EPYC1 out of each condensate (roughly ~R^3) balances the flux of sticky EPYC1 into each condensate (roughly ~R) (Fig. 6d; Supplementary Video 8; Methods)[41]. The exact value of this preferred radius is determined by EPYC1 diffusivity and kinase/phosphatase activity ratio (Methods). Leading up to cell division, the kinase/phosphatase activity ratio increases, progressively decreasing the preferred condensate radius and causing the system to favor states with multiple smaller condensates before EPYC1 is fully dissolved (Fig. 6c-iv,d-ii; Supplementary Video 7). Specifically, as the initial single condensate shrinks toward the smaller preferred radius, the efflux of EPYC1 from this condensate leads to the buildup of a high concentration of EPYC1 away from the condensate, which is converted to the sticky form by the phosphatase. Once the concentration of sticky EPYC1 in the dilute phase is sufficiently high, a new condensate forms by spinodal decomposition. Following cell division, as KEY1 activity decreases, the preferred condensate radius progressively increases, ultimately causing the system to coarsen into a single condensate via Ostwald ripening (Extended Data Fig. 9). As a consequence of kinase and phosphatase activities, the distribution of sticky EPYC1 both inside and outside the condensates is spatially nonuniform—a signature of active systems (Fig. 6d-i,ii)[46]. Thus, our findings suggest that pyrenoid dynamics and size control are consequences of the system being active, with energy injected via phosphorylation/dephosphorylation reactions.

Self-centering and inter-condensate repulsion: In our minimal model, as a consequence of the active mechanism described above, we observed additional intriguing behaviors of the condensates that might be biologically relevant. Specifically, we found that the fluxes of molecules due to kinase and phosphatase activity can cause the condensate to self-center within the boundaries of the simulation (Fig. 6c-vi; Supplementary Video 7). To see this phenomenon clearly, we initialized a singular condensate in the arm of the chloroplast (Fig. 6e; Supplementary Video 9). Over time, the condensate moved to the center of the chloroplast. In contrast, without kinase and phosphatase activity, the condensate remained in the arm of the chloroplast over the same timescale (Supplementary Video 10). Strikingly, the position favored by the active model

bioRxiv preprint doi: https://doi.org/10.1101/2025.10.09.681382; this version posted October 10, 2025. The copyright holder for this preprint (which was not certified by peer review) is the author/funder, who has granted bioRxiv a license to display the preprint in perpetuity. It is made available under a CC-BY 4.0 International license.

matches the *in vivo* position of the pyrenoid condensate in the chloroplast (Fig. 1d,f; Fig. 6e). This result suggests that KEY1-driven phosphorylation of EPYC1 may contribute to proper pyrenoid localization within the chloroplast.

We also observed that our simulated condensates appeared to repel each other. Indeed, when we initialized two condensates close together with a finite phosphorylation rate, we saw them move away from each other such that they were eventually evenly spaced within the chloroplast geometry (Fig. 6f; Supplementary Video 11). In the model, the self-centering and repulsive phenomena are due to the same underlying mechanism: phosphorylated, non-sticky EPYC1 departs a condensate symmetrically, but after diffusion and dephosphorylation within the confining geometry, the influx of sticky EPYC1 is highest from the side of the condensate farthest from the chloroplast boundaries or from other condensates. This mechanism for condensate interactions may extend to other regulated biomolecular condensates.

Dissolution of ectopic condensates: Finally, we also explored whether our minimal model could recapitulate the observed suppression of small ectopic clusters mediated by KEY1 activity, as compared to mutant cells lacking KEY1 which cannot dissolve them (Extended Data Fig. 3b-e). To this end, we considered that the absence of KEY1 not only implies negligible switching of EPYC1 to a non-sticky state, but also leads to anomalously low EPYC1 phosphorylation, thus increasing the EPYC1-EPYC1 self-attraction strength (Methods, Mathematical Model: Model parameter values). The presence of KEY1 at low activity leads to the dissolution of a small ectopic cluster (Fig. 6g; Supplementary Video 12), whereas in the absence of KEY1, EPYC1 self-interactions are too strong to allow the dissolution of the ectopic cluster within the same time window (Extended Data Fig. 9; Supplementary Video 13). These results support the idea that a low level of KEY1 activity could mediate the dissolution of ectopic condensates during cell growth to maintain a single pyrenoid and can explain the origin of the ectopic condensates that lack size control in the *key1-1* mutant (Extended Data Fig. 3b-e).

bioRxiv preprint doi: https://doi.org/10.1101/2025.10.09.681382; this version posted October 10, 2025. The copyright holder for this preprint (which was not certified by peer review) is the author/funder, who has granted bioRxiv a license to display the preprint in perpetuity. It is made available under a CC-BY 4.0 International license.

Thus, while the multiple condensates exhibited by the *key1-1* mutant resemble the multiple condensates seen during cell division in wild-type cells, they arise by distinct mechanisms. The multiple condensates exhibited by the *key1-1* mutant result from the effective absence of Ostwald ripening as new material is added to the system, whereas the multiple condensates seen during cell division in wild-type cells result from an active size control mechanism mediated by KEY1 (Fig. 6h).

Discussion

In this study, we identified a protein kinase, KEY1, that regulates the size and dissolution of the pyrenoid condensate in Chlamydomonas. KEY1 phosphorylates the Rubisco linker protein EPYC1, inhibiting EPYC1's interaction with Rubisco and promoting the dissolution of the pyrenoid condensate. KEY1 localizes to the condensate throughout the cell cycle, and this localization is mediated by a Rubisco-binding motif that is necessary for its localization and function.

Our modeling and experimental results suggest mechanisms by which KEY1 regulates condensate size, number, and dissolution. Our data are consistent with KEY1 being a central player in an active condensate size control system where the condensate size setpoint is inversely related to the ratio of KEY1 activity to phosphatase activity (Fig. 6h). In wild-type cells during the growth phase of the cell cycle, relatively low KEY1 activity sets the pyrenoid condensate size setpoint to "large", favoring a single large condensate and suppressing ectopic condensates. During cell division, an increase in KEY1 activity transiently decreases the condensate size setpoint, favoring a progression to multiple small condensates and complete dissolution. After cell division, a return to lower KEY1 activity again favors a single large condensate. In the absence of KEY1, cells lack an effective pyrenoid condensate size regulation mechanism, resulting in the appearance and persistence of ectopic condensates, aberrant condensate size, and the failure to dissolve the pyrenoid condensate during cell division.

bioRxiv preprint doi: https://doi.org/10.1101/2025.10.09.681382; this version posted October 10, 2025. The copyright holder for this preprint (which was not certified by peer review) is the author/funder, who has granted bioRxiv a license to display the preprint in perpetuity. It is made available under a CC-BY 4.0 International license.

While kinases are known to promote the dissolution of various biomolecular condensates[87-91], the molecular mechanisms connecting phosphorylation to dissolution remain poorly understood. Our identification of KEY1, characterization of its physical interactions with Rubisco and the sites it phosphorylates on EPYC1, and analysis of the impact of EPYC1 phosphorylation on its binding to Rubisco contributes a system where the molecular basis by which a kinase promotes a condensate's dissolution is known.

Our work also advances the broader understanding of the regulation of condensate size, number, and position. The examples proposed to date to potentially represent active regulation of condensate size by the enrichment-inhibition mechanism[41] — MBK-2 in P granules[87], DYRK3 in stress granules[88], the CLK kinase in nuclear speckles[89], Cdk2 in Cajal Bodies[90], and CaMKII in synapsin condensates[91] — could all be cases where the kinase acts at one time to disassemble the condensate rather than participating in active size regulation. Here we show that the pyrenoid condensate system exhibits all the hallmarks of genuine size regulation previously expected from an active size-control mechanism[41]: 1) the key pyrenoid condensate protein, EPYC1, is phosphorylated by a kinase; 2) kinase activity dissolves the condensate; 3) the kinase is localized to the condensate throughout the cell cycle. In addition to meeting these previously-established criteria, we find that the pyrenoid condensate system exhibits two other properties that we propose are also hallmarks of active size control: 4) there is a basal level of EPYC1 phosphorylation during steady-state growth; and 5) increases in kinase activity lead to a decrease in condensate size concomitant with an increase in condensate number. We also observe, unexpectedly, that the absence of regulation by the kinase leads to the appearance of ectopic mislocalized condensates, suggesting that the same kinase-based condensate size regulation is leveraged to suppress ectopic condensates during cell growth. Finally, our modeling and experimental observations suggest that the same kinase and phosphatase activity can also contribute to the centering of condensates within cellular compartments and inter-condensate repulsion. Together, our results advance the understanding of the regulation of condensate size,

bioRxiv preprint doi: https://doi.org/10.1101/2025.10.09.681382; this version posted October 10, 2025. The copyright holder for this preprint (which was not certified by peer review) is the author/funder, who has granted bioRxiv a license to display the preprint in perpetuity. It is made available under a CC-BY 4.0 International license.

number, and position and establish the pyrenoid condensate as a promising experimental model system for further studies of these behaviors, including the possibility of their eventual *in vitro* reconstitution.

Author contributions

S.H., L.M.L, and M.C.J. conceived the project. A.M.C. and N.S.W. conceived the mathematical model. L.W. performed immunoprecipitation experiments and mass spectrometry, S.H. performed analysis. S.H. performed genetic analysis of *key1-1* and *key1-2* mutants. A.K.R performed RT-qPCR. J.H.H. performed the transmission electron microscopy. S.H. performed or designed plasmid construction and cloning, and generated Chlamydomonas strains by mating or transformation. L.M.L., C.W., A.K.B., and S.H. performed confocal microscopy and analysis. L.M.L. and S.H. performed spot test experiment. L.M.L. expressed and purified EPYC1-GFP and extracted Rubisco. G.H. expressed and purified 6xHis-EPYC1. S.H. and L.M.L supervised the expression and purification project for KEY1 and KEY1$^{\Delta RBM}$. S.H. and S.L.E. performed immunoblotting analyses for EPYC1 phosphorylation status. L.M.L. and S.H. prepared samples and performed analysis to identify the phosphorylation sites on EPYC1 mediated by KEY1. L.M.L., S.H., C.W., and L.B. collected diurnal cell samples for western blot experiments. L.M.L. performed *in vitro* phase separation experiments. G.H., Q.W., and L.M.L. performed fluorescence correlation spectroscopy experiments and analysis. S.H. analyzed the sequence of KEY1 and predicted its structure with AlphaFold2. S.H. performed surface plasmon resonance experiment. A.M.C. performed simulations and theoretical analyses. S.H., L.M.L., A.M.C., C.P.B., N.S.W., and M.C.J. guided the research and wrote the manuscript with input from all authors.

bioRxiv preprint doi: https://doi.org/10.1101/2025.10.09.681382; this version posted October 10, 2025. The copyright holder for this preprint (which was not certified by peer review) is the author/funder, who has granted bioRxiv a license to display the preprint in perpetuity. It is made available under a CC-BY 4.0 International license.

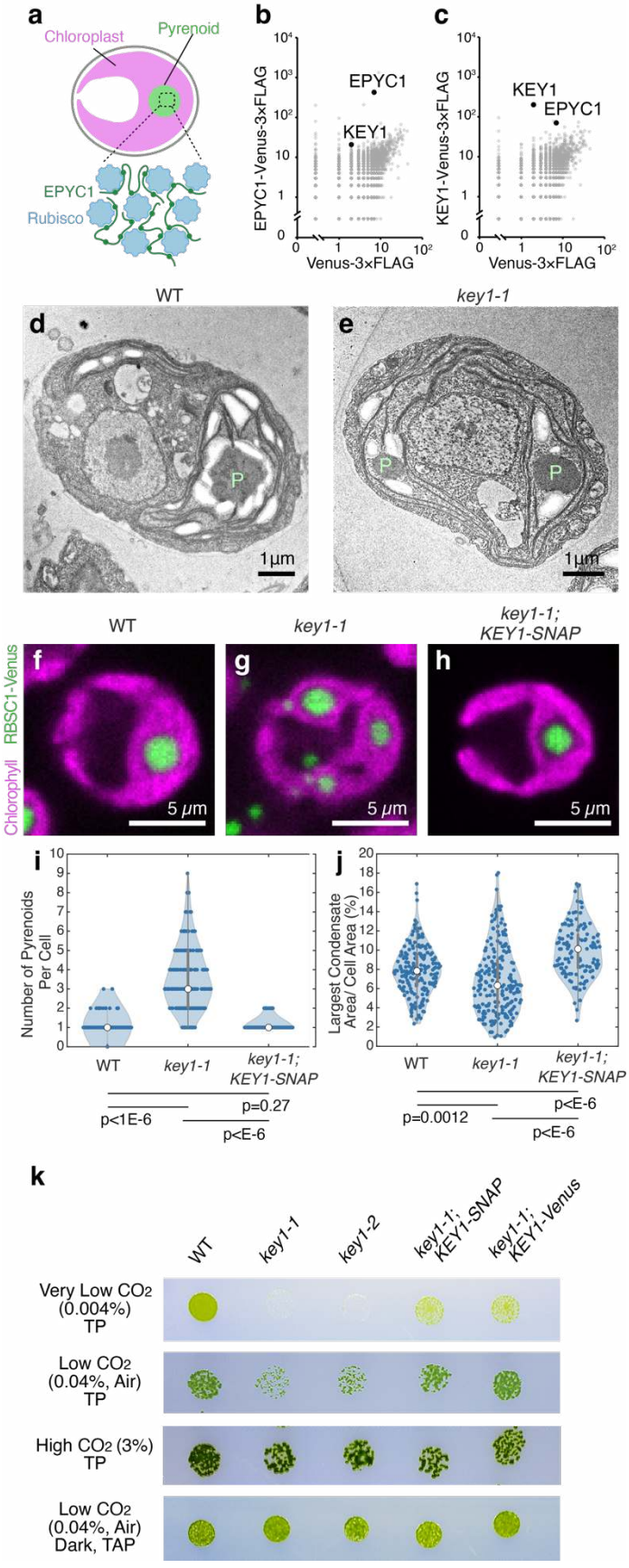
Acknowledgments

We would like to thank Saw Kyin and Henry Shwe for their help with mass spectrometry through the Princeton Molecular Biology Core Facility; Martin Wühr and Felix Keber for useful discussions on mass spectrometry data; Evangelos Gatzogiannis for microscopy support and discussions; Xiaoping Li for technical support of SPR experiments; Marie Bao, as part of Life Science Editors, Luke Mackinder, Alistair McCormick, Moritz Meyer, Aastha Garde, Victoria Crans, Sophie Skanchy, Amy Strom, Nima Jaberi-Lashkari, Anita Donlic, and Jordy Botello for manuscript editing help; Howard Griffiths, members of the Jonikas lab, Brangwynne lab, and Wingreen group for helpful discussions. We are grateful to the Chlamydomonas Resource Center for maintaining the strains described here. This project was supported by funding from the Howard Hughes Medical Institute to C.P.B. and M.C.J.; grants from the U.S. National Science Foundation (MCB-1935444, MCB-2410354, and MCB-1914989) and U.S. Department of Energy (DE-SC0020195) to M.C.J.; and U.S. National Institutes of Health (1R01GM140032-01) to N.S.W. and M.C.J. L.M.L. was supported by the Omenn-Darling Bioengineering Institute Innovators (ODBI^2) Postdoctoral Fellowship and the HHMI Hanna H. Gray Postdoctoral Fellowship. A.M.C. was supported by a Princeton Center for Theoretical Science (PCTS) fellowship and a Human Frontier Science (HFSP) fellowship (LT000035/2021). A.M.C. also acknowledges support from the Center for the Physics of Biological Function. The content is solely the responsibility of the authors and does not necessarily represent the official views of the funders.

bioRxiv preprint doi: https://doi.org/10.1101/2025.10.09.681382; this version posted October 10, 2025. The copyright holder for this preprint (which was not certified by peer review) is the author/funder, who has granted bioRxiv a license to display the preprint in perpetuity. It is made available under a CC-BY 4.0 International license.

Figures

bioRxiv preprint doi: https://doi.org/10.1101/2025.10.09.681382; this version posted October 10, 2025. The copyright holder for this preprint (which was not certified by peer review) is the author/funder, who has granted bioRxiv a license to display the preprint in perpetuity. It is made available under a CC-BY 4.0 International license.



bioRxiv preprint doi: https://doi.org/10.1101/2025.10.09.681382; this version posted October 10, 2025. The copyright holder for this preprint (which was not certified by peer review) is the author/funder, who has granted bioRxiv a license to display the preprint in perpetuity. It is made available under a CC-BY 4.0 International license.

Fig. 1. The candidate kinase KEY1 is necessary for normal pyrenoid size, number, and function.

a, The pyrenoid matrix in Chlamydomonas is a biomolecular condensate that forms through phase separation of the CO_2-fixing enzyme Rubisco and the intrinsically disordered linker protein EPYC1.

b-c, Spectral counts of proteins identified by mass spectrometry after immunoprecipitation of EPYC1-Venus-3×FLAG (**b**) or KEY1-Venus-3×FLAG (**c**), plotted against the spectral counts of the same proteins after immunoprecipitation of Venus-3×FLAG. See also Supplementary Table 1.

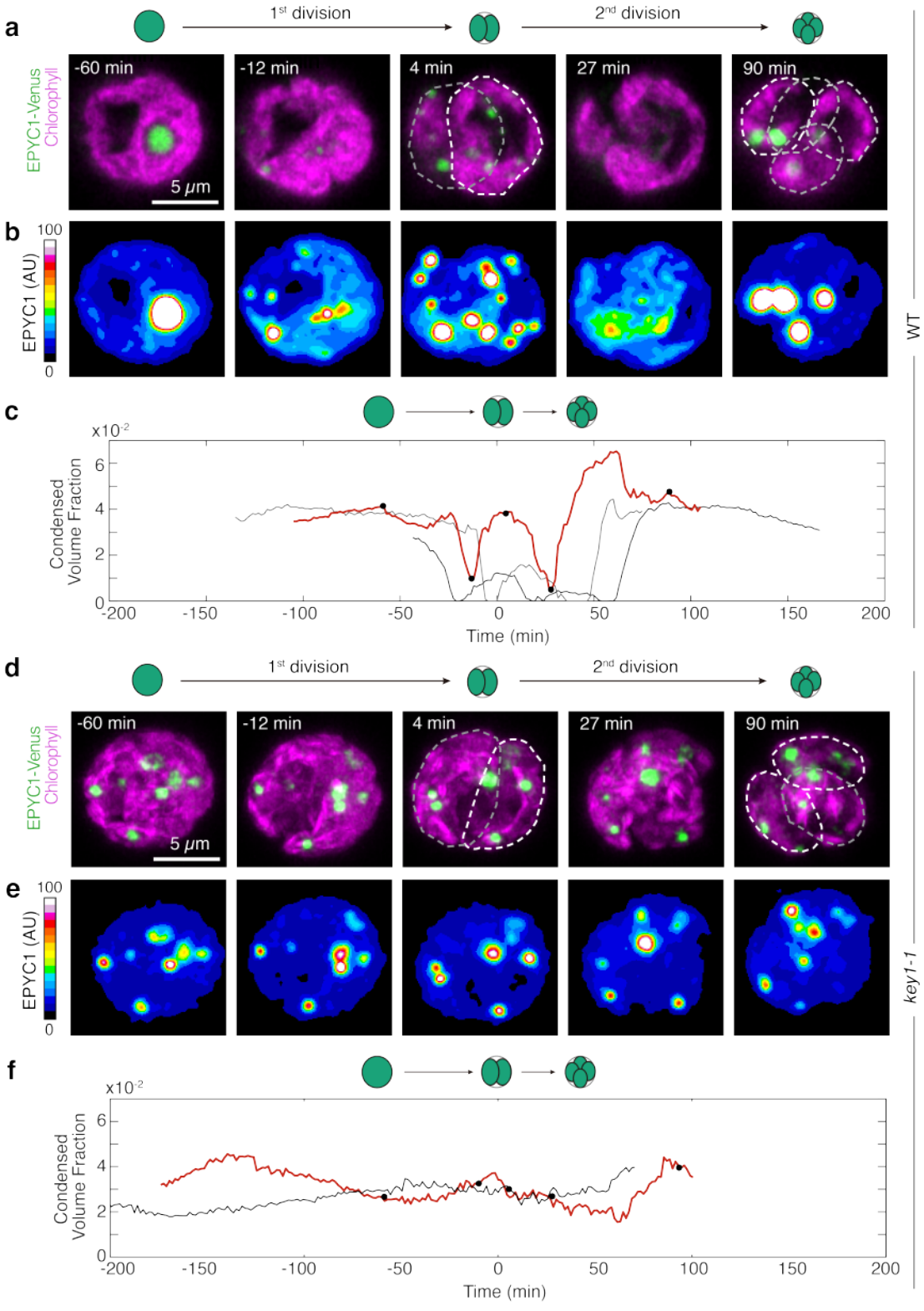
d-e, Transmission electron micrographs of a wild-type (WT) cell (**d**) and a *key1-1* mutant cell (**e**). P, pyrenoid. See also Extended Data Fig. 1.

f-h, Representative confocal fluorescence images of wild type (**f**), *key1-1* mutant (**g**), and the rescued strain *key1-1*;*KEY1-SNAP* (**h**), each expressing RBCS1-Venus to label Rubisco. Magenta shows the mid-plane of chlorophyll autofluorescence. Green shows the maximum intensity projection of RBCS1-Venus. See also Supplementary Video 1.

i-j, Violin plots of the number of condensates per cell (**i**) and the percent of cell area that the largest condensate occupies (**j**) for Rubisco labeled by RBCS1-Venus in wild type (n = 191 cells), *key1-1* mutant (n = 208 cells), and *key1-1*;*KEY1-SNAP* rescue (n = 122 cells). P-values calculated by a two-sided t-test. White circles indicate median of the distributions. Gray bars show first (thick) and third (thin) quartiles of the distributions.

k, Spot growth assays of wild type, two *key1* mutant alleles, and two rescued strains of *key1-1* on Tris-Phosphate (TP) medium in low CO_2 (air, 0.04%), very low CO_2 (0.004%), high CO_2 (3%) in light at 200 µmol photons/m^2/s, and on Tris-Acetate-Phosphate (TAP) medium in the dark in air.

bioRxiv preprint doi: https://doi.org/10.1101/2025.10.09.681382; this version posted October 10, 2025. The copyright holder for this preprint (which was not certified by peer review) is the author/funder, who has granted bioRxiv a license to display the preprint in perpetuity. It is made available under a CC-BY 4.0 International license.



bioRxiv preprint doi: https://doi.org/10.1101/2025.10.09.681382; this version posted October 10, 2025. The copyright holder for this preprint (which was not certified by peer review) is the author/funder, who has granted bioRxiv a license to display the preprint in perpetuity. It is made available under a CC-BY 4.0 International license.

Fig. 2. KEY1 is necessary for pyrenoid condensate size, number, and dissolution dynamics during cell division.

a-**b,** Timelapse microscopy of a dividing wild-type cell where the pyrenoid condensate is labeled by EPYC1-Venus (green, maximum z-projection) and the chloroplast is visualized through chlorophyll autofluorescence (magenta, mid-plane z) (**a**). The first cell division was completed at 0 min, and the second division was completed at 44 min, ending with four descendant cells. A heat map allows visualization of EPYC1-Venus dissolution during cell division (**b**).

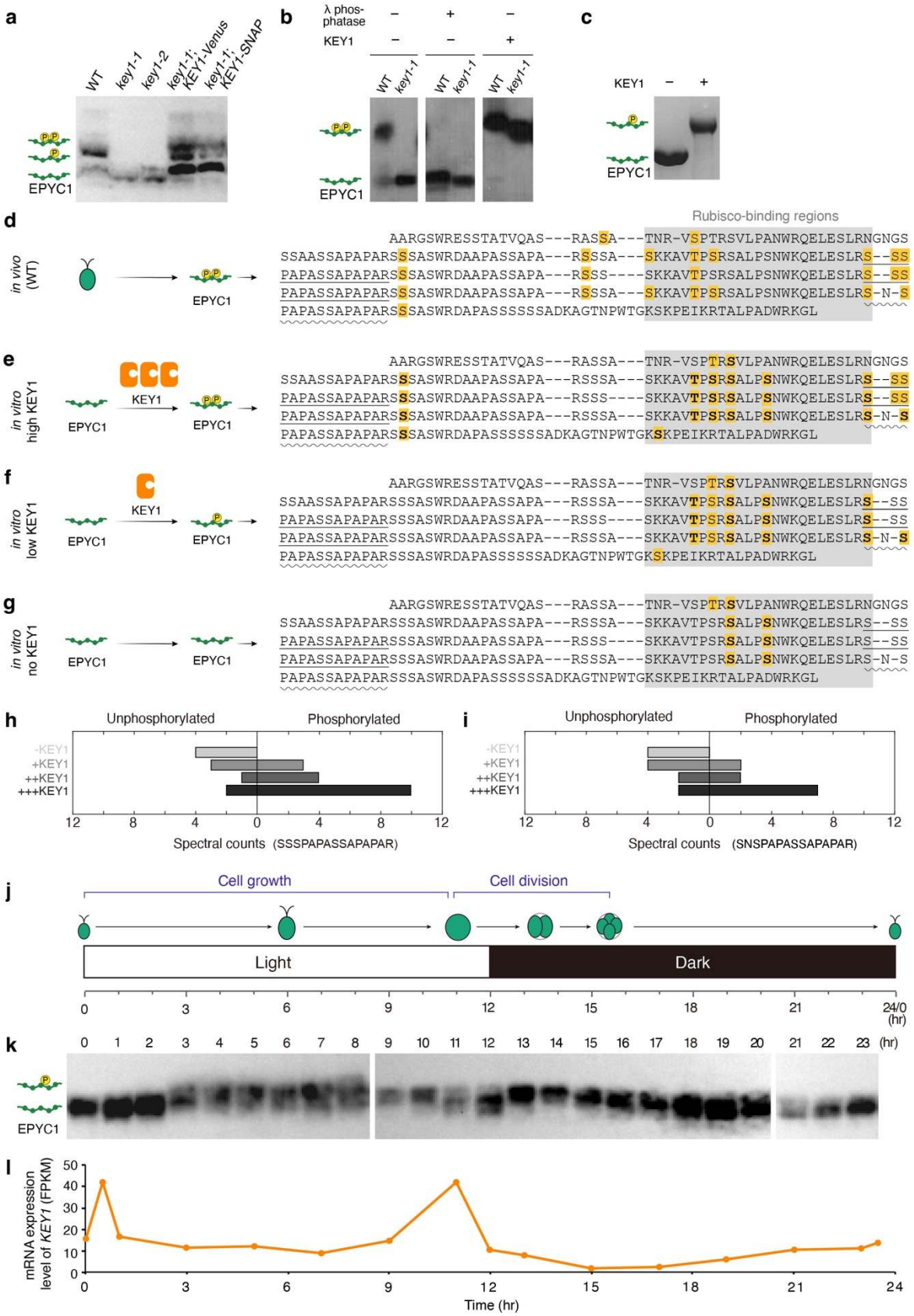
c, The condensed volume fraction ($V_{\text{dense phase}}/V_{\text{chloroplast(s)}}$) of EPYC1-Venus in wild-type cells throughout cell division for three representative parent cells. The red curve shows the cell in (**a**-**b**) with the time points marked as black dots. The first cell division occurs at 0 min for each cell. Protein concentration was assumed to be constant across the acquisition.

d-**e,** Timelapse microscopy of a dividing *key1-1* mutant cell with the pyrenoid condensate labeled by EPYC1-Venus (green, maximum z-projection) and the chloroplast visualized through chlorophyll autofluorescence (magenta, maximum z-projection) (**d**). The first cell division was completed at 0 min, and the second division was completed at 48 min, ending with four descendant cells. The heatmap shows EPYC1-Venus concentration (**e**).

f, The condensed volume fraction of EPYC1-Venus in *key1-1* mutant cells throughout cell division for two representative cells. The red curve shows the cell in (**d**-**e**) with the time points marked as black dots. The first cell division occurs at 0 min for each cell. Protein concentration was assumed to be constant across the acquisition.

See also Extended Data Figs. 2-3 and Supplementary Videos 2-5.

bioRxiv preprint doi: https://doi.org/10.1101/2025.10.09.681382; this version posted October 10, 2025. The copyright holder for this preprint (which was not certified by peer review) is the author/funder, who has granted bioRxiv a license to display the preprint in perpetuity. It is made available under a CC-BY 4.0 International license.



bioRxiv preprint doi: https://doi.org/10.1101/2025.10.09.681382; this version posted October 10, 2025. The copyright holder for this preprint (which was not certified by peer review) is the author/funder, who has granted bioRxiv a license to display the preprint in perpetuity. It is made available under a CC-BY 4.0 International license.

Fig. 3. KEY1 directly phosphorylates specific sites on EPYC1.

a, Anti-EPYC1 western blot based on Phos-tag gel of lysates of unsynchronized wild type, *key1* mutants, and *key1-1* rescued strains.

b, Anti-EPYC1 western blot based on Phos-tag gel of lysates of unsynchronized wild type and *key1-1*, with or without the addition of Lambda phosphatase or *E. coli*-expressed KEY1.

c, Coomassie-stained Phos-tag gel of purified EPYC1-GFP incubated with or without purified KEY1. Both proteins were expressed in *E. coli.*

d, Phosphorylation pattern of EPYC1 from unsynchronized wild-type Chlamydomonas cells analyzed by mass spectrometry. Residues with yellow backgrounds represent the identified phosphorylation sites. The gray block highlights previously identified Rubisco-binding regions.

e-**g** Phosphorylation pattern of EPYC1-GFP purified from *E. coli* treated with a large amount (3 μM) (**e**) or small amount (115 nM) (**f**) of KEY1 or untreated (**g**). Residues with yellow backgrounds represent phosphorylation sites identified in at least one experiment; bolded residues indicate sites identified in both replicate experiments. Untreated EPYC1-GFP from *E. coli* contained several phosphorylation sites not observed in EPYC1 from Chlamydomonas.

h-**i,** Spectral counts of unphosphorylated and phosphorylated versions of two EPYC1 peptides identified by mass spectrometry from EPYC1-GFP purified from *E. coli* with different treatments. The positions of these peptides are indicated in panels **d**-**g** with straight underlines (**h**) or wavy underlines (**i**).

j, Chlamydomonas cells were synchronized in a diurnal cycle, during which they grow in the light cycle, and divide twice in rapid succession upon the shift from light to dark each day.

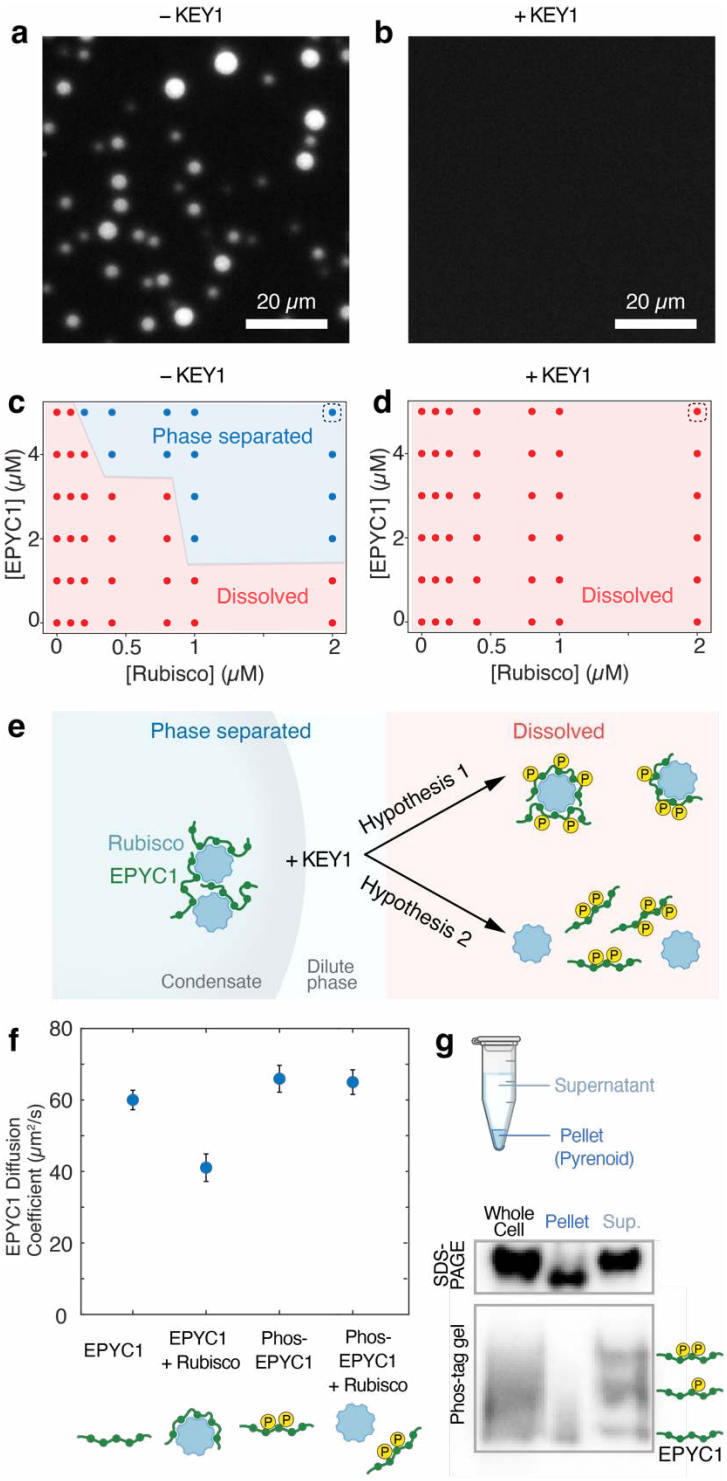
k, Cell lysates from a synchronized culture of wild-type cells were run on a Phos-tag gel and probed for EPYC1. Lower-mobility bands correspond to a more highly phosphorylated form of EPYC1.

l, The mRNA expression level of *KEY1* during a day, based on transcriptome data reported in Strenkert et al., 2019.[79]

The time points in panels **j** to **l** are aligned.

See also Extended Data Figs. 4 and 5.

bioRxiv preprint doi: https://doi.org/10.1101/2025.10.09.681382; this version posted October 10, 2025. The copyright holder for this preprint (which was not certified by peer review) is the author/funder, who has granted bioRxiv a license to display the preprint in perpetuity. It is made available under a CC-BY 4.0 International license.



bioRxiv preprint doi: https://doi.org/10.1101/2025.10.09.681382; this version posted October 10, 2025. The copyright holder for this preprint (which was not certified by peer review) is the author/funder, who has granted bioRxiv a license to display the preprint in perpetuity. It is made available under a CC-BY 4.0 International license.

Fig. 4. EPYC1 phosphorylation promotes the dissolution of Rubisco-EPYC1 condensates by disrupting Rubisco-EPYC1 binding.

a-**b**, 9 μM *E. coli*-purified EPYC1-GFP was untreated (**a**) or treated with 3.6 μM KEY1 (**b**) before being mixed with 2 μM Rubisco and imaged.

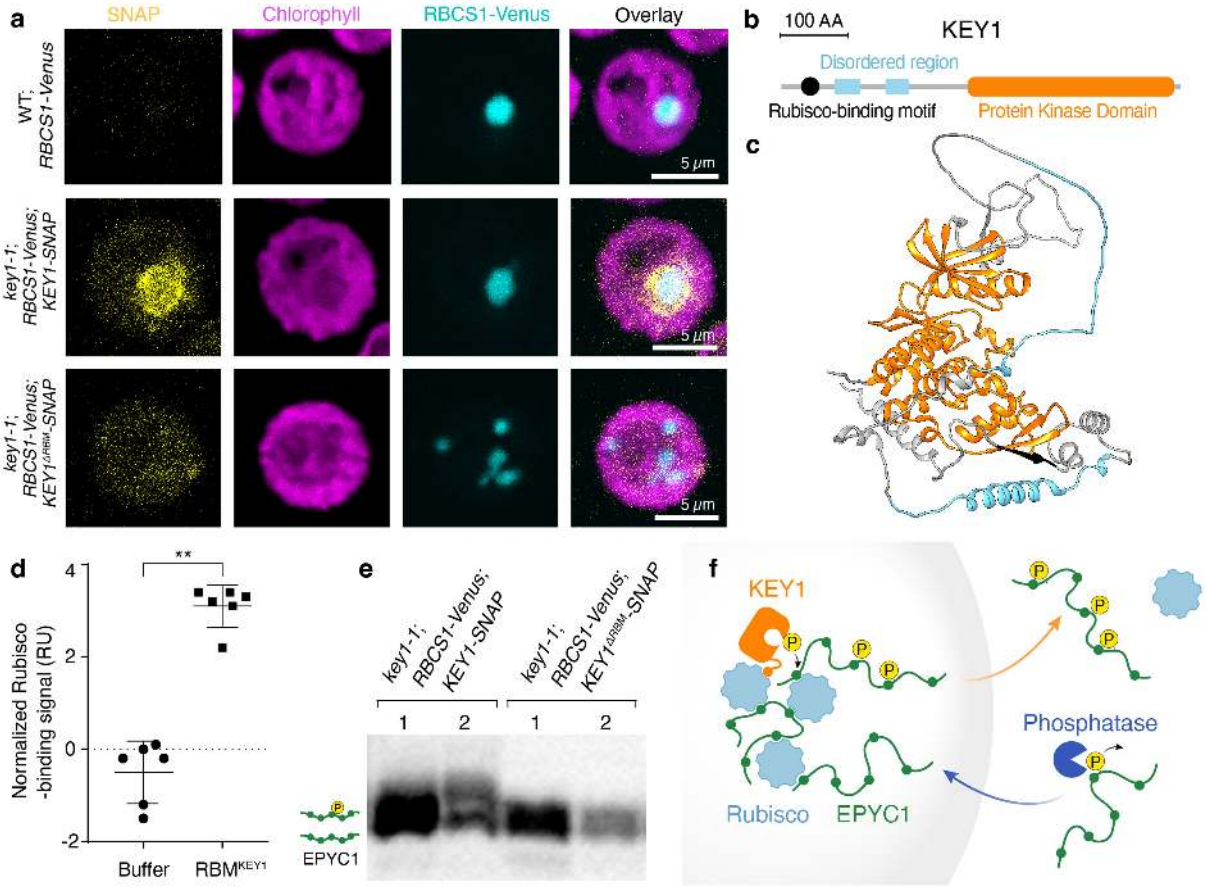
c-**d**, Concentration-dependent phase diagram of unphosphorylated EPYC1-GFP (**c**) or EPYC1-GFP phosphorylated by 3.6 μM KEY1 (**d**) along with Rubisco. Dashed boxes indicate samples shown in panel **a,b**.

e, Schematic of the two possible mechanisms for KEY1-mediated EPYC1 phosphorylation that promote dissolution of the EPYC1-Rubisco condensate. In Hypothesis 1, phosphorylation of EPYC1 promotes the formation of small clusters of a single Rubisco and several EPYC1 molecules. In Hypothesis 2, phosphorylation of EPYC1 disrupts the interactions between EPYC1 and Rubisco.

f, The diffusion coefficient of unphosphorylated or phosphorylated full-length EPYC1 tagged with GFP in the presence of Rubisco was measured using fluorescence correlation spectroscopy. Blue circles represent the mean diffusion coefficient from two experimental replicates in which three FCS measurements were made. The error bars represent the standard deviation. The cartoon models underneath the x-axis show our interpretation of the results.

g, Whole cell lysate was fractionated into condensed phase (pyrenoid pellet) and the dilute phase (supernatant). Fractions were separated by SDS-PAGE (top) and Phos-tag (bottom) gels and probed for EPYC1 by western blot.

bioRxiv preprint doi: https://doi.org/10.1101/2025.10.09.681382; this version posted October 10, 2025. The copyright holder for this preprint (which was not certified by peer review) is the author/funder, who has granted bioRxiv a license to display the preprint in perpetuity. It is made available under a CC-BY 4.0 International license.



669

bioRxiv preprint doi: https://doi.org/10.1101/2025.10.09.681382; this version posted October 10, 2025. The copyright holder for this preprint (which was not certified by peer review) is the author/funder, who has granted bioRxiv a license to display the preprint in perpetuity. It is made available under a CC-BY 4.0 International license.

Fig. 5. A Rubisco-binding motif localizes KEY1 to the pyrenoid condensate to mediate function.

a, Confocal fluorescence images of cells from unsynchronized cultures of wild type, showing the background signal of SNAP dye staining (top row); *key1-1* with RBCS1-Venus rescued by KEY1-SNAP, showing representative localization of KEY1 (middle row); and *key1-1* with RBCS1-Venus expressing KEY1$^{\Delta RBM}$-SNAP, showing representative localization of KEY1 with a five amino acid mutation disrupting the Rubisco-binding motif (bottom row). Magenta shows chlorophyll autofluorescence, cyan shows RBCS1-Venus, and yellow shows SNAP. See also Extended Data Fig. 6.

b, Predicted KEY1 domains (based on the Uniprot dataset [92]). The Rubisco-binding motif is in black, the disordered regions are shown in cyan, and the protein kinase domain is shown in Orange.

c, KEY1 3D structure predicted by AlphaFold. The color key is the same as in panel **b**. See also Supplementary Video 6.

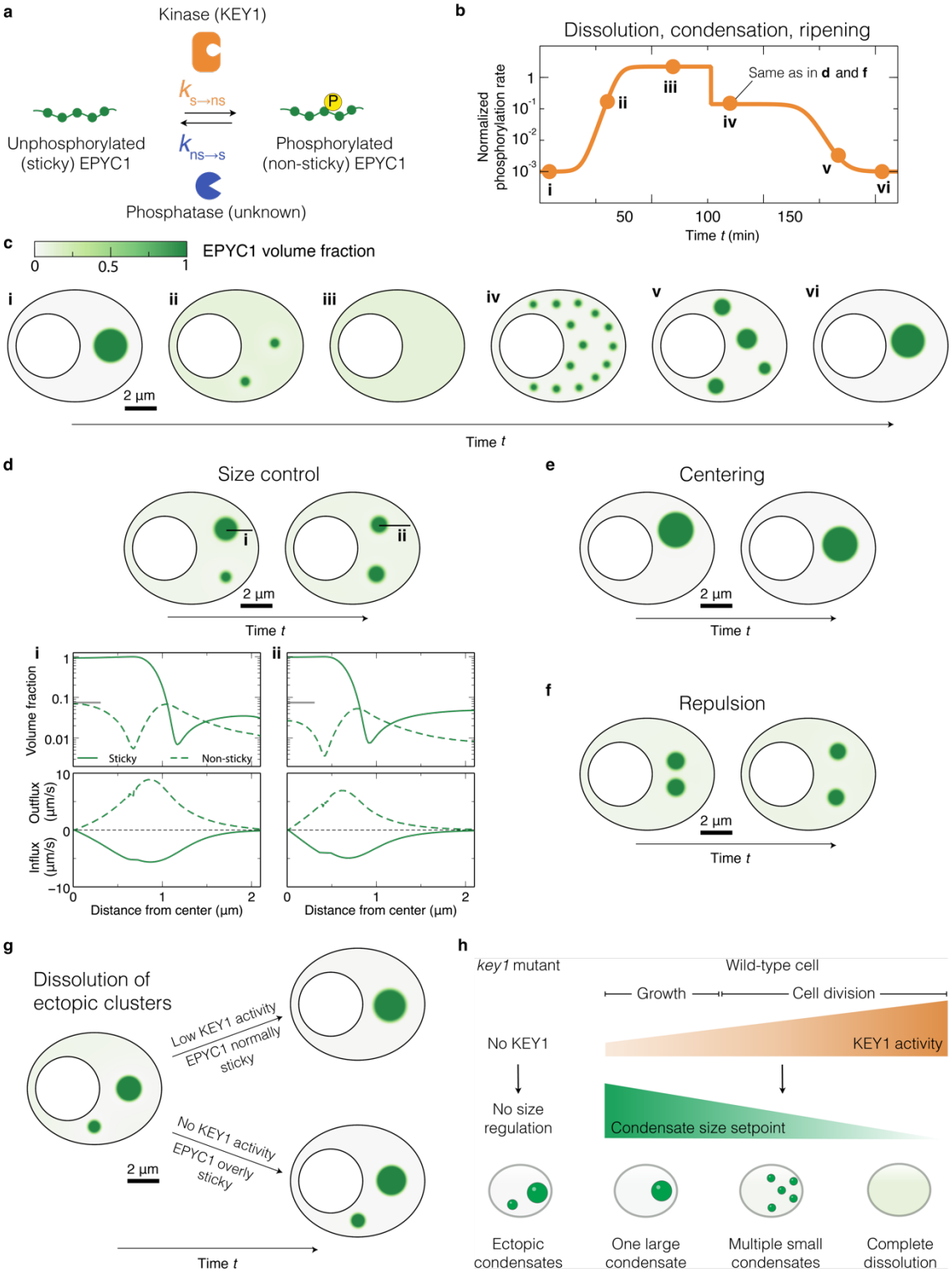
d, The binding to Rubisco of a peptide representing KEY1's Rubisco-binding motif (RBM^{KEY1}) was assayed using surface plasmon resonance in comparison to a buffer-only control. $^{**}p < 0.05$, two-sided Mann-Whitney *U* test.

e, EPYC1 phosphorylation was assayed using anti-EPYC1 western blot of lysates from *key1-1*;*KEY1-SNAP* and *key1-1*;*KEY1$^{\Delta RBM}$-SNAP* run on a Phos-tag gel.

f, Cartoon of the proposed molecular mechanism of KEY1. In the pyrenoid condensate, KEY1 phosphorylates EPYC1, disrupting interactions between EPYC1 and Rubisco and allowing phosphorylated EPYC1 to diffuse out of the condensate. We speculate that a phosphatase dephosphorylates EPYC1 in the dilute phase outside the pyrenoid condensate, promoting its interaction with Rubisco and favoring the entry of unphosphorylated EPYC1 into the condensate.

See also Extended Data Figs. 6-8 and Supplementary Video 6.

bioRxiv preprint doi: https://doi.org/10.1101/2025.10.09.681382; this version posted October 10, 2025. The copyright holder for this preprint (which was not certified by peer review) is the author/funder, who has granted bioRxiv a license to display the preprint in perpetuity. It is made available under a CC-BY 4.0 International license.



bioRxiv preprint doi: https://doi.org/10.1101/2025.10.09.681382; this version posted October 10, 2025. The copyright holder for this preprint (which was not certified by peer review) is the author/funder, who has granted bioRxiv a license to display the preprint in perpetuity. It is made available under a CC-BY 4.0 International license.

Fig. 6. Modeling supports the role of KEY1 in regulating pyrenoid condensate size and number and reveals a centering mechanism.

a, Overview of our model: we represent the EPYC1-Rubisco system through EPYC1 only, with EPYC1 existing in two states – unphosphorylated (sticky) and phosphorylated (non-sticky). The rates of switching between these states are mediated by a kinase (KEY1) and a phosphatase. For simplicity, we assume both the switching rates to be spatially uniform, and the dephosphorylation rate to be constant.

b, To recapitulate the hypothesized temporal changes in KEY1 activity during cell division, the EPYC1 phosphorylation rate is varied over time.

c, The computed spatiotemporal phase behaviors are shown as snapshots (times indicated by dots in panel **b**). The colorbar indicates EPYC1 concentration for panels **c**-**g**. At a low phosphorylation rate, a single EPYC1 cluster forms (i). At intermediate phosphorylation rate, EPYC1 forms small stable clusters that do not coarsen (ii). At a very high phosphorylation rate, the stable cluster dissolves as most EPYC1s are non-sticky (iii). As the phosphorylation rate is reduced, multiple stable small clusters re-appear (iv) and coarsen into a single cluster (v and vi).

d, Due to KEY1 activity, the system exhibits a size control mechanism at intermediate phosphorylation rates (rate same as in **c**-iv). The model is initialized with two EPYC1 clusters of different sizes (i). After a finite time, both clusters equilibrate, reaching the same stable size (ii). The sticky and non-sticky EPYC1 volume fractions (top) and radially directed influx and outflux (bottom) across one of the condensates are plotted for timepoints i and ii. The clusters reach a stable size when the inflow and outflow of sticky and non-sticky EPYC1, respectively, become balanced (ii, see Methods). The gray horizontal line indicates the maximum volume fraction reached by non-sticky EPYC1 in the dense phase.

e, The model is initialized with an off-center condensate, which self-centers into the canonical position farthest from the boundaries (KEY1 level lower than in **d** and **f**).

f, The model is initialized with two condensates that are initially placed too close to each other. They move apart over time, exhibiting repulsive behavior.

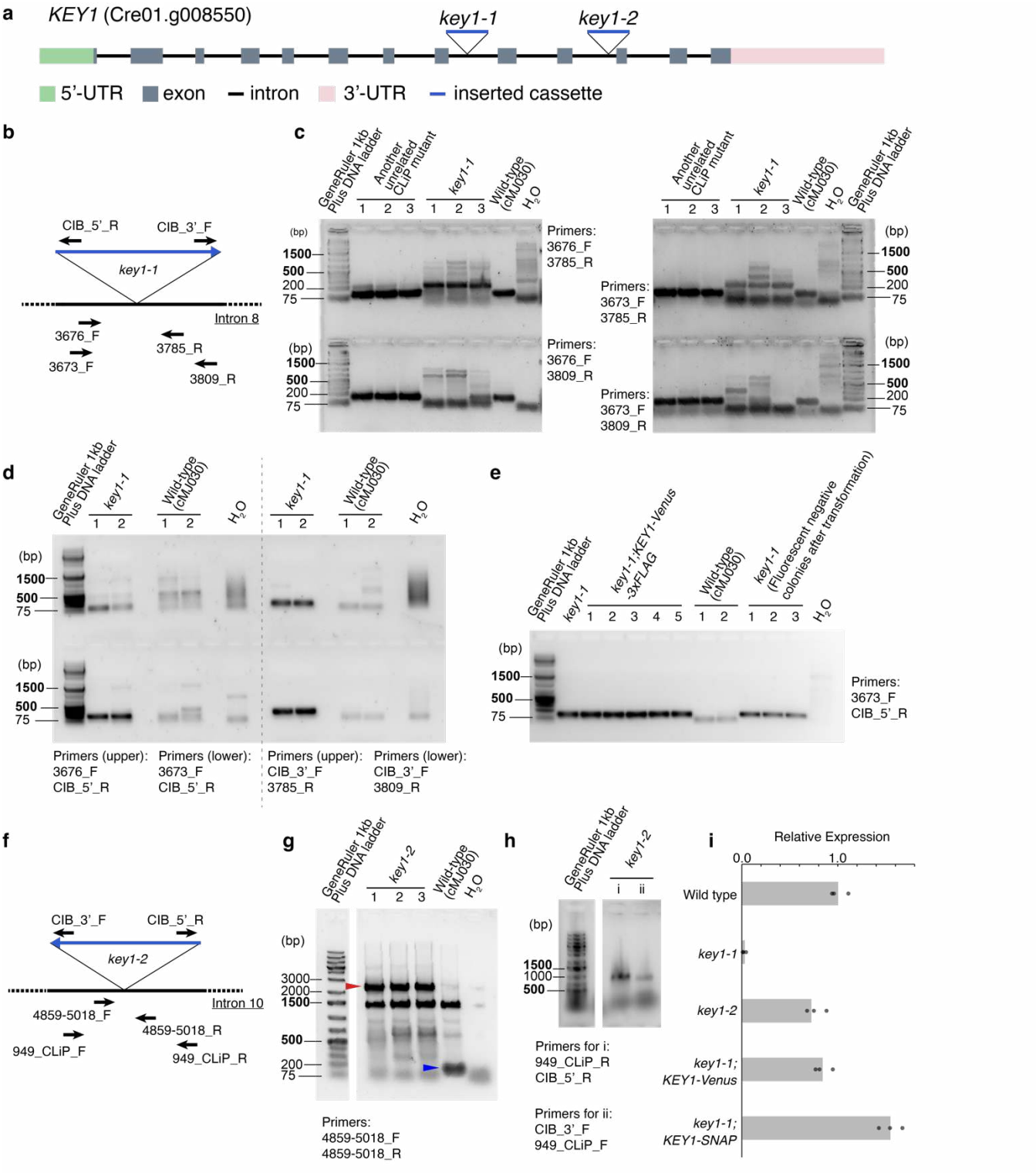
g, With no KEY1 activity, EPYC1 is modeled as overly sticky, which prevents coarsening over time through Ostwald ripening (top). Low KEY1 activity, in addition to mediating switching, is modeled as reducing the magnitude of sticky self-attractive interactions, which allows ectopic clusters to dissolve (Bottom).

h, Summary of our understanding of how KEY1 activity levels impact the phase behaviors and size of pyrenoid condensates.

See also Extended Data Fig. 9 and Supplementary Videos 7-14.

bioRxiv preprint doi: https://doi.org/10.1101/2025.10.09.681382; this version posted October 10, 2025. The copyright holder for this preprint (which was not certified by peer review) is the author/funder, who has granted bioRxiv a license to display the preprint in perpetuity. It is made available under a CC-BY 4.0 International license.

Extended Data Figures



bioRxiv preprint doi: https://doi.org/10.1101/2025.10.09.681382; this version posted October 10, 2025. The copyright holder for this preprint (which was not certified by peer review) is the author/funder, who has granted bioRxiv a license to display the preprint in perpetuity. It is made available under a CC-BY 4.0 International license.

Extended Data Fig. 1. Genetic characterization and complementation of *key1* mutants, related to Fig. 1.

a, Gene structure of *KEY1* and the cassette insertion sites of *key1-1* and *key1-2* mutants obtained from the CLiP mutant library collection[71] (see also Methods). The insertion cassettes in the CLiP mutants contain transcription terminators, which typically lead to the knockdown of the transcript due to nonsense-mediated decay.

b, Cartoon of the *key1-1* mutant cassette insertion site, showing the approximate positions of the primers used to characterize *key1-1*.

c, Agarose gel electrophoresis of the results of PCR amplification across the cassette insertion sites of *key1-1*. In each of the four primer-pair combinations shown, a specific fragment (ranging from 110 bp to 137 bp) was amplified from wild-type genomic DNA, but not from the genomic DNA of any of the three single colonies of *key1-1*, suggesting a DNA insertion at this locus in the *key1-1* genome.

d, Agarose gel electrophoresis of the results of PCR amplification across the junction regions of the insertion cassette and the KEY1 encoding sequence on both sides of the insertion site in *key1-1*. In each of the four primer-pair combinations shown, a specific fragment (ranging from ~160 bp to ~230 bp) was amplified from *key1-1* genomic DNA in both replicates, but not from wild-type genomic DNA in either replicate, indicating a cassette insertion at this locus in the *key1-1* genome.

e, Agarose gel electrophoresis of the results of PCR amplification across the junction regions of the insertion cassette and the KEY1 encoding sequence in the complemented strain of *key1-1* (*key1-1;KEY1-Venus-3×FLAG*). A specific fragment was amplified from the genomic DNA of both *key1-1* and the complemented strains, but not from wild-type genomic DNA in either replicate, indicating a cassette insertion in the complemented strain at the same locus as in the *key1-1* genome.

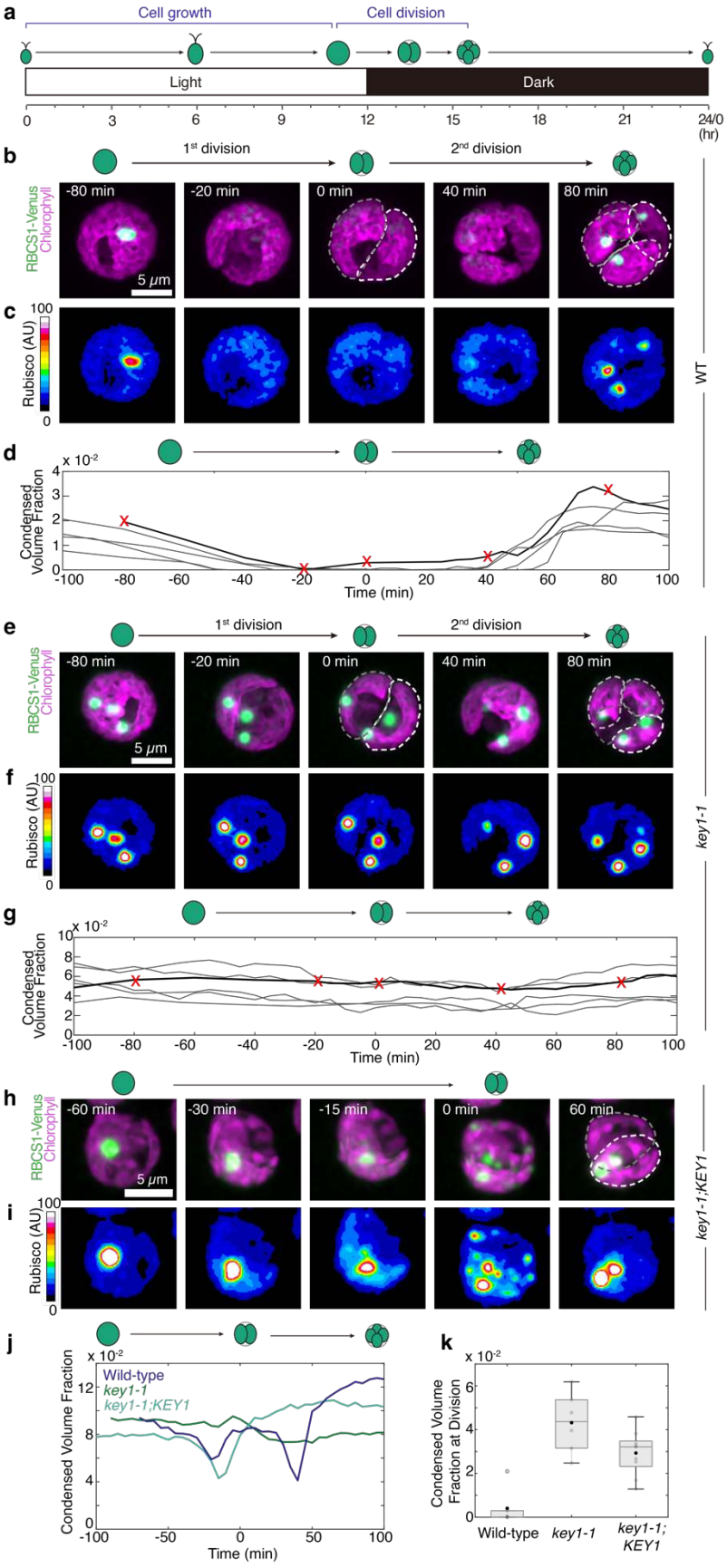
f, Cartoon of the *key1-2* mutant cassette insertion site, showing the approximate positions of the primers used to characterize *key1-2*.

g, Agarose gel electrophoresis of the results of PCR amplification across the cassette insertion sites of *key1-2*. A specific fragment (160 bp, indicated by the blue arrowhead) was amplified from wild-type genomic DNA, but not from the genomic DNA of any of the three single colonies of *key1-2*. However, a specific band of ~2.4 kb (indicated by the red arrowhead) was amplified from the genomic DNA of each of the three single colonies of *key1-2,* indicating a cassette insertion at this locus in the *key1-2* genome.

h, Agarose gel electrophoresis of the results of PCR amplification across the junction regions of the insertion cassette and the KEY1 encoding sequence on both sides of the insertion site in *key1-2*. In each of the primer-pair combinations shown, a specific fragment (~1 kb) was amplified from *key1-2* genomic DNA, indicating a cassette insertion at this locus in the *key1-2* genome.

i, RT-qPCR analysis of KEY1 expression in lines *key1-1*, *key1-2*, *key1-1;KEY1-Venus*, *key1-1;KEY1-SNAP*, and wild type. Error bars represent the standard deviation from three biological replicates.

bioRxiv preprint doi: https://doi.org/10.1101/2025.10.09.681382; this version posted October 10, 2025. The copyright holder for this preprint (which was not certified by peer review) is the author/funder, who has granted bioRxiv a license to display the preprint in perpetuity. It is made available under a CC-BY 4.0 International license.



bioRxiv preprint doi: https://doi.org/10.1101/2025.10.09.681382; this version posted October 10, 2025. The copyright holder for this preprint (which was not certified by peer review) is the author/funder, who has granted bioRxiv a license to display the preprint in perpetuity. It is made available under a CC-BY 4.0 International license.

Extended Data Fig. 2. Rubisco-Venus behaves similarly to EPYC1-Venus in WT and *key1-1*, and the dissolution of the pyrenoid condensate is observed in the *key1-1* rescued strain, related to Fig. 2.

a, Chlamydomonas cells were synchronized in a diurnal cycle where they divided twice in rapid succession upon the shift from light to dark each day.

b-**c**, Timelapse microscopy of a dividing wild-type cell where the pyrenoid condensate is labeled by RBCS1-Venus (green, maximum z-projection), and the chloroplast is visualized through chlorophyll autofluorescence (magenta, maximum z-projection) (**b**). The first cell division was completed at 0 min, and the second division was completed at 50 min, ending with four descendant cells. A heat map allows visualization of RBCS1-Venus dissolution during cell division (**c**).

d, The condensed volume fraction ($V_{\text{dense phase}}/V_{\text{chloroplast(s)}}$) of RBCS1-Venus in wild-type cells throughout cell division. The gray curves represent the individual mother cell profiles.The black curve shows the cell in (**b**, **c**) with the time points marked in red. Protein concentration was assumed to be constant across the acquisition.

e-**f**, Timelapse microscopy of a dividing *key1-1* mutant cell with the pyrenoid condensate labeled by RBCS1-Venus (green, maximum z-projection) and the chloroplast visualized through chlorophyll autofluorescence (magenta, maximum z-projection) (**e**). The first cell division was completed at 0 min, and the second division was completed at 55 min, ending with four descendant cells. The heatmap shows RBCS1-Venus concentration (**f**).

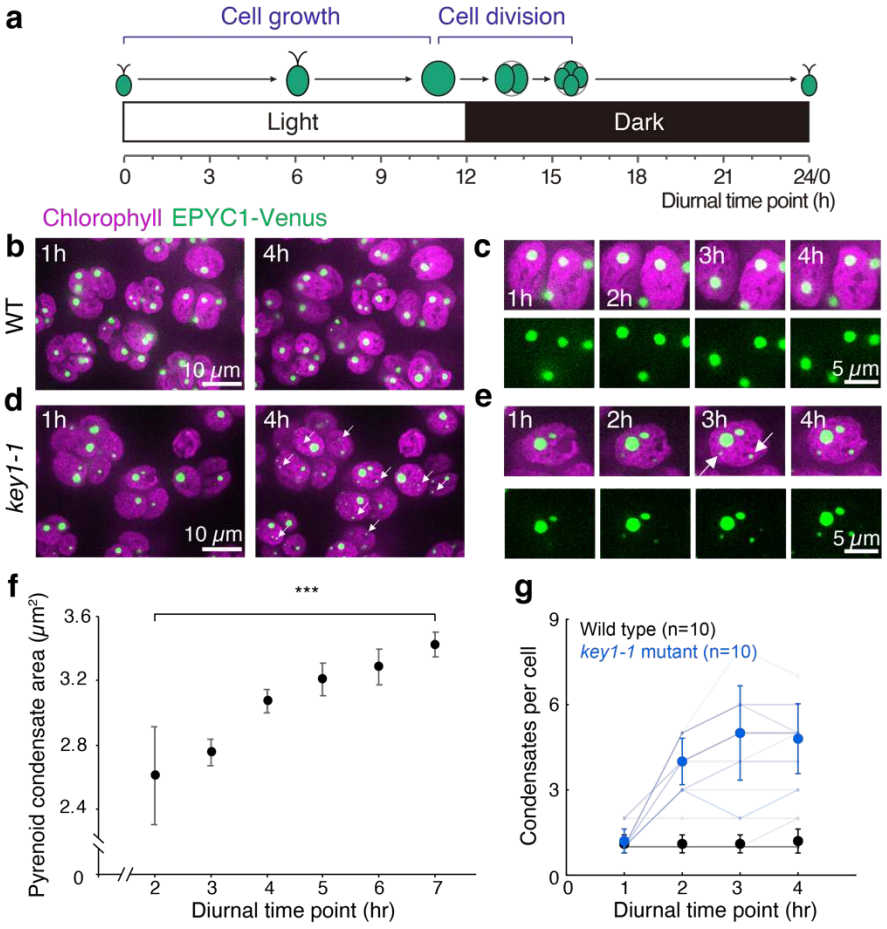
g, Condensed volume fraction of RBCS1-Venus in *key1-1* mutant cells throughout cell division. The gray curves represent the individual mother cell profiles. The black curve shows the cell in (**e**-**f**) with the time points marked in red. Protein concentration was assumed to be constant across the acquisition.

h-**i**, Timelapse microscopy of a dividing *key1-1* cell rescued with KEY1 (*key1-1*;*RBCS1-Venus*;*KEY1-SNAP*) with the pyrenoid condensate labeled by RBCS1-Venus (green, maximum z-projection) and chloroplast visualized through chlorophyll autofluorescence (magenta, maximum z-projection) (**h**). The cell divided once at 0 min. The heatmap shows RBCS1-Venus concentration (**i**).

j, The condensed volume fraction of RBCS1-Venus in wild type, *key1-1* mutant, and the rescued strain (*key1-1*;*RBCS1-Venus*;*KEY1-SNAP*) during cell division. Protein concentration was assumed to be constant across the acquisition.

k, Condensed volume fraction of RBCS1-Venus in wild type (n = 6 cells), *key1-1* (n = 6 cells), and the rescued strain (*key1-1*;*RBCS1-Venus*;*KEY1-SNAP*, n = 9 cells) at cell division. The black circle indicates the median, the gray box indicates the first quartile, and the line indicates the third quartile of each distribution. The grey circles indicate individual cells. Protein concentration was assumed to be constant across the acquisition.

bioRxiv preprint doi: https://doi.org/10.1101/2025.10.09.681382; this version posted October 10, 2025. The copyright holder for this preprint (which was not certified by peer review) is the author/funder, who has granted bioRxiv a license to display the preprint in perpetuity. It is made available under a CC-BY 4.0 International license.



812

bioRxiv preprint doi: https://doi.org/10.1101/2025.10.09.681382; this version posted October 10, 2025. The copyright holder for this preprint (which was not certified by peer review) is the author/funder, who has granted bioRxiv a license to display the preprint in perpetuity. It is made available under a CC-BY 4.0 International license.

Extended Data Fig. 3. The pyrenoid condensate grows over time in the wild type, while ectopic condensates nucleate over time in the *key1-1* mutant during cell growth, related to Fig. 2.

a, Chlamydomonas cells were synchronized in a diurnal cycle, during which they grow in the light cycle, and divide twice in rapid succession upon the shift from light to dark each day.

b, Timelapse confocal images of wild-type cells during the light cycle. The pyrenoid condensate is labeled by EPYC1-Venus (green, maximum z-projection), and the chloroplast is visualized through chlorophyll autofluorescence (magenta, maximum z-projection).

c, Zoom in of a single wild-type cell from **b** showing hourly time points.

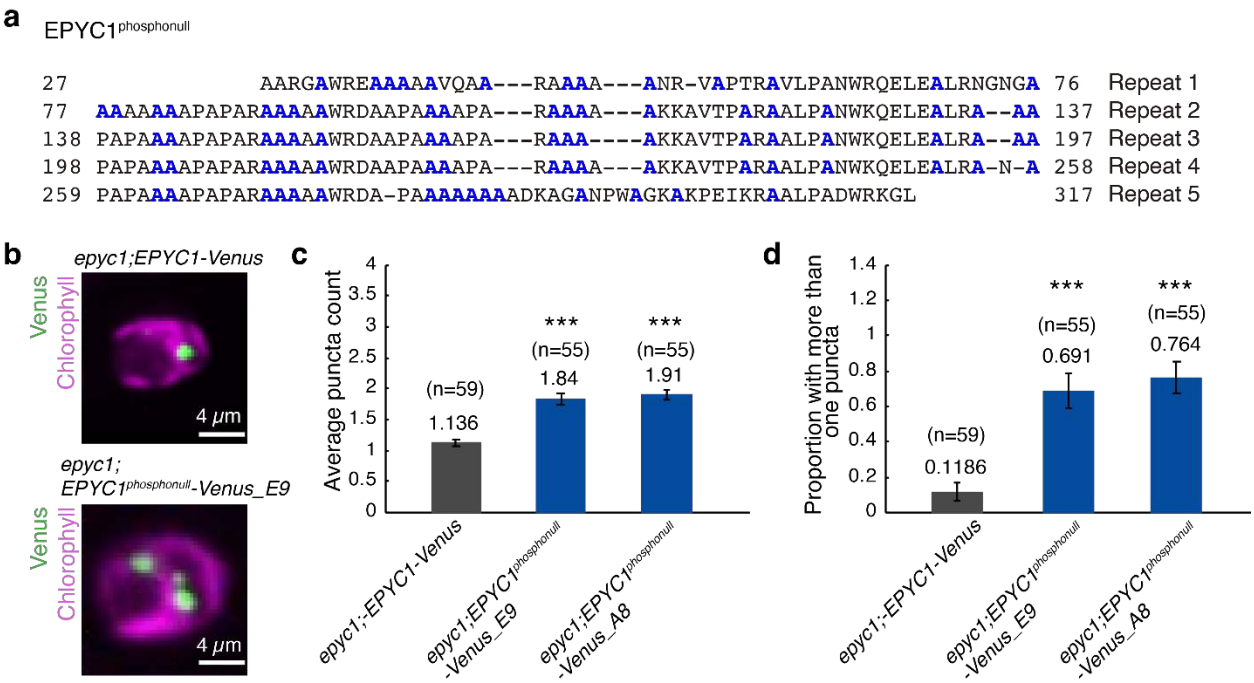
d, Timelapse confocal images of a *key1-1* cell during the light cycle. The pyrenoid condensate is labeled by EPYC1-Venus (green, maximum z-projection), and the chloroplast is visualized through chlorophyll autofluorescence (magenta, maximum z-projection). The white arrows indicate several of the ectopic pyrenoid condensates that appeared during the timelapse.

e, Zoom-in of a single *key1-1* cell from **d** showing hourly time points. The white arrows indicate the ectopic pyrenoid condensates that appeared during the timelapse.

f, Mean pyrenoid condensate area in wild-type cells expressing EPYC1-Venus (n = 11 cells). Error bars, SEM. *** indicates a statistically-significant ($p < 0.001$, two-sided Wilcoxon signed rank test) difference in area from hour 2 to hour 7.

g, Mean condensate number per cell in wild-type (black) and *key1-1* (blue) cells expressing EPYC1-Venus during cell growth (n=10 cells). Error bars represent standard deviation. Light gray and blue indicate individual cell traces.

bioRxiv preprint doi: https://doi.org/10.1101/2025.10.09.681382; this version posted October 10, 2025. The copyright holder for this preprint (which was not certified by peer review) is the author/funder, who has granted bioRxiv a license to display the preprint in perpetuity. It is made available under a CC-BY 4.0 International license.



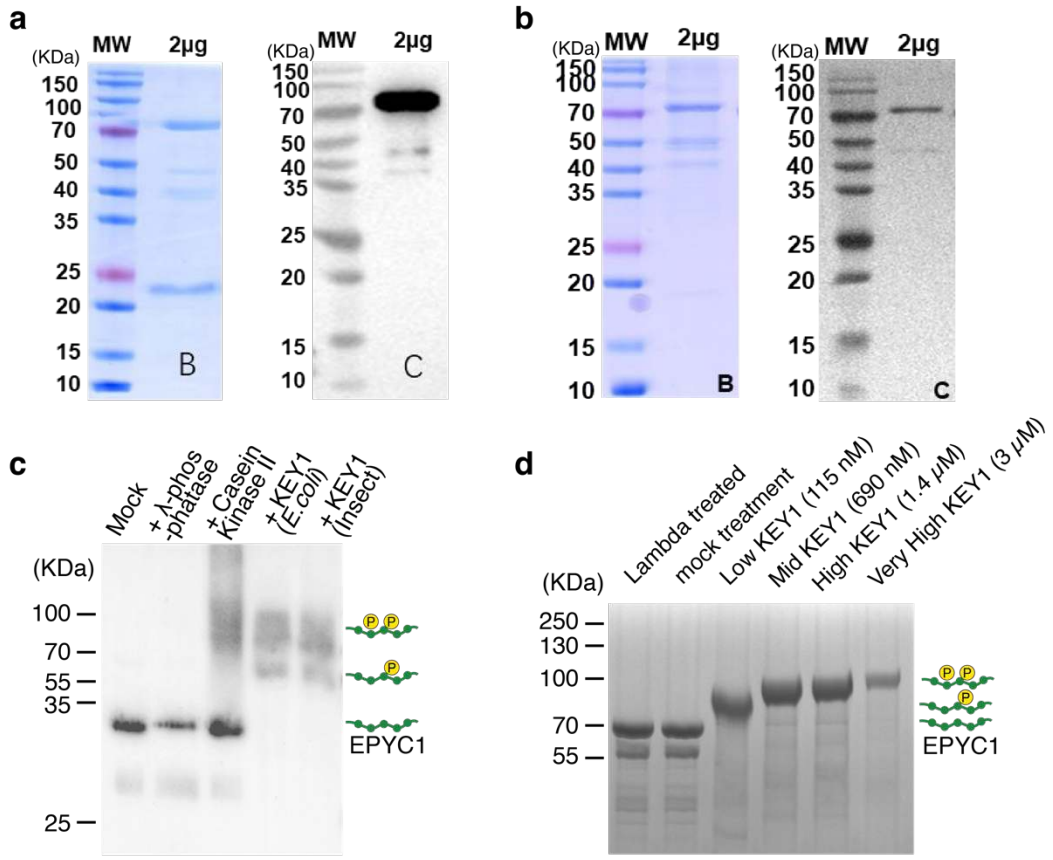
Extended Data Fig. 4. Phosphonull mutants of EPYC1 have multiple condensates, related to Fig. 3.

a, Amino acid sequence of the phosphonull mutant of EPYC1. All the Serines and Threonines in the wild-type EPYC1 sequence were substituted for Alanines, which are shown in blue.

b, Confocal fluorescence images of *epyc1* rescued by EPYC1 (*epyc1*;*EPYC1-Venus*) (top) and *epyc1* expressing the phosphonull mutant of EPYC1 (*epyc1*;*EPYC1*^{phosphonull}*-Venus*) (bottom). Magenta shows the mid-plane of chlorophyll autofluorescence. Green shows the maximum intensity z-projection of Venus.

c-**d**, The average number of condensates (**c**) and the proportion of cells in the sample with greater than one condensate (**d**) were quantified in a representative sample of cells. Sample sizes are indicated on bars. Values and error bars depict mean and SEM, respectively. *** indicates a phenotype is different from the *epyc1*;*EPYC1-Venus* phenotype with statistical significance $p < 0.001$, two-sided Wilcoxon-ranked sum test.

bioRxiv preprint doi: https://doi.org/10.1101/2025.10.09.681382; this version posted October 10, 2025. The copyright holder for this preprint (which was not certified by peer review) is the author/funder, who has granted bioRxiv a license to display the preprint in perpetuity. It is made available under a CC-BY 4.0 International license.



Extended Data Fig. 5. Purified KEY1 from *E. coli* and insect cells is active on *E. coli*-expressed EPYC1, related to Fig. 3.

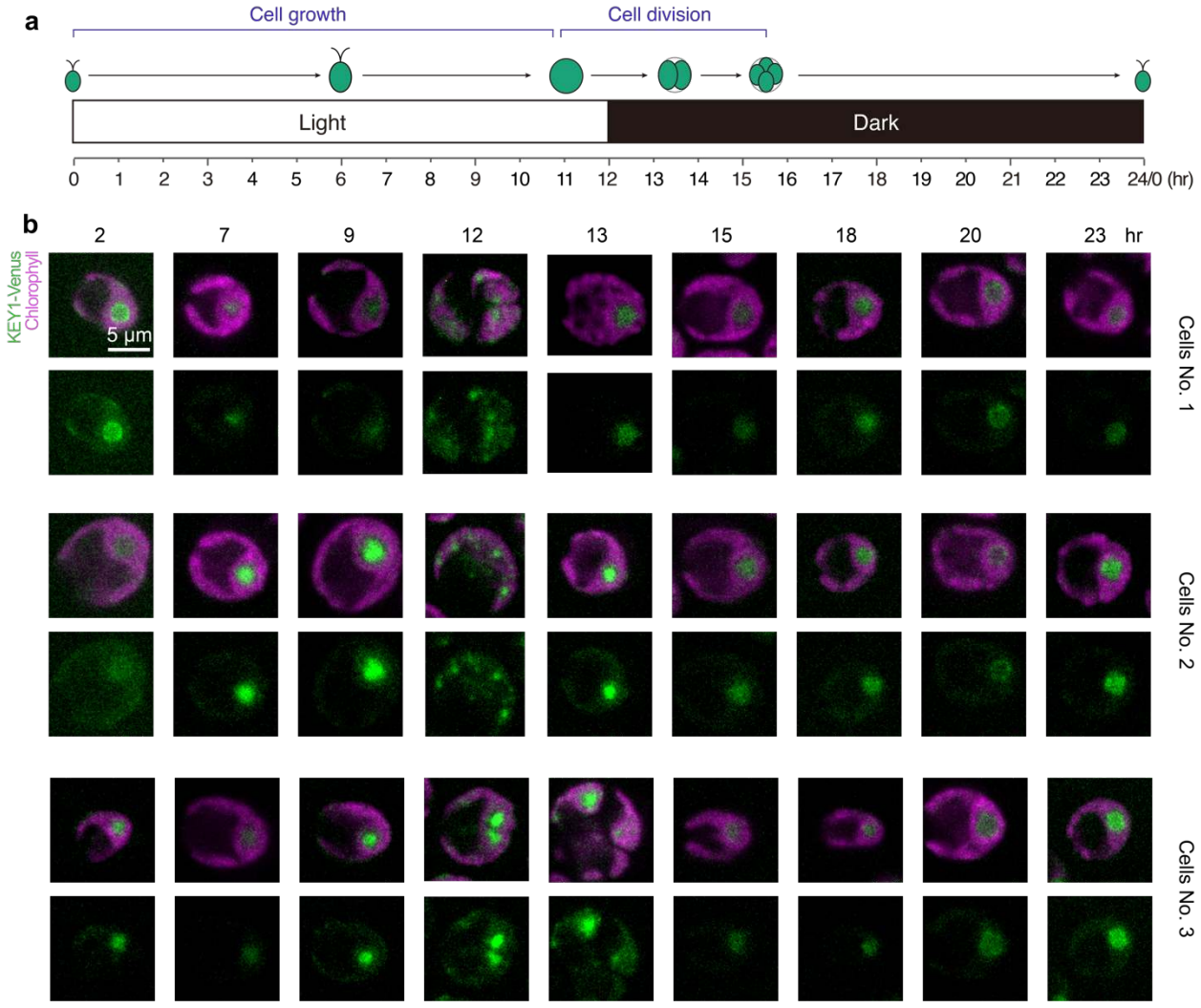
a, Coomassie blue staining (left) and western blot with anti-His-tag antibody (right) for KEY1 protein purified from *E. coli* expression system (data provided by Proteogenix).

b, Coomassie blue staining (left) and western blot with anti-His-tag antibody (right) for KEY1 protein purified from baculovirus/insect cell expression system (data provided by Proteogenix).

c, Anti-EPYC1 western blot of Phos-tag gel of purified His-tagged EPYC1 expressed in *E. coli* with or without treatment with Lambda phosphatase, Casein Kinase II, *E. coli*-expressed KEY1, or insect cell expressed KEY1.

d, Coomassie stain of Phos-tag gels of *E. coli*-expressed EPYC1-GFP samples prepared for phosphoproteomics.

bioRxiv preprint doi: https://doi.org/10.1101/2025.10.09.681382; this version posted October 10, 2025. The copyright holder for this preprint (which was not certified by peer review) is the author/funder, who has granted bioRxiv a license to display the preprint in perpetuity. It is made available under a CC-BY 4.0 International license.

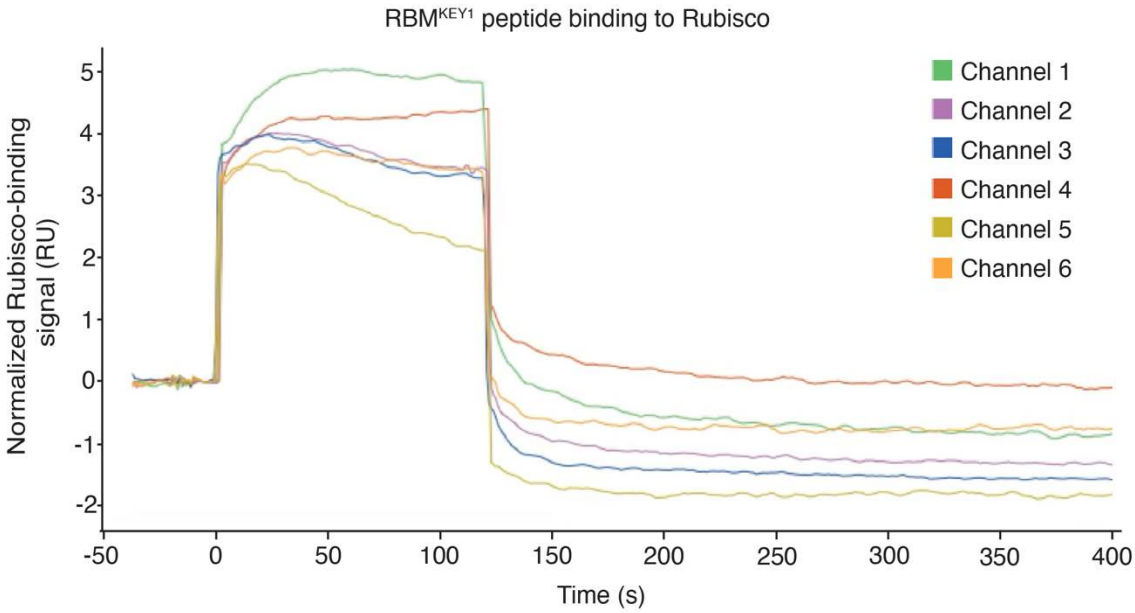


Extended Data Fig. 6. KEY1 localizes to the condensates throughout the cell, related to Fig. 5.

a, A cartoon shows Chlamydomonas cells synchronized in a diurnal cycle, where they grow in the light cycle and divide twice in rapid succession upon the shift from light to dark each day.

b, Confocal images of *key1-1*;*KEY1-Venus* cells throughout the cell cycle. At each time point, three representative cells are shown. Magenta shows chlorophyll autofluorescence mid-plane, and green shows KEY1-Venus mid-plane. All image acquisition and display parameters for the Venus channel are constant across images.

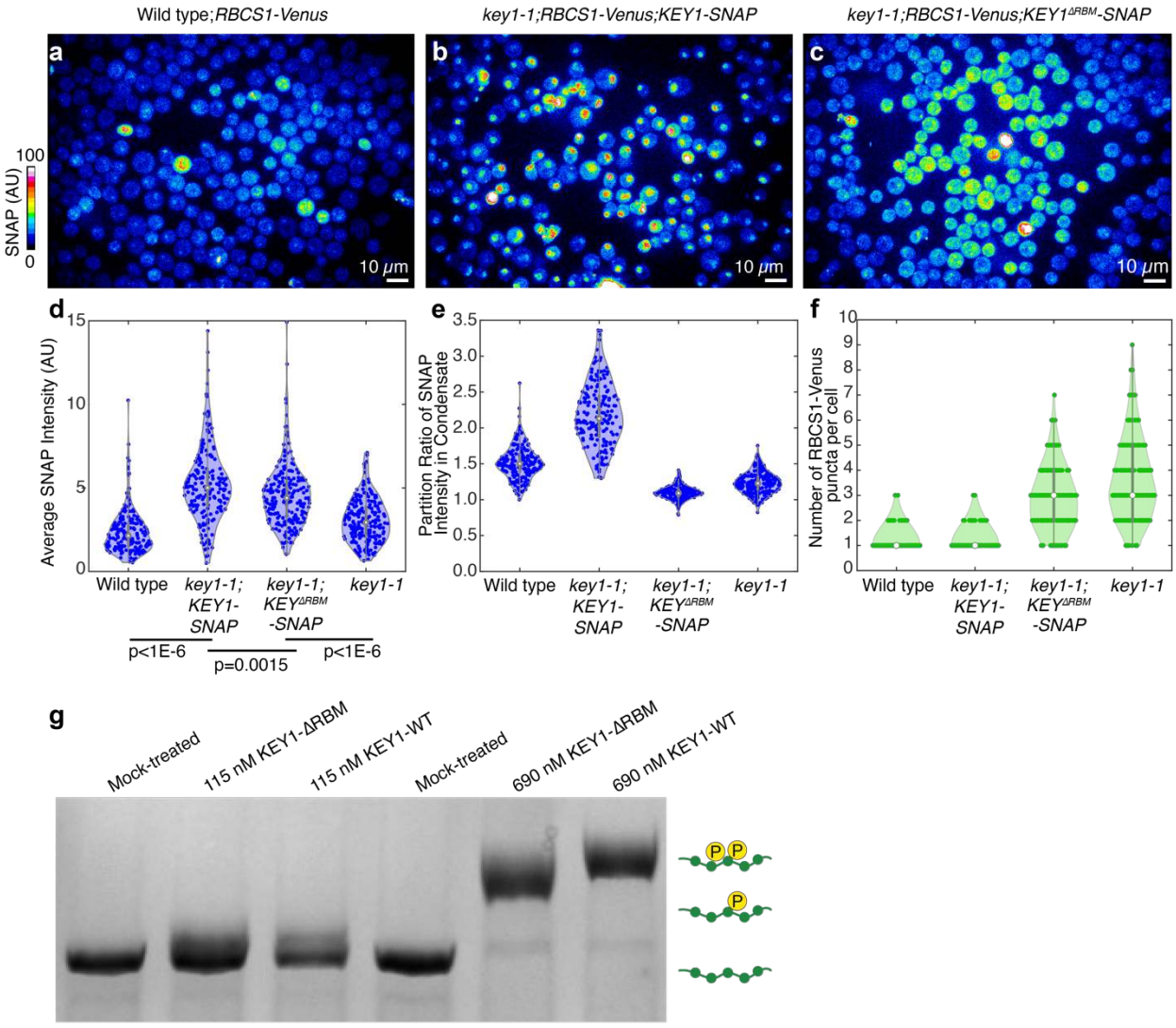
bioRxiv preprint doi: https://doi.org/10.1101/2025.10.09.681382; this version posted October 10, 2025. The copyright holder for this preprint (which was not certified by peer review) is the author/funder, who has granted bioRxiv a license to display the preprint in perpetuity. It is made available under a CC-BY 4.0 International license.



Extended Data Fig. 7. The Rubisco-binding motif of KEY1 directly binds to Rubisco holoenzyme, related to Fig. 5.

Double-subtracted sensorgrams showing the normalized binding signal of the RBM^{KEY1} peptide to Rubisco on each of the six channels (see also Methods). RU, response unit.

bioRxiv preprint doi: https://doi.org/10.1101/2025.10.09.681382; this version posted October 10, 2025. The copyright holder for this preprint (which was not certified by peer review) is the author/funder, who has granted bioRxiv a license to display the preprint in perpetuity. It is made available under a CC-BY 4.0 International license.



875

bioRxiv preprint doi: https://doi.org/10.1101/2025.10.09.681382; this version posted October 10, 2025. The copyright holder for this preprint (which was not certified by peer review) is the author/funder, who has granted bioRxiv a license to display the preprint in perpetuity. It is made available under a CC-BY 4.0 International license.

Extended Data Fig. 8. A Rubisco-binding motif promotes targeting of KEY1 to the condensate, related to Fig. 5.

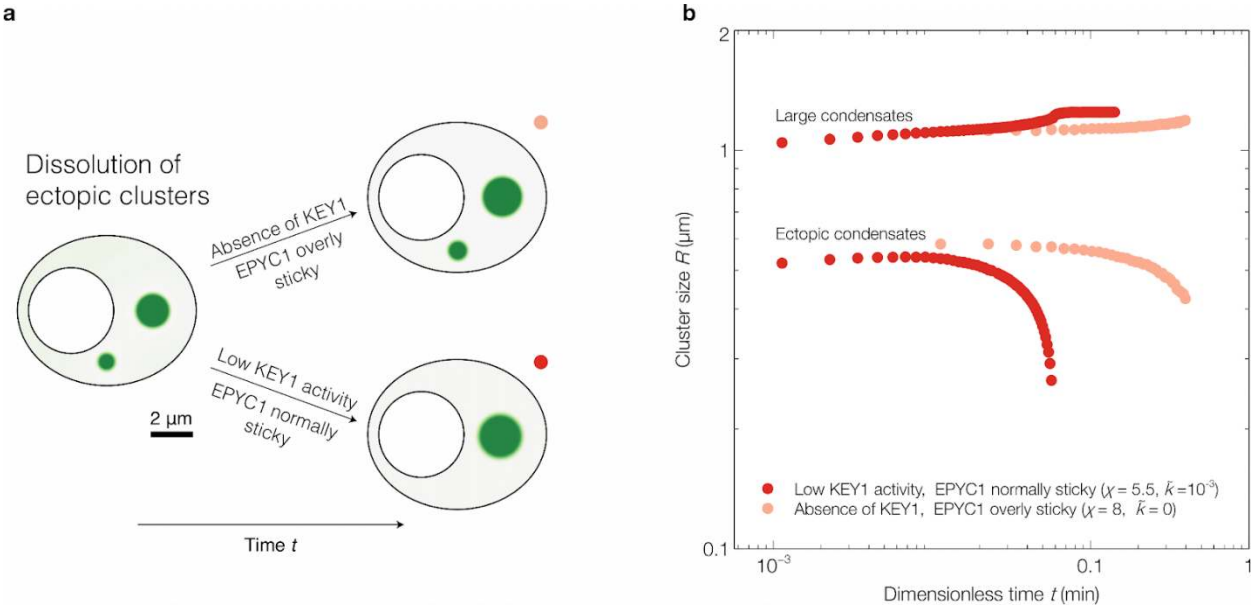
a-**c**, Full fields of view of maximum z-projection of SNAP-stained cells from which representative individual cells were shown in Fig. 5a. Shown are wild type (**a**), *key1-1*;*KEY1-SNAP* (**b**), and *key1-1*;*KEY1*$^{\Delta RBM}$*-SNAP* (**c**) all expressing RBCS1-Venus. The color bar indicates SNAP intensity. All image acquisition and display parameters are identical between the three images.

d-**e**, Violin plots showing average SNAP intensity in the cell (**d**) and partition ratio of SNAP intensity into pyrenoid condensate (**e**) in the cells expressing RBCS1-Venus with the background of wild type (n = 188 cells), *key1-1*;*KEY1-SNAP* (n = 188 cells), *key1-1*;*KEY1*$^{\Delta RBM}$*-SNAP* (n = 215 cells), and *key1-1* mutant (n=208 cells). Partition ratio of SNAP intensity is calculated as the mean intensity inside the condensate divided by the mean intensity outside the condensate; a partition ratio of 1 indicates no enrichment. P-values were calculated using a two-sided t-test.

f, Violin plot showing the number of pyrenoid condensates (visualized by RBCS1-Venus) per cell in the background of wild type (n = 188 cells), *key1-1*;*KEY1-SNAP* (n = 188 cells), *key1-1*;*KEY1*$^{\Delta RBM}$*-SNAP* (n = 215 cells) and *key1-1* mutant (n = 208 cells).

g, A Phos-tag gel stained with Coomassie of in vitro activity assay with KEY1-WT and KEY1-ΔRBM on EPYC1-GFP.

bioRxiv preprint doi: https://doi.org/10.1101/2025.10.09.681382; this version posted October 10, 2025. The copyright holder for this preprint (which was not certified by peer review) is the author/funder, who has granted bioRxiv a license to display the preprint in perpetuity. It is made available under a CC-BY 4.0 International license.



Extended Data Fig. 9. Ectopic clusters dissolve more slowly in the absence of KEY1. **a,** Dynamical simulations of our model starting from an initial condition with a small ectopic condensate and a large condensate located in the canonical pyrenoid position. Top: without KEY1 activity ($\tilde{k} = 0$) EPYC1 is overly sticky ($\chi = 8$), and the small condensate does not dissolve over time. Bottom: at low KEY1 activity ($\tilde{k} = 10^{-3}$), EPYC1 has normal stickiness ($\chi = 5.5$) and the small ectopic condensate dissolves over time (Fig. 6g). **b,** Large and ectopic cluster size as a function of time for the two cases shown in panel a.

bioRxiv preprint doi: https://doi.org/10.1101/2025.10.09.681382; this version posted October 10, 2025. The copyright holder for this preprint (which was not certified by peer review) is the author/funder, who has granted bioRxiv a license to display the preprint in perpetuity. It is made available under a CC-BY 4.0 International license.

References

1. Brangwynne, C.P. *et al.* Germline P granules are liquid droplets that localize by controlled dissolution/condensation. *Science* **324**, 1729-1732 (2009).
2. Shin, Y. & Brangwynne, C.P. Liquid phase condensation in cell physiology and disease. *Science* **357** (2017).
3. Banani, S.F., Lee, H.O., Hyman, A.A. & Rosen, M.K. Biomolecular condensates: organizers of cellular biochemistry. *Nat Rev Mol Cell Biol* **18**, 285-298 (2017).
4. Boeynaems, S. *et al.* Phase separation in biology and disease; current perspectives and open questions. *J Mol Biol* **435**, 167971 (2023).
5. Brangwynne, C.P., Mitchison, T.J. & Hyman, A.A. Active liquid-like behavior of nucleoli determines their size and shape in Xenopus laevis oocytes. *Proc Natl Acad Sci U S A* **108**, 4334-4339 (2011).
6. Pedley, A.M. *et al.* Purine biosynthetic enzymes assemble into liquid-like condensates dependent on the activity of chaperone protein HSP90. *J Biol Chem* **298**, 101845 (2022).
7. Wang, B. *et al.* Liquid-liquid phase separation in human health and diseases. *Signal Transduct Target Ther* **6**, 290 (2021).
8. Aoki, S.T. *et al.* C. elegans germ granules require both assembly and localized regulators for mRNA repression. *Nat Commun* **12**, 996 (2021).
9. Protter, D.S.W. & Parker, R. Principles and properties of stress granules. *Trends Cell Biol* **26**, 668-679 (2016).
10. Zhao, E.M. *et al.* Light-based control of metabolic flux through assembly of synthetic organelles. *Nat Chem Biol* **15**, 589-597 (2019).
11. Hnisz, D., Shrinivas, K., Young, R.A., Chakraborty, A.K. & Sharp, P.A. A phase separation model for transcriptional control. *Cell* **169**, 13-23 (2017).
12. Strom, A.R. *et al.* Phase separation drives heterochromatin domain formation. *Nature* **547**, 241-245 (2017).
13. Larson, A.G. *et al.* Liquid droplet formation by HP1alpha suggests a role for phase separation in heterochromatin. *Nature* **547**, 236-240 (2017).
14. Alberti, S., Gladfelter, A. & Mittag, T. Considerations and challenges in studying liquid-liquid phase separation and biomolecular condensates. *Cell* **176**, 419-434 (2019).
15. Li, Q., Liu, Y. & Zhang, X. Biomolecular condensates in plant RNA silencing: insights into formation, function, and stress responses. *Plant Cell* **36**, 227-245 (2024).
16. Su, X. *et al.* Phase separation of signaling molecules promotes T cell receptor signal transduction. *Science* **352**, 595-599 (2016).
17. Formicola, N., Vijayakumar, J. & Besse, F. Neuronal ribonucleoprotein granules: dynamic sensors of localized signals. *Traffic* **20**, 639-649 (2019).
18. Lyon, A.S., Peeples, W.B. & Rosen, M.K. A framework for understanding the functions of biomolecular condensates across scales. *Nat Rev Mol Cell Biol* **22**, 215-235 (2021).
19. Riback, J.A. *et al.* Stress-Triggered Phase Separation Is an Adaptive, Evolutionarily Tuned Response. *Cell* **168**, 1028-1040 e1019 (2017).
20. Emenecker, R.J., Holehouse, A.S. & Strader, L.C. Biological Phase Separation and Biomolecular Condensates in Plants. *Annu Rev Plant Biol* **72**, 17-46 (2021).
21. Lafontaine, D.L.J., Riback, J.A., Bascetin, R. & Brangwynne, C.P. The nucleolus as a multiphase liquid condensate. *Nat Rev Mol Cell Biol* **22**, 165-182 (2021).
22. Pedley, A.M., Pareek, V. & Benkovic, S.J. The Purinosome: A Case Study for a Mammalian Metabolon. *Annu Rev Biochem* **91**, 89-106 (2022).
23. Lim, S. & Clark, D.S. Phase-separated biomolecular condensates for biocatalysis. *Trends Biotechnol* **42**, 496-509 (2024).

bioRxiv preprint doi: https://doi.org/10.1101/2025.10.09.681382; this version posted October 10, 2025. The copyright holder for this preprint (which was not certified by peer review) is the author/funder, who has granted bioRxiv a license to display the preprint in perpetuity. It is made available under a CC-BY 4.0 International license.

24. Hyman, A.A., Weber, C.A. & Julicher, F. Liquid-liquid phase separation in biology. *Annu Rev Cell Dev Biol* **30**, 39-58 (2014).
25. Mittag, T. & Pappu, R.V. A conceptual framework for understanding phase separation and addressing open questions and challenges. *Mol Cell* **82**, 2201-2214 (2022).
26. Li, P. *et al.* Phase transitions in the assembly of multivalent signalling proteins. *Nature* **483**, 336-340 (2012).
27. Nott, T.J. *et al.* Phase transition of a disordered nuage protein generates environmentally responsive membraneless organelles. *Mol Cell* **57**, 936-947 (2015).
28. Castellana, M. *et al.* Enzyme clustering accelerates processing of intermediates through metabolic channeling. *Nat Biotechnol* **32**, 1011-1018 (2014).
29. Buchner, A., Tostevin, F., Hinzpeter, F. & Gerland, U. Optimization of collective enzyme activity via spatial localization. *J. Chem. Phys.* **139**, 135101 (2013).
30. Derenzini, M., Montanaro, L. & Trere, D. What the nucleolus says to a tumour pathologist. *Histopathology* **54**, 753-762 (2009).
31. Thompson, E.D. & Wood, L.D. Pancreatic neoplasms with acinar differentiation: a review of pathologic and molecular features. *Arch Pathol Lab Med* **144**, 808-815 (2020).
32. Lee, D.S.W. *et al.* Size distributions of intracellular condensates reflect competition between coalescence and nucleation. *Nat Phys* **19**, 586-596 (2023).
33. Folkmann, A.W., Putnam, A., Lee, C.F. & Seydoux, G. Regulation of biomolecular condensates by interfacial protein clusters. *Science* **373**, 1218-1224 (2021).
34. Cochard, A. *et al.* RNA at the surface of phase-separated condensates impacts their size and number. *Biophysical Journal* **121**, 1675-1690 (2022).
35. Snead, W.T. *et al.* Membrane surfaces regulate assembly of ribonucleoprotein condensates. *Nature Cell Biology* **24**, 461-470 (2022).
36. Hur, W. *et al.* CDK-Regulated Phase Separation Seeded by Histone Genes Ensures Precise Growth and Function of Histone Locus Bodies. *Developmental Cell* **54**, 379-394.e376 (2020).
37. Hondele, M. *et al.* DEAD-box ATPases are global regulators of phase-separated organelles. *Nature* **573**, 144-148 (2019).
38. Banani, S.F. *et al.* Active RNA synthesis patterns nuclear condensates. *bioRxiv*, 2024.2010.2012.614958 (2024).
39. Rai, A.K., Chen, J.-X., Selbach, M. & Pelkmans, L. Kinase-controlled phase transition of membraneless organelles in mitosis. *Nature* **559**, 211-216 (2018).
40. Hofweber, M. & Dormann, D. Friend or foe-Post-translational modifications as regulators of phase separation and RNP granule dynamics. *J Biol Chem* **294**, 7137-7150 (2019).
41. Söding, J., Zwicker, D., Sohrabi-Jahromi, S., Boehning, M. & Kirschbaum, J. Mechanisms for active regulation of biomolecular condensates. *Trends Cell Biol* **30**, 4-14 (2020).
42. Glotzer, S.C., Di Marzio, E.A. & Muthukumar, M. Reaction-controlled morphology of phase-separating mixtures. *Phys Rev Lett* **74**, 2034-2037 (1995).
43. Berry, J., Brangwynne, C.P. & Haataja, M. Physical principles of intracellular organization via active and passive phase transitions. *Rep Prog Phys* **81**, 046601 (2018).
44. Bazant, M.Z. Thermodynamic stability of driven open systems and control of phase separation by electro-autocatalysis. *Faraday Discuss* **199**, 423-463 (2017).
45. Weber, C.A., Zwicker, D., Julicher, F. & Lee, C.F. Physics of active emulsions. *Rep Prog Phys* **82**, 064601 (2019).
46. Jülicher, F. & Weber, C.A. Droplet physics and intracellular phase separation. *Annual Review of Condensed Matter Physics* **15**, 237-261 (2024).
47. Demarchi, L., Goychuk, A., Maryshev, I. & Frey, E. Enzyme-enriched condensates show self-propulsion, positioning, and coexistence. *Phys Rev Lett* **130**, 128401 (2023).

bioRxiv preprint doi: https://doi.org/10.1101/2025.10.09.681382; this version posted October 10, 2025. The copyright holder for this preprint (which was not certified by peer review) is the author/funder, who has granted bioRxiv a license to display the preprint in perpetuity. It is made available under a CC-BY 4.0 International license.

48. Schede, H.H., Natarajan, P., Chakraborty, A.K. & Shrinivas, K. A model for organization and regulation of nuclear condensates by gene activity. *Nature Communications* **14**, 4152 (2023).
49. Zwicker, D., Decker, M., Jaensch, S., Hyman, A.A. & Jülicher, F. Centrosomes are autocatalytic droplets of pericentriolar material organized by centrioles. *Proceedings of the National Academy of Sciences* **111**, E2636-E2645 (2014).
50. Zwicker, D., Paulin, O.W. & ter Burg, C. Physics of droplet regulation in biological cells. *arXiv*, 2501.13639 (2025).
51. Sastre, J. *et al.* Size control and oscillations of active droplets in synthetic cells. *Nature Communications* **16**, 2003 (2025).
52. Freeman Rosenzweig, E.S. *et al.* The eukaryotic CO2-concentrating organelle is liquid-like and exhibits dynamic reorganization. *Cell* **171**, 148-162 e119 (2017).
53. Barrett, J., Girr, P. & Mackinder, L.C.M. Pyrenoids: CO2-fixing phase separated liquid organelles. *Biochim Biophys Acta Mol Cell Res* **1868**, 118949 (2021).
54. He, S., Crans, V.L. & Jonikas, M.C. The pyrenoid: the eukaryotic CO2-concentrating organelle. *Plant Cell* **35**, 3236–3259 (2023).
55. Mackinder, L.C. *et al.* A repeat protein links Rubisco to form the eukaryotic carbon-concentrating organelle. *Proc Natl Acad Sci U S A* **113**, 5958-5963 (2016).
56. Holdsworth, R.H. The isolation and partial characterization of the pyrenoid protein of Eremosphaera viridis. *J Cell Biol* **51**, 499-513 (1971).
57. Fei, C., Wilson, A.T., Mangan, N.M., Wingreen, N.S. & Jonikas, M.C. Modelling the pyrenoid-based CO2-concentrating mechanism provides insights into its operating principles and a roadmap for its engineering into crops. *Nat Plants* **8**, 583-595 (2022).
58. Wunder, T., Cheng, S.L.H., Lai, S.K., Li, H.Y. & Mueller-Cajar, O. The phase separation underlying the pyrenoid-based microalgal Rubisco supercharger. *Nat Commun* **9**, 5076 (2018).
59. He, S. *et al.* The structural basis of Rubisco phase separation in the pyrenoid. *Nat Plants* **6**, 1480-1490 (2020).
60. Ma, Y., Pollock, S.V., Xiao, Y., Cunnusamy, K. & Moroney, J.V. Identification of a novel gene, CIA6, required for normal pyrenoid formation in Chlamydomonas reinhardtii. *Plant Physiol* **156**, 884-896 (2011).
61. Itakura, A.K. *et al.* A Rubisco-binding protein is required for normal pyrenoid number and starch sheath morphology in Chlamydomonas reinhardtii. *Proc Natl Acad Sci U S A* **116**, 18445-18454 (2019).
62. Meyer, M.T. *et al.* Rubisco small-subunit alpha-helices control pyrenoid formation in Chlamydomonas. *Proc Natl Acad Sci U S A* **109**, 19474-19479 (2012).
63. Reddy, R.J. *et al.* Early signaling dynamics of the epidermal growth factor receptor. *Proc Natl Acad Sci U S A* **113**, 3114-3119 (2016).
64. Humphrey, S.J., Azimifar, S.B. & Mann, M. High-throughput phosphoproteomics reveals in vivo insulin signaling dynamics. *Nat Biotechnol* **33**, 990-995 (2015).
65. Turkina, M.V., Blanco-Rivero, A., Vainonen, J.P., Vener, A.V. & Villarejo, A. CO2 limitation induces specific redox-dependent protein phosphorylation in Chlamydomonas reinhardtii. *Proteomics* **6**, 2693-2704 (2006).
66. Wang, H. *et al.* The global phosphoproteome of Chlamydomonas reinhardtii reveals complex organellar phosphorylation in the flagella and thylakoid membrane. *Mol Cell Proteomics* **13**, 2337-2353 (2014).
67. Werth, E.G. *et al.* Probing the global kinome and phosphoproteome in Chlamydomonas reinhardtii via sequential enrichment and quantitative proteomics. *Plant J* **89**, 416-426 (2017).

bioRxiv preprint doi: https://doi.org/10.1101/2025.10.09.681382; this version posted October 10, 2025. The copyright holder for this preprint (which was not certified by peer review) is the author/funder, who has granted bioRxiv a license to display the preprint in perpetuity. It is made available under a CC-BY 4.0 International license.

68. Roustan, V. & Weckwerth, W. Quantitative phosphoproteomic and system-level analysis of TOR inhibition unravel distinct organellar acclimation in Chlamydomonas reinhardtii. *Front Plant Sci* **9**, 1590 (2018).
69. Goodstein, D.M. *et al.* Phytozome: a comparative platform for green plant genomics. *Nucleic Acids Res* **40**, D1178-1186 (2012).
70. Mackinder, L.C.M. *et al.* A spatial interactome reveals the protein organization of the algal CO2-concentrating mechanism. *Cell* **171**, 133-147 e114 (2017).
71. Li, X. *et al.* A genome-wide algal mutant library and functional screen identifies genes required for eukaryotic photosynthesis. *Nat Genet* **51**, 627-635 (2019).
72. Nagai, T. *et al.* A variant of yellow fluorescent protein with fast and efficient maturation for cell-biological applications. *Nat Biotechnol* **20**, 87-90 (2002).
73. Iwatate, R.J. *et al.* Covalent self-labeling of tagged proteins with chemical fluorescent dyes in BY-2 cells and Arabidopsis seedlings. *Plant Cell* **32**, 3081-3094 (2020).
74. Keppler, A. *et al.* A general method for the covalent labeling of fusion proteins with small molecules in vivo. *Nat Biotechnol* **21**, 86-89 (2003).
75. Hennacy, J.H. *et al.* SAGA1 and MITH1 produce matrix-traversing membranes in the CO(2)-fixing pyrenoid. *Nat Plants* **10**, 2038-2051 (2024).
76. Toyokawa, C., Yamano, T. & Fukuzawa, H. Pyrenoid starch sheath is required for LCIB localization and the CO2-concentrating mechanism in green algae. *Plant Physiol* **182**, 1883–1893 (2020).
77. Bernstein, E. Synchronous division in Chlamydomonas moewusii. *Science* **131**, 1528-1529 (1960).
78. Rooney, D.W., Yen, B.C. & Mikita, D.J. Synchronization of Chlamydomonas division with intermittent hypothermia. *Exp Cell Res* **65**, 94-98 (1971).
79. Strenkert, D. *et al.* Multiomics resolution of molecular events during a day in the life of Chlamydomonas. *Proc Natl Acad Sci U S A* **116**, 2374-2383 (2019).
80. Mitchell, M.C., Meyer, M.T. & Griffiths, H. Dynamics of carbon-concentrating mechanism induction and protein relocalization during the dark-to-light transition in synchronized Chlamydomonas reinhardtii. *Plant Physiol* **166**, 1073-1082 (2014).
81. Kinoshita, E., Takahashi, M., Takeda, H., Shiro, M. & Koike, T. Recognition of phosphate monoester dianion by an alkoxide-bridged dinuclear zinc(II) complex. *Dalton Trans*, 1189-1193 (2004).
82. Kinoshita, E., Kinoshita-Kikuta, E., Takiyama, K. & Koike, T. Phosphate-binding tag, a new tool to visualize phosphorylated proteins. *Mol Cell Proteomics* **5**, 749-757 (2006).
83. He, G. *et al.* Phase-separating pyrenoid proteins form complexes in the dilute phase. *Commun Biol* **6**, 19 (2023).
84. Xu, B. *et al.* Rigidity enhances a magic-number effect in polymer phase separation. *Nat Commun* **11**, 1561 (2020).
85. Meyer, M.T. *et al.* Assembly of the algal CO2-fixing organelle, the pyrenoid, is guided by a Rubisco-binding motif. *Sci Adv* **6**, eabd2408 (2020).
86. Zwicker, D., Hyman, A.A. & Julicher, F. Suppression of Ostwald ripening in active emulsions. *Phys Rev E Stat Nonlin Soft Matter Phys* **92**, 012317 (2015).
87. Wang, J.T. *et al.* Regulation of RNA granule dynamics by phosphorylation of serine-rich, intrinsically disordered proteins in C. elegans. *Elife* **3**, e04591 (2014).
88. Wippich, F. *et al.* Dual specificity kinase DYRK3 couples stress granule condensation/dissolution to mTORC1 signaling. *Cell* **152**, 791-805 (2013).
89. Colwill, K. *et al.* The Clk/Sty protein kinase phosphorylates SR splicing factors and regulates their intranuclear distribution. *EMBO J* **15**, 265-275 (1996).
90. Liu, J.-L. *et al.* Cell cycle-dependent localization of the CDK2-cyclin E complex in Cajal (coiled) bodies. *J Cell Sci* **113**, 1543-1552 (2000).

bioRxiv preprint doi: https://doi.org/10.1101/2025.10.09.681382; this version posted October 10, 2025. The copyright holder for this preprint (which was not certified by peer review) is the author/funder, who has granted bioRxiv a license to display the preprint in perpetuity. It is made available under a CC-BY 4.0 International license.

91. Milovanovic, D., Wu, Y., Bian, X. & De Camilli, P. A liquid phase of synapsin and lipid vesicles. *Science* **361**, 604-607 (2018).
92. UniProt, C. UniProt: the Universal Protein Knowledgebase in 2023. *Nucleic Acids Res* **51**, D523-D531 (2023).
93. Kropat, J. *et al.* A revised mineral nutrient supplement increases biomass and growth rate in Chlamydomonas reinhardtii. *Plant J* **66**, 770-780 (2011).
94. Wang, L. *et al.* A chloroplast protein atlas reveals punctate structures and spatial organization of biosynthetic pathways. *Cell* **186**, 3499-3518 e3414 (2023).
95. Kafri, M. *et al.* Systematic identification and characterization of genes in the regulation and biogenesis of photosynthetic machinery. *Cell* **186**, 5638-5655 e5625 (2023).
96. Jiang, X. & Stern, D. Mating and tetrad separation of Chlamydomonas reinhardtii for genetic analysis. *J Vis Exp* (2009).
97. Redekop, P. *et al.* Transcriptional regulation of photoprotection in dark-to-light transition—More than just a matter of excess light energy. *Science Advances* **8**, eabn1832 (2022).
98. Livak, K.J. & Schmittgen, T.D. Analysis of Relative Gene Expression Data Using Real-Time Quantitative PCR and the 2−ΔΔCT Method. *Methods* **25**, 402-408 (2001).
99. Shevchenko, A., Tomas, H., Havlis, J., Olsen, J.V. & Mann, M. In-gel digestion for mass spectrometric characterization of proteins and proteomes. *Nat Protoc* **1**, 2856-2860 (2006).
100. Dorfer, V. *et al.* MS Amanda, a universal identification algorithm optimized for high accuracy tandem mass spectra. *J Proteome Res* **13**, 3679-3684 (2014).
101. Eng, J.K., McCormack, A.L. & Yates, J.R. An approach to correlate tandem mass spectral data of peptides with amino acid sequences in a protein database. *J Am Soc Mass Spectrom* **5**, 976-989 (1994).
102. Lemma, B., Mitchell, N.P., Subramanian, R., Needleman, D.J. & Dogic, Z. Active microphase separation in mixtures of microtubules and tip-accumulating molecular motors. *Phys Rev X* **12** (2022).
103. Aymard, B., Vaes, U., Pradas, M. & Kalliadasis, S. A linear, second-order, energy stable, fully adaptive finite element method for phase-field modelling of wetting phenomena. *Journal of Computational Physics: X* **2** (2019).
104. Dong, S. On imposing dynamic contact-angle boundary conditions for wall-bounded liquid–gas flows. *Computer Methods in Applied Mechanics and Engineering* **247-248**, 179-200 (2012).

bioRxiv preprint doi: https://doi.org/10.1101/2025.10.09.681382; this version posted October 10, 2025. The copyright holder for this preprint (which was not certified by peer review) is the author/funder, who has granted bioRxiv a license to display the preprint in perpetuity. It is made available under a CC-BY 4.0 International license.

Methods

Strains and culture conditions

The *Chlamydomonas reinhardtii* strain cMJ030 (CC-4533) was the wild type for all experiments (hereafter WT). The *key1-1* and *key1-2* mutant strains were obtained from the CLiP mutant collection[71] and can be found at the Chlamydomonas Resource Center (ID: LMJ.RY0402.107748 and LMJ.RY0402.168949), which is funded by the US National Science Foundation. All strains were maintained at 19˚C in the dark or low light (~10 µmol photons/m^2/second) on 1.5% agar plates containing tris-acetate-phosphate (TAP) medium (pH 7.4) with revised trace elements[93].

For unsynchronized liquid cultures, the TAP medium was primed with a loopful of cells and was grown to ~4 × 10^6 cells/ml at 22 °C, shaking at 200 rpm under ~200 µmol photons/m^2/second white light in the air in an orbital incubator-shaker (Infors).

For synchronized liquid cultures, cells were first cultivated in the unsynchronized liquid cultures, as described above. Then, cells were inoculated with ~2 × 10^4 cells/mL in bottles with Tris-Phosphate (TP) or TAP medium, aerated with air, and mixed using a conventional magnetic stirrer at 200 rpm in growth chambers with a diurnal cycle for five to seven days for synchronization before sample collections. The diurnal cycle was set to a 12-hour light cycle with a temperature at 28˚C under ~200 µmol photons/m^2/second, and a 12-hour dark cycle with a temperature at 18˚C in the dark[79].

Co-immunoprecipitation and mass spectrometry to verify kinase KEY1 and EPYC1 interaction

Immunoprecipitation and mass spectrometry of Venus-3×FLAG-KEY1, Venus-3×FLAG-EPYC1, or Venus-3×FLAG was performed as described previously[94] with the following modification: a 40 cm long chromatography column was used. The column temperature was set at 45 °C and a two-hour gradient method with 300 nL/minute flow was used. The mass spectrometer was operated in data-dependent mode with a 120,000 resolution MS1 scan (positive mode, profile data type, AGC gain of 4e5, maximum injection time of 54 s and mass range of 375-1,500 m/z) in the Orbitrap followed by HCD fragmentation in Orbitrap with a 30,000 resolution MS2 scan and 30% collision energy.

Mutant genotype analysis

The cassette insertion site of the *key1-1* mutant strain (LMJ.RY0402.107748) was validated by PCR amplifications performed with the Phusion® High-Fidelity DNA Polymerase (New England BioLabs) and primer pairs 3676_F and CIB_5'_R, and 3673_F and CIB_5'_R for testing the 5' end of the insertion, and primer pairs 3785_R and CIB_3'_F, and 3809_R and CIB_3'_F for testing the 3' end of the insertion. The specific insertion site was detected and validated by Sanger sequencing (GENEWIZ) and whole genome sequencing as described in Kafri et al., 2023[95].

bioRxiv preprint doi: https://doi.org/10.1101/2025.10.09.681382; this version posted October 10, 2025. The copyright holder for this preprint (which was not certified by peer review) is the author/funder, who has granted bioRxiv a license to display the preprint in perpetuity. It is made available under a CC-BY 4.0 International license.

The cassette insertion site of the *key1-2* mutant strain (LMJ.RY0402.168949) was validated by PCR amplification performed with the Phusion® High-Fidelity DNA Polymerase (New England BioLabs), and primer pairs 949_CLiP_R and CIB_5'_R, and CIB_3'_F and 949_CLiP_F, and 4859-5018_F and 4859-5018_R. The specific insertion site was detected and validated by Sanger sequencing (GENEWIZ).

The presence of the insertion cassette in the rescued strains of *key1-1* was validated by PCR with the primers 3673_F and CIB_5'_R and the Phusion® High-Fidelity DNA Polymerase (New England BioLabs).

Transmission electron microscopy

The transmission electron microscopy experiment was performed as described in Hennacy et al., 2024[75]. Specifically, the samples for electron microscopy were prepared at room temperature and were nutated in 1 mL volumes during chemical treatments and washes unless otherwise noted. After the initial centrifugation for harvesting, all pelleting was done at 3000 × g for 1 minute. Approximately 50 × 10^6 cells were harvested at 1000 × g for 5 minutes and fixed in 2.5% glutaraldehyde in Tris-Phosphate medium (pH 7.4) for one hour. After three 5-minute washes in MilliQ water, the samples were treated with a freshly prepared solution of 1% OsO_4, 1.5% $K_3Fe(CN)_6$, and 2 mM $CaCl_2$. After four 5-minute washes in MilliQ water, the samples were serially dehydrated (5-minute incubations in 50%, 75%, 95%, and 100% ethanol, followed by two 10-minute incubations in 100% acetonitrile). The samples were then suspended in 50% acetonitrile, 17.5% Quetol 651, 22.5% nonenyl succinic anhydride, and 10% methyl-5-norbornene-2,3-dicarboxylic anhydride and were left uncapped and stationary overnight in a fume hood to allow for the evaporation of the acetonitrile. The samples were then embedded in epoxy resin containing 34% Quetol 651, 44% nonenyl succinic anhydride, 20% methyl-5-norbornene-2,3-dicarboxylic anhydride, and 2% catalyst dimethylbenzylamine. The resin mixture was refreshed daily for four subsequent days. After the final resin refresh, the pellets were resuspended in 300 µL of the resin mixture and centrifuged at 30°C for 20 minutes at 10,500 rpm in a swinging bucket rotor for microfuge tubes. They were then cured at 65°C for 48 hours. Subsequently, ultramicrotomy was performed using a DiaTome diamond knife on a Leica UCT Ultramicrotome at the Imaging and Analysis Center, Princeton University, and imaging was performed on a CM100 transmission electron microscope (Philips) at 80 kV or CM200 at 200 kV.

Mating

The *key1-1*;*RBCS1-Venus* strain was generated by mating the strains *key1-1* (mt-) and RBCS1-Venus (mt+), which was generated by mating the strain RBCS1-Venus (mt-) in a cMJ030 background with the wild-type strain CC-1690 (mt+). The mating protocol was adapted from Jiang and Stern 2009[96]. However, zygotes were grown to colonies instead of dissecting tetrads, and then streaked to single colonies. These single colonies were first screened by a Typhoon scanner (GE Healthcare) for RBCS1-Venus fluorescent and then by PCR for the correct genotype of *key1-1* with the primers 3676_F and 3785_R.

bioRxiv preprint doi: https://doi.org/10.1101/2025.10.09.681382; this version posted October 10, 2025. The copyright holder for this preprint (which was not certified by peer review) is the author/funder, who has granted bioRxiv a license to display the preprint in perpetuity. It is made available under a CC-BY 4.0 International license.

Plasmid Construction and Cloning

The open reading frame of *KEY1* was cloned by PCR with the primers KEY1_473-491_adapter_F and KEY1_5967-5984_adapter_R and the KOD Xtreme™ Hot Start DNA Polymerase (TOYOBO) with the genomic DNA of WT strain (cMJ030) as a template. The plasmid pRAM118-KEY1 was generated using the In-fusion® Snap Assembly Master Mix (Takara) with endonuclease HpaI-linearized pRAM118 backbone and the open reading frame of *KEY1*. The sequence of the open reading frame of *KEY1* amplified was verified by Sanger sequencing (GENEWIZ) in the pRAM118-KEY1 plasmid. This generated pRAM118-KEY1 plasmid has a sequence encoding a Venus protein followed by a 3×FLAG tag on the backbone, which follows the *KEY1* gene with a short linker fragment in between.

The native promoter of *KEY1* was cloned by PCR with the primers KEY1_US-2141_BstBI_F and KEY1_584_AgeI_R and the Phusion® High-Fidelity DNA Polymerase (New England BioLabs) with the genomic DNA of WT strain (cMJ030) as a template. The plasmid pRAM118-pro+KEY1 was generated using the In-fusion® Snap Assembly Master Mix (Takara) with endonucleases BstBI and AgeI linearized pRAM118-KEY1 backbone and the native promoter of KEY1 amplified. The sequence of the native promoter of KEY1 amplified was verified by Sanger sequencing (GENEWIZ) in the pRAM118-pro+KEY1 plasmid. This generated pRAM118-pro+KEY1 plasmid has a sequence encoding a Venus protein followed by a 3×FLAG tag on the backbone, which follows the *KEY1* gene with a short linker fragment in between.

The plasmid pRAM118-pro+KEY1-SNAP was generated by GenScript Biotech by replacing the Venus-tag encoding sequence in the plasmid pRAM118-pro+KEY1 with codon-optimized SNAP-tag encoding sequence[73]. This generated pRAM118-pro+KEY1-SNAP plasmid has a sequence encoding a 3×FLAG on the backbone, which follows the SNAP-tag encoding gene with a short linker fragment in between. The SNAP-tag encoding gene was codon-optimized for Chlamydomonas.

The plasmid pRAM118-pro+KEY1_ΔRBM-SNAP was generated by GenScript Biotech by replacing the candidate Rubisco-binding motif WRVDI encoding sequence (TGGCGGGTAGACATC) to AAVDD encoding sequence (GCGGCGGTAGACGAC). This generated pRAM118-pro+KEY1_ΔRBM-SNAP plasmid has a sequence encoding a 3×FLAG on the backbone, which follows the SNAP-tag encoding gene with a short linker fragment in between. The SNAP-tag encoding gene was codon-optimized for Chlamydomonas.

The plasmid pRAM118-proEPYC1-EPYC1-Venus was generated by GenScript Biotech by replacing the PsaD promoter in the plasmid pRAM118 with the synthesized EPYC1 native promoter (2000 bp upstream of ATG). This generated pRAM118-proEPYC1-EPYC1-Venus plasmid has a sequence encoding a Venus protein followed by a 3×FLAG tag on the backbone, which follows the *EPYC1* gene with a short linker fragment in between.

The plasmid pRAM118-proEPYC1-EPYC1-Astring-Venus was generated by GenScript Biotech by changing all the Serine or Threonine encoding sequences to Alanine encoded sequences

bioRxiv preprint doi: https://doi.org/10.1101/2025.10.09.681382; this version posted October 10, 2025. The copyright holder for this preprint (which was not certified by peer review) is the author/funder, who has granted bioRxiv a license to display the preprint in perpetuity. It is made available under a CC-BY 4.0 International license.

(after the predicted transit peptide encoding sequences). In details, it is changing "GGCAGCTGGCGCGAGTCTTCCACTGCCACCGTGCAGGCCAGGTGAGCACACTTCTGCAG CTATGAGATGCATCTGGGTCCAGCTTAAAGCGGCTCGCGTTGTGTGGCGCGCCGCGATCC CTTATCCGCTCGCCTGCCAGCCGGGCCTTTTCGCACTTGTTTCCTAAGTCAAGTTCGAACC TGCAGCTGGCTGTGCATATCTTGCTAAGTGATAGCGCGGTTGTACGCGGTTTGAGTACGCT GCTCAACTGGTGTACTGACACGTTTGCTTGCCGTTTCCCCTGGTGCCCCTTCGCCCCTGCA GCCGCGCCTCGTCGGCCACCAACCGCGTGAGCCCCACCCGCTCCGTCCTGCCCGCCAAC TGGCGCCAGGAGCTGGAGAGCCTGCGCAACGGCAACGGCTCCTCCTCGGCTGCCTCGTC GGCCCCCGCCCCGGCCCGCTCCTCGTCGGCCAGCTGGCGCGACGCCGCCCCGGCCTCG TCGGCCCCTGCCCGCTCCAGCTCTGCCTCCAAGAAGGCCGTGACCCCGTCGCGCAGCGC CCTGCCCTCCAACTGGAAGCAGGAGCTGGAGAGCCTGCGCAGCAGCTCCCCCGCCCCCG CCTCGTCGGCCCCCGCCCCGGCCCGCTCCTCGTCGGCCAGCTGGCGTGATGCCGCCCC GGCCTCGTCGGCCCCCGCCCGCTCCAGCTCCTCCAAGAAGGCTGTGACCCCGTCGCGCA GCGCCCTGCCCTCCAACTGGAAGCAGGAGCTGGAGAGCCTGCGCAGCAGCTCCCCCGCC CCCGCCTCGTCGGCCCCTGCCCCGGCCCGCTCCTCGTCGGCCAGCTGGCGTGACGCCG CCCCGGCCTCGTCGGCCCCTGCCCGCTCCAGCTCTGCCTCCAAGAAGGCCGTGACCCCG TCGCGCAGCGCCCTGCCCTCCAACTGGAAGCAGGAGCTGGAGAGCCTGCGCAGCAACTC CCCTGCCCCCGCCTCGTCGGCCCCTGCCCCGGCCCGCTCCTCGTCGGCCAGCTGGCGTG ACGCCCCCGCCTCGAGCTCCAGCTCGAGCGCCGACAAGGCCGGCACCAACCCCTGGACT GGCAAGTCCAAGCCCGAGATCAAGCGCACCGCCCTGCCC" to "GGCGCCTGGCGCGAGGCCGCGGCCGCCGCCGTGCAGGCCGCGTGAGCACACTTCTGCA GCTATGAGATGCATCTGGGTCCAGCTTAAAGCGGCTCGCGTTGTGTGGCGCGCCGCGATC CCTTATCCGCTCGCCTGCCAGCCGGGCCTTTTCGCACTTGTTTCCTAAGTCAAGTTCGAAC CTGCAGCTGGCTGTGCATATCTTGCTAAGTGATAGCGCGGTTGTACGCGGTTTGAGTACG CTGCTCAACTGGTGTACTGACACGTTTGCTTGCCGTTTCCCCTGGTGCCCCTTCGCCCCTG CAGCCGCGCCGCGGCGGCCGCCAACCGCGTGGCCCCCGCCCGCGCCGTCCTGCCCGCC AACTGGCGCCAGGAGCTGGAGGCCCTGCGCAACGGCAACGGCGCCGCCGCGGCTGCCG CGGCGGCCCCCGCCCCGGCCCGCGCCGCGGCGGCCGCCTGGCGCGACGCCGCCCCGG CCGCGGCGGCCCCTGCCCGCGCCGCCGCCGCCGCCAAGAAGGCCGTGGCCCCGGCGC GCGCCGCCCTGCCCGCCAACTGGAAGCAGGAGCTGGAGGCCCTGCGCGCCGCCGCCCC CGCCCCCGCCGCGGCTGCCCCCGCCCCGGCCCGCGCCGCGGCGGCCGCCTGGCGTGA TGCCGCCCCGGCCGCGGCGGCCCCCGCCCGCGCCGCCGCCGCCAAGAAGGCTGTGGCC CCGGCGCGCGCCGCCCTGCCCGCCAACTGGAAGCAGGAGCTGGAGGCCCTGCGCGCCG CCGCCCCCGCCCCCGCCGCGGCGGCCCCTGCCCCGGCCCGCGCCGCGGCGGCCGCCT GGCGTGACGCCGCCCCGGCCGCGGCGGCCCCTGCCCGCGCCGCCGCCGCCGCCAAGA AGGCCGTGGCCCCGGCGCGCGCCGCCCTGCCCGCCAACTGGAAGCAGGAGCTGGAGGC CCTGCGCGCCAACGCCCCTGCCCCCGCCGCGGCGGCCCCTGCCCCGGCCCGCGCCGCG GCGGCCGCCTGGCGTGACGCCCCCGCCGCGGCCGCCGCCGCGGCCGCCGACAAGGCC GGCGCCAACCCCTGGGCCGGCAAGGCCAAGCCCGAGATCAAGCGCGCCGCCCTGCCC". This generated pRAM118-proEPYC1-EPYC1-Astring-Venus plasmid has a sequence encoding a Venus protein followed by a 3×FLAG tag on the backbone, which follows the mutated *EPYC1* gene with a short linker fragment in between.

bioRxiv preprint doi: https://doi.org/10.1101/2025.10.09.681382; this version posted October 10, 2025. The copyright holder for this preprint (which was not certified by peer review) is the author/funder, who has granted bioRxiv a license to display the preprint in perpetuity. It is made available under a CC-BY 4.0 International license.

The plasmids generated for this study have been submitted to the Chlamydomonas Resource Center (www.chlamycollection.org), which is funded by the US National Science Foundation. The antibiotic resistances and other information of these plasmids are available in Supplementary Table 3.

All cloning of *KEY1* described in this study was based on the sequence of Cre01.g008550 in the *Chlamydomonas reinhardtii* v5.6 genome, prior to the release of the *Chlamydomonas reinhardtii* CC-4532 v6.1 genome. Specifically, there is a shift in the annotation of the start codon of the *KEY1* gene, which introduces an additional 58 amino acids at the N-terminus of the KEY1 protein in the v6.1 genome compared to the v5.6 genome. Importantly, in all our *KEY1* plasmid constructs used for *in vivo* experiments, expression was driven by the default native *KEY1* promoter, defined as the 2,000 bp genomic region upstream of the start codon in the v5.6 genome. Therefore, we expect that the translations were initiated correctly in our *in vivo* experiments. For the *in vitro* experiments, the KEY1 and KEY1$^{\Delta RBM}$ proteins we expressed in *E. coli* both lacked the 58 N-terminal amino acids annotated in the v6.1 genome. However, we expect that some or all of these amino acids encode the chloroplast transit peptide, and thus we don't expect a significant impact on the protein's function *in vitro*. Thus, the reannotation does not affect the expression, localization, or function of any of the KEY1 proteins analyzed in this study.

Transformation of *Chlamydomonas reinhardtii*

The strains *key1-1*;*EPYC1-Venus*, *key1-1*;*KEY1-Venus*, and *key1-1*;*KEY1-SNAP* were generated by transforming the plasmids pLM005-EPYC1, pRAM118-pro+KEY1 and pRAM118-pro+KEY1-SNAP into *key1-1* strain, respectively. The strains *key1-1*;*RBCS1-Venus*;*KEY1-SNAP* and *key1-1*;*RBCS1-Venus;KEY1$^{\Delta RBM}$-SNAP* were generated by transforming the plasmids pRAM118-pro+KEY1-SNAP and pRAM118-pro+KEY1_ΔRBM-SNAP into the *key1-1*;*RBCS1-Venus* strain, respectively. The *epyc1*;*EPYC1-Venus* and *epyc1*;*EPYC1^{phosphonull}-Venus* strains were generated by transforming the plasmid pRAM118-proEPYC1-EPYC1-Venus and pRAM118-proEPYC1-EPYC1-Astring-Venus into the *epyc1* mutant strain, respectively. Chlamydomonas transformations were performed as described in Wang et al., 2023[94]. pRAM118-pro+KEY1-SNAP was linearized by ScaI, and the other plasmids were linearized by EcoRV. The transformants were plated on the TAP agar medium with 20 μg mL^{-1} hygromycin. The single colonies of the transformants were screened by PCR.

The Chlamydomonas strains generated for this study have been submitted to the Chlamydomonas Resource Center (www.chlamycollection.org), which is funded by the US National Science Foundation. The accession numbers and the antibiotic resistances of these strains are available in Table S4.

RNA extraction and RT-qPCR

Cells of wild type, *key1-1*, *key1-2*, *key1-1;-KEY1-Venus*, and *key1-1;KEY1-SNAP* were grown and synchronized in diurnal cycles as described in previous section. Cell samples were collected at +11 hour time point in the light cycle. Total RNA was extracted using TRIzol™ reagent

bioRxiv preprint doi: https://doi.org/10.1101/2025.10.09.681382; this version posted October 10, 2025. The copyright holder for this preprint (which was not certified by peer review) is the author/funder, who has granted bioRxiv a license to display the preprint in perpetuity. It is made available under a CC-BY 4.0 International license.

(Invitrogen) following the manufacturer's protocol. For RT-qPCR, 100 ng of total RNA from each sample was used with the Luna® Universal One-Step RT-qPCR Kit (New England Biolabs) according to the manufacturer's instructions, and reactions were run on a QuantStudio™ 6 Real-Time PCR System (Applied Biosystems). G protein beta subunit-like polypeptide (*CBLP*) was used as the reference gene for all RT-qPCR analyses. cDNA of *KEY1* was amplified by primer pair Key1_P1Fw and Key1_p1Rv, while cDNA of *CBLP* was amplified by primer pair CBLP_FW and CBLP_RV[97] (See Supplementary Table 2). The relative expression level of each gene was calculated with the cycle threshold (CT) $2^{-\Delta\Delta CT}$ method[98].

Confocal microscopy for living cells

The wild-type strains expressing fluorescent proteins (RBCS1-Venus, EPYC1-Venus) were generated in Mackinder et al 2016[55] using the same method as described above. The strains can be obtained through the Chlamydomonas Resource Center under accession numbers CC-5357 (RBCS1-Venus) and CC-5359 (EPYC1-Venus). The *key1-1;EPYC1-Venus, key1-1*;*RBCS1-Venus, key1-1;RBCS1-Venus*;*KEY1-SNAP*, *key1-1*;*RBCS1-Venus;KEY1*$^{\Delta RBM}$*-SNAP, epyc1;EPYC1-Venus* and *epyc1;EPYC1*^{phosphonull}*-Venus* strains were generated as described above.

For observing condensate size and number, cells were grown in unsynchronized liquid culture conditions as described above and transferred to TP media 6 hours before imaging.

For observing pyrenoid phase behaviors during cell division and at the start of the day, cells were grown in diurnal growth conditions in TAP media as described above for 5 days or longer. The cultures were maintained at ~2 × 10^6 cells/mL through periodic dilution. On the day of imaging, 200 µL of culture was removed from the incubator 1-4 hours before darkness.

For observing the subcellular localization of KEY1 or KEY1 $^{\Delta RBM}$, we used TMR-STAR SNAP-tag dye (New England BioLabs) to label KEY1-SNAP and KEY1 $^{\Delta RBM}$-SNAP. Following the protocol from the manufacturer, we dissolved the dye in DMSO for a solution of 0.6 mM SNAP-tag and stored it at -20C. 1 mL of cell culture was collected and spun down at 600 × g for 5 min in a table-top centrifuge. We diluted the dye 1:200 into TP media with 1% BSA and resuspended the pellet in 200 µL of the dye solution. We incubated the cell culture of wild type*, key1-1;RBCS1-Venus;KEY1-SNAP* and *key1-1;RBCS1-Venus;KEY1* $^{\Delta RBM}$*-SNAP* with the dye for 30 minutes with shaking and constant light. Then the cells were spun down and washed 3 times with TP. On the final spin, the cells were resuspended in TP with 1% BSA and incubated with shaking for 1 hour. Then the cells were spun down and resuspended in TP media for imaging.

For imaging, 200 µL of cell samples was added to an ibidi 8 well plate and allowed to settle for 5 minutes. The liquid media was then aspirated to leave a layer of cells on the glass. Next, TP media with 2% low melting point agarose was added at 35-40˚C to the well to trap the cells on the glass surface. For timelapse imaging, after 5 minutes when the agar was solid, 200 µL of mineral oil was added to prevent evaporation. Ensuring the mineral oil wetted the entire well was essential for stable, long timelapse imaging.

bioRxiv preprint doi: https://doi.org/10.1101/2025.10.09.681382; this version posted October 10, 2025. The copyright holder for this preprint (which was not certified by peer review) is the author/funder, who has granted bioRxiv a license to display the preprint in perpetuity. It is made available under a CC-BY 4.0 International license.

With the following exceptions, all microscopy images were taken on a VT-iSIM super-resolution spinning disk confocal on an Olympus iX83 body equipped with a Hamamatsu Orca Quest sCMOS camera and run using VisiView control software. Venus fluorescence was excited with a 514 nm laser and collected at 545/50 nm. Chlorophyll autofluorescence was excited with a 642 nm laser and collected at 700/75 nm. Images shown in Fig. 2 and Supplementary Video 2 were taken on a Zeiss 980 Laser Scanning Confocal Microscope with AiryScan. Images shown in Extended Data Fig. 2 and Supplementary Video 3 were taken on a Nikon A1R scanning confocal microscope.

For analyzing condensate size and number, cell samples were imaged on a VT-iSIM with a 60× 1.42 NA oil immersion objective (Olympus: UPLXAPO60XO). The z-step was 0.3 µm. For each strain, the scan-slide function was used in VisiView to obtain images for a large number of cells. These images were subsequently stitched together in VisiView and saved as series of tif files. Analysis was performed using custom MATLAB scripts (https://github.com/linnealemma/KEY1_He-Lemma-etal). Briefly, the Chlorophyll channel was used to identify individual cells and measure their volume using intensity-based thresholding and MATLAB regionprops3 function. Then, intensity-based thresholding and regionprops3 were applied to the Venus channel for each cell to identify the condensate size and number. These results for each strain were plotted as violin plots. P-values were calculated using the t-test function in MATLAB.

For analyzing the condensate behavior at the start of the day, cells were imaged on a VT-iSIM microscope with 100× 1.3 NA silicone immersion objective (Olympus: UPLSAPO100XS). The z-step was 0.3 µm. For each strain, a field of view with many cells was defined and the stage positions were stored in VisiView. Every hour, a z-stack was obtained with the same laser intensities. To mimic light conditions from the chamber, the brightfield lamp intensity was adjusted to 150 µmol and turned on between hourly acquisitions. FIJI was used to process z-stack acquisition files. To quantify condensate size, the max-z projection was created for Venus channel and the condensates were manually outlined using the ImageJ polygon tool and ROI manager. To quantify condensate number, the look-up-tables were set equal for all time points and then condensates were counted manually by scrubbing through the z-stack for each cell.

For observing pyrenoid phase behaviors of wild-type and *key1-1* mutant cells with EPYC1-Venus during cell division, cell samples were imaged every 90 s on a Zeiss 980 AiryScan confocal microscope in AiryScan mode using a 100× 1.46 oil immersion objective (Zeiss: 420792-9800-000) with pinhole size 97 µm. Venus fluorescence and chlorophyll autofluorescence were excited with 508 nm and 640 nm lasers, and collected at 524 nm and 667 nm with a spectral detector respectively. The z-step was 1 µm. Zeiss Definite Focus system was used and cells were imaged for 4-8 hours.

For observing pyrenoid phase behaviors of wild-type and *key1-1* mutant cells with RBCS1-Venus during cell division, cell samples were imaged at room temperature every 20 minutes for 2 hours and then every 5 minutes for 6 hours on a Nikon A1R scanning confocal microscope in resonant

bioRxiv preprint doi: https://doi.org/10.1101/2025.10.09.681382; this version posted October 10, 2025. The copyright holder for this preprint (which was not certified by peer review) is the author/funder, who has granted bioRxiv a license to display the preprint in perpetuity. It is made available under a CC-BY 4.0 International license.

scanning mode using Nikon Elements software, a 100× 1.49 NA objective, and pinhole size 49.81 µm. Venus fluorescence was excited with 514 nm laser and collected at 585/65 nm on a GaAsP detector. Chlorophyll autofluorescence was excited with a 640 nm laser and collected with a long pass 650 nm on a PMT HV detector. Images were collected with 4× line-averaging and 0.5 µm z-steps driven by Nikon A1 Piezo z-drive through the cell volume. The Nikon perfect focus system was enabled. Multiple positions were defined to capture both wild-type and *key1* mutant cell divisions on the same day. For visualization, Nikon AI denoise algorithm was used. The unprocessed images were used for statistical analysis. Similar acquisition parameters on the same Nikon A1R were also used to observe pyrenoid phase behaviors of KEY1 rescued strain, with wild-type and *key1-1* mutant controls.

For analyzing pyrenoid phase behaviors in all cell types, the 4D tiff stacks were imported into FIJI. Cells were manually cropped and saved in separate folders as a series of tif files. Division times were manually determined as the frame when the cleavage furrow split the chloroplast(s). Analysis was performed on these images using custom MATLAB scripts (https://github.com/linnealemma/KEY1_He-Lemma-etal). Briefly, for each parent cell, the Chlorophyll channel of images throughout cell division was used to mask the Venus channel which limited analysis to signal within the chloroplast(s). The Venus images were corrected for photobleaching using a simple ratio, which assumes that protein concentration is constant throughout the acquisition. The Venus channel was then thresholded using a value that was constant for a single acquisition. The MATLAB function regionprops3 was used with the raw and thresholded images to identify the condensate(s) in each frame and measure the volume inside and outside the dense phase.

For analyzing the subcellular localization of KEY1 or KEY1 $^{\Delta RBM}$, cell samples were imaged on a VT-iSIM microscope using excitation and emission settings for Venus and Chlorophyll as described above. Additionally, the TMR-SNAP dye labeling KEY1 was excited with a 561 nm laser and collected at 595/40 nm. A 60× 1.46 NA oil immersion objective was used for imaging. The z-step was 0.3 µm. Analysis was performed on these images using custom MATLAB scripts (https://github.com/linnealemma/KEY1_He-Lemma-etal). Briefly, the same process was used to identify chloroplasts and condensates as for analyzing condensate size and number (above). The SNAP channel was then used to calculate the intensity in the whole chloroplast and the partitioning between the condensate and the non-condensate chloroplast for each strain.

Spot test growth assays

WT, *key1-1*, *key1-2*, and complemented cell lines were grown in TAP under 200 µmol photons/m^2/second white light until ~2 ×10^6 cells mL^{-1}, washed once with TP, resuspended in TP to a concentration of 2 ×10^5 cells mL^{-1}, then serially diluted 1:10 three times. 10 µl of each dilution was spotted onto four TP plates or TAP plates and incubated in the air (0.04% CO_2), 3% CO_2 or 0.004% CO_2 under 200 µmol photons/m^2/second white light or in the dark. The plates were imaged after 6 days (TP and TAP-dark, air), 8 days (TP, 3% CO_2), or 10 days (TP, 0.004% CO_2).

Immunoblotting Analysis

bioRxiv preprint doi: https://doi.org/10.1101/2025.10.09.681382; this version posted October 10, 2025. The copyright holder for this preprint (which was not certified by peer review) is the author/funder, who has granted bioRxiv a license to display the preprint in perpetuity. It is made available under a CC-BY 4.0 International license.

Cell lysates for direct immunoblot analysis were prepared as described in Meyer et al., 2020[85], with adaptations. Specifically, 10 mL of unsynchronized TAP-grown cell cultures were pelleted at 1000 × g at 4°C for 5 minutes and resuspended in 300 µL of lysis buffer containing 5 mM HEPES-KOH (pH 7.5), 100 mM dithiothreitol, 100 mM Na_2CO_3, 2% SDS, 12% sucrose, 1 mM NaF, 0.3 mM Na_3VO_4, 2× Halt™ Protease Inhibitor Cocktail, EDTA-free (Thermo Fisher Scientific), and 2× Halt™ Phosphatase Inhibitor Single-Use Cocktail (Thermo Fisher Scientific). For the diurnal western blot, 10 mL of synchronized TAP-grown cell cultures were pelleted every hour. The pellets were then weighed and lysis buffer was added for a final concentration of 0.05g /300 µL.

Then, for both unsynchronized and diurnal samples, the lysates were transferred to 1.5 mL microcentrifuge tubes and heat-denatured in a thermomixer at 37°C, 750 rpm for 10 minutes before being centrifuged at 16,000 × g at 4 °C for 5 minutes. The supernatant was aliquoted, flash-frozen in liquid nitrogen, and stored at −80 °C until use.

Cell lysates for subsequent kinase or phosphatase treatments are prepared as described in Mackinder et al., 2016[55], with adaptations. Specifically, cells were harvested by centrifugation at 1000 × g at 4°C for 5 minutes, and then re-suspended in ice-cold lysis buffer containing 50 mM HEPES (pH 6.8), 50 mM KOAc, 2 mM $Mg(OAc)_2$, 1 mM $CaCl_2$, 200 mM sorbitol, 1 mM NaF, 0.3 mM Na_3VO_4, 2× Halt™ Protease Inhibitor Cocktail, EDTA-free (Thermo Fisher Scientific), and 2× Halt™ Phosphatase Inhibitor Single-Use Cocktail (Thermo Fisher Scientific) before being lysed by sonication (6 × 30-second bursts of 20 microns amplitude, with 15 s on ice between bursts; Soniprep 150, MSE UK, London, UK).

For the unsynchronized lysate (Fig. 3a), gel-loading was normalized by total chlorophyll a+b content as described in Meyer et al. 2020[85].

For electrophoresis, 30 µL of lysate sample (with or without kinase or phosphatase treatments) was mixed with 10 µL 4 × SDS-PAGE buffer (Bio-Rad) containing 100 mM DTT (Sigma-Aldrich) followed by denaturation by heating at 70°C for 10 minutes. Then, a 12.5 µL denatured protein sample was loaded into a well of a 12.5% 17-well SuperSep™ Phos-tag™ Precast Gel (FUJIFILM) for electrophoresis at 100 V for 200 minutes.

After electrophoresis, the Phos-tag™ Precast Gels were washed four times in a washing buffer containing 25 mM Tris, 192 mM Glycine, 20% (w/v) methanol, and 10 mM EDTA for 10 minutes each time, and then washed three times with the transfer buffer without EDTA (containing 25 mM Tris, 192 mM Glycine, 20% (w/v) methanol) for 10 minutes each time. Following the washing steps, proteins were transferred to Immobilon-P PVDF membranes (Millipore) using a semidry blotting system (Bio-Rad) at 15V for 46 minutes. Membranes were blocked with 5% (w/v) Non-fat Dry Milk (LabScientific) in TBST buffer which contained 0.1% (v/v) Tween 20 (Bio-Rad) at room temperature for 1 hour. Blocked membranes were then washed with TBST and incubated with the primary antibody (anti-EPYC1, obtained from YenZym) with 1:5000 dilution in TBST containing 2.5% milk at room temperature for 1 hour or at 4°C overnight. Membranes were washed in TBST four times before incubation with the secondary antibody, goat anti-rabbit IgG

bioRxiv preprint doi: https://doi.org/10.1101/2025.10.09.681382; this version posted October 10, 2025. The copyright holder for this preprint (which was not certified by peer review) is the author/funder, who has granted bioRxiv a license to display the preprint in perpetuity. It is made available under a CC-BY 4.0 International license.

(H+L) (Thermo Fisher Scientific), with 1:10,000 dilution at room temperature for 1 hour. Immunoreactive proteins were detected using enhanced chemiluminescence (WesternBright ECL, Advansta) followed by X-ray film processing (CL-XPosure Film, Thermo Fisher Scientific; SRX-101A, Konica- Minolta) or imaged by an iBright FL1500 Imaging System (Thermo Fisher Scientific).

For Fig. 4g, cell fractionation and immunoblotting was performed as described in Hennacy et al., 2024[75]. In brief, wild-type Chlamydomonas was grown in TAP media at air levels of CO_2 until it reached 2 $\times 10^6$ cells/mL density. Cells were spun down for 5 minutes at 1000 × g and the pellet was weighed and resuspended in 2 × volumes of lysis buffer (50 mM HEPES, 10 mM KOAc, 2 mM $Mg(OAC)_2$, 1 mM $CaCl_2$, pH 7.0 + protease inhibitors). Cells were sonicated on ice for 5 minutes, 3 seconds pulse, 60% amplitude. Lysates were spun for 10 minutes at 2000 × g to remove any unlysed cells. 50 µL of supernatant was collected as whole cell lysate. The remaining lysate was spun for 30 minutes at 18,000 × g. The supernatant was collected and the pellet was washed in 5× volumes of lysis buffer, re-spun, and resuspended. Laemmeli sample buffer was added to samples followed by boiling at 95˚C for 10 minutes. Each sample was split in two, with half being separated on an SDS-polyacrylamide gel (Bio-rad) while the other half was separated on a Phos-tag™ Precast Gel. Gel was transferred to a PVDF membrane using a semi-dry transfer system (Bio-rad). Primary antibody was added overnight at 4˚C, followed by three 10-minute washes in 1×TBS-0.1% tween. The secondary antibody was added for 1 hour at room temperature, followed by three additional washes in TBS-T. Blots were imaged on an iBright imaging system using enhanced chemiluminescence.

Protein expression and purification

The KEY1 and KEY1$^{\Delta RBM}$ protein were expressed and purified by ProteoGenix. For the expression with *E.coli* expression system, the cDNA coding for the 6 x His tagged KEY1 (6His-KEY1-EC) was chemically synthesized with optimization for expression in *E.coli*. After the starter growth of the cells at 37 °C, the protein expression was induced with 1 mM IPTG at 16˚C for 16 hrs. The expressed 6 × His tagged KEY1 was purified on Nickel resin, with equilibration and binding with PBS buffer (pH7.5) and washes and elution by imidazole shift. The final sample was buffer exchanged with 20 mM Tris, 50 mM NaCl, pH 8. For the expression with the baculovirus/insect cells expression system, the gene coding for the 6 × His tagged KEY1 (6His-KEY1-IC) was chemically synthesized with optimization for expression in insect cells and then was subcloned in ProteoGenix' proprietary expression vector for insect cells. The expression construct obtained was used to transform *E. coli* strain DH10Bac to produce recombinant Bacmids. Purified recombinant Bacmids were then prepared by a standard method, and transfected in *Spodoptera frugiperda* (Sf) cells to generate the P1 virus stock. Sf cells were infected with different quantities of P2 stock, and the best expression level was observed in Sf9 cells with infection during 72 hrs with 30 µl of virus. Cell lysis was obtained by sonication in PBS buffer (pH 7.5), and the 6 × His tagged KEY1 was purified with an affinity vs. His-Tag purification using a standard protocol, which is an equilibration with PBS (pH 7.5) followed by 3 × washes with PBS (pH 7.5) and 0 mM, 30 mM, 50 mM imidazole buffer, and then an elution with PBS, pH 7.5, 200 mM and 400 mM imidazole buffer. Elutions were pooled and the final sample was buffer exchanged vs 20 mM Tris,

bioRxiv preprint doi: https://doi.org/10.1101/2025.10.09.681382; this version posted October 10, 2025. The copyright holder for this preprint (which was not certified by peer review) is the author/funder, who has granted bioRxiv a license to display the preprint in perpetuity. It is made available under a CC-BY 4.0 International license.

50 mM NaCl, pH 8 by dialysis method and concentrated. Both the *E. coli* and insect cell-purified proteins were stored in 50% glycerol and flash frozen in liquid nitrogen for shipment and long term storage at -80 °C. The proteins used in experiments were subjected to an additional flash-freeze-thaw cycle after aliquoting.

EPYC1-GFP and EPYC1 (both with His tag) were expressed and purified as described in He et al 2023[83] and Wunder et al 2018[58]. Briefly, the pHueEPYC1-GFP plasmid was transformed into BL21 DE3 *E. coli* cells. Cells were grown from frozen glycerol stocks in LB with carbenicillin at 37˚C overnight. 1.2 mL of starter culture were added to 250 mL media in 1 L flasks and grown at 37˚C until OD 0.6. At OD 0.6, the flasks were placed on ice to cool for 30 minutes. Then 0.4 mM IPTG was added and the cultures were grown overnight at 18˚C to induce expression and reduce toxicity. Cells were harvested by centrifugation at 5000 × g for 30 minutes. The pellet was resuspended in 50 mL of media, transferred to a 50 mL falcon tube and centrifuged for 10 minutes at 3200 × g. The pellet was then frozen at -80°C for future use. On the day of purification, the cell pellet was thawed and resuspend in high-salt lysis buffer (20 mM Tris-HCl, 500 mM NaCl, 10 mM Imidazole, 0.3 mg/mL lysozyme, 3 mM phenylmethylsulfonyl fluoride, 50 units of Benzonase (Sigma-Aldrich), 2 mM $MgCl_2$) so that the total volume was 25 mL. The cells were lysed on ice by sonication using a tip sonicator (Q125 + CL-18 probe, QSonica) for 6 cycles of 10 seconds with 50 seconds rest at 50% amplitude, or with additional cycles until visually lysed. The lysate was clarified by centrifugation at 100,000 × g in SW 41 rotor (Beckman Coulter) for 30 minutes. The supernatant was then filtered through a 0.2 µm filter before loading onto a HisTrap HP column using an AKTA protein purification system (Cytivia). The column was eluted into high imidazole buffer (20 mM Tris-HCl pH 8.0, 500 mM NaCl, 300 mM Imidazole) using a 0% to 100% gradient over 5 minutes at a flow rate of 1 mL/minute. Fractions that had a peak in absorbance 280 nm were pooled together. These fractions were loaded onto a size exclusion column (Superdex Increase 200 10/300 GL, Cytivia) equilibrated in storage buffer (20 mM Tris-HCl, 50 mM NaCl, pH 8.0, 5% glycerol). Fractions that came off the column at the correct molecular weight peak were pooled, and the concentration was measured using Qubit Fluorometric Quantitation (Thermo Fisher). We also measured the 260/280 nm absorbance using a nanodrop to ensure that DNA contamination was minimal. For the proteins used in the phase diagram (Fig. 4c,d), the A260/280 was 0.3. The protein was then aliquoted, flash-frozen in liquid nitrogen, and stored at -80°C for future use.

Rubisco was extracted and purified as described in He et al., 2020 and Meyer et al., 2020 with adaptations[59, 85]. Specifically, cells were collected by centrifugation at 4,000 rpm for 15 minutes in an Avanti J-26X centrifuge with an 8.1000 rotor (Beckman) at 4°C. The pellets were washed in pre-chilled TAP medium and then resuspended in a 1:1 (v/w) ratio of cold extraction buffer (10 mM $MgCl_2$, 50 mM Bicine, 10 mM $NaHCO_3$, 1 mM dithiothreitol, pH 8.0) supplemented with Halt Protease Inhibitor Cocktail, EDTA-Free (Thermo Fisher Scientific). Cell slurry was immediately added to liquid nitrogen to form small popcorn pellets which were stored at -80°C until needed. Cells were lysed by cryogenic grinding using a Cryomill (Retsch) at a frequency of 25 oscillations/second for 20 minutes. The ground powder was defrosted on ice for 60-120 minutes. The soluble proteins were isolated by centrifugation (16,000 × g, 30 minutes, 4°C), and 600 mL of the clarified lysate was loaded on top of a thin-wall ultracentrifugation tube (Ultra-Clear,

bioRxiv preprint doi: https://doi.org/10.1101/2025.10.09.681382; this version posted October 10, 2025. The copyright holder for this preprint (which was not certified by peer review) is the author/funder, who has granted bioRxiv a license to display the preprint in perpetuity. It is made available under a CC-BY 4.0 International license.

Beckman Coulter) containing 12 mL of a 10 to 30% sucrose gradient prepared with the extraction buffer. Gradients were made the previous day with a gradient maker (BioComp Instruments) and left to equilibrate at 4°C. After an ultracentrifugation in a SW 41 Ti rotor (Beckman Coulter) at a speed of 35,000 rpm for 20 hours at 4 °C, fractions (750 mL each) were collected with a piston gradient fractionator (BioComp Instruments). Rubisco-containing fractions were applied to an anion exchange column (MONO Q™ 5/50 GL, Cytiva) and eluted with a linear salt gradient from 30 to 500 mM NaCl in a buffer with 20 mM Tris-HCl, pH 8, and 2.5 mM DTT. Fractions enriched in Rubisco were confirmed by SDS-PAGE, and were pooled before being concentrated and buffer exchange into phase separation buffer (20 mM Tris HCl pH 8.0, 50 mM NaCl) with centrifugal filters (Amicon 100K, MilliporeSigma).

Identification of EPYC1 phosphorylation sites regulated by KEY1

EPYC1-Venus-3×FLAG and *key1-1*;EPYC1-Venus-3×FLAG cells were prepared for immunoprecipitation as described in Wang et al., 2023 with the following modifications[94]. Halt protease and Halt phosphatase inhibitors (Thermo Fisher Scientific) were added at 1× to the lysis buffer and elution buffers. No digitonin was added to the wash or elution buffers. An additional high salt wash was added, with 0.5 M NaCl in wash buffer to remove Rubisco and other protein interactors. After elution, samples were divided into 50 µL aliquots and immediately flash-frozen.

EPYC1-GFP and KEY1 were purified from *E. coli* as described above. Samples were prepared in 20 mM Tris-HCl, pH 8, supplemented with 5 mM $MgCl_2$ and 5 mM $MnCl_2$, which are necessary for kinase and phosphatase activity, respectively. Each sample had a final volume of 50 µL. *E. coli*-purified EPYC1-GFP was added for a final concentration 17.5 µM. For the Lambda phosphatase-treated sample, 1 µL of Lambda Protein Phosphatase (400,000 units/µL, NEB) was added. For KEY1-treated samples, *E. coli* -purified KEY1 was added at 115 nM, 690 nM, 1.4 nM and 3 µM final concentration along with 1 mM ATP. All samples were incubated at room temperature for 30 minutes. Then 2 µL of Halt protease and 2 µL of Halt phosphatase inhibitors (Thermo Fisher Scientific) were added. 2 µL of each sample was reserved for Phos-tag gel analysis. The remaining 48 µL was immediately processed for mass spectrometry analysis.

For the *Chlamydomonas*-purified EPYC1, in-gel digestion of protein bands using trypsin was performed as in Shevchenko et al[99]. For the *E. coli* purified EPYC1, the liquid samples were subjected to in-solution thiol reduction/alkylation and trypsin Gold (Promega) digestion overnight according to the manufacturer's instructions. Trypsin-digested samples were dried completely in a SpeedVac and resuspended with 20 µL of 0.1% formic acid pH 3 in water. 2 µL (~ 360 ng) was injected per run using an Easy-nLC 1200 UPLC system. Samples were loaded directly onto a 45 cm long 75 µm inner diameter nano capillary column packed with 1.9 µm C18-AQ resin (Dr. Maisch, Germany) mated to metal emitter in-line with an Orbitrap Fusion Lumos (Thermo Scientific, USA). Column temperature was set at 45 °C and two-hour gradient method with 300 nL/minute flow was used. The mass spectrometer was operated in data dependent mode with the 120,000 resolution MS1 scan (positive mode, profile data type, AGC gain of 4e5, maximum injection time of 54 sec and mass range of 375-1500 m/z) in the Orbitrap followed by HCD fragmentation in Orbitrap (30,000 resolution) with 35% collision energy. Dynamic exclusion list

bioRxiv preprint doi: https://doi.org/10.1101/2025.10.09.681382; this version posted October 10, 2025. The copyright holder for this preprint (which was not certified by peer review) is the author/funder, who has granted bioRxiv a license to display the preprint in perpetuity. It is made available under a CC-BY 4.0 International license.

was invoked to exclude previously sequenced peptides for 60 seconds and maximum cycle time of 3 seconds was used. Peptides were isolated for fragmentation using quadrupole (1.2 m/z isolation window).

Raw files were searched using MSAmanda 2.0[100] and Sequest HT algorithms[101] within the Proteome Discoverer 2.5.0 suite (Thermo Scientific, USA). 10 ppm MS1 and 0.4 Da MS2 mass tolerances were specified. Carbamidomethylation of cysteine was used as fixed modification, oxidation of methionine, phosphorylation of serine, threonine, and tyrosine were specified as dynamic modifications. Pyro glutamate conversion from glutamic acid and glutamine are set as dynamic modifications at peptide N-terminus. Acetylation was specified as dynamic modification at protein N-terminus. Trypsin digestion with maximum of 2 missed cleavages were allowed. Files were searched against UP000006906 Chlamydomonas database downloaded from Uniprot.org.

Scaffold (version Scaffold 5.1.0, Proteome Software Inc., Portland, OR) was used to validate MS/MS based peptide identifications. Peptide identifications were accepted if they could be established at greater than 95.0% probability by the Scaffold Local FDR algorithm. The data and subsequent analysis are often unable to distinguish the phosphorylation pattern on the polyS sequences in EPYC1: a shift of 80 Da was observed in the fragmentation, indicating the addition of a phosphate group, but which serine it fell on remained ambiguous. In these cases, the Scaffold analysis software assigns the phosphorylation site to the first serine in the sequence. In some cases, a phosphorylation site was unambiguously identified as the second or third serine in the sequence.

In vitro phase separation experiments

EPYC1-GFP and KEY1 were purified from *E. coli* as described above. Rubisco was purified from Chlamydomonas as described above. 10 μM EPYC1-GFP was mixed with 0 μM or 3 μM KEY1 and 0.8 mM ATP in protein kinase buffer (20 mM Tris HCl pH 8.0, 5 mM MgCl2, 5 mM MnCl2, 1mM DTT) and incubated at room temperature for 30 minutes to produce unphosphorylated and phosphorylated EPYC1-GFP, respectively.

We used microscopy to determine the phase diagram. A glass chamber with parafilm spacers between two #1.5 coverslips cleaned with Hellmanex soap was constructed[102]. We mapped the phase diagram by mixing stock Rubisco, EPYC1-GFP, and phase separation buffer at 0-2 μM Rubisco and 0-5 μM EPYC1-GFP in 3 μL total volume. Each sample was loaded immediately after mixing, and the lane was sealed using clear nail polish. After 5 minutes, the sample was assessed for droplets under the microscope. We used a Nikon Ti Eclipse widefield microscope with a EGFP filter cube (Excitation 40/35 nm, Dicrhoic mirror 505 nm, Emission 535/40 nm) to assess EPYC1-GFP signal. Phase separation was visually assessed by the presence of droplets in brightfield and GFP channels.

Fluorescence correlation spectroscopy to measure EPYC1-Rubisco interactions

bioRxiv preprint doi: https://doi.org/10.1101/2025.10.09.681382; this version posted October 10, 2025. The copyright holder for this preprint (which was not certified by peer review) is the author/funder, who has granted bioRxiv a license to display the preprint in perpetuity. It is made available under a CC-BY 4.0 International license.

Phosphorylated and unphosphorylated EPYC1-GFP were prepared as in the *in vitro* phase separation experiments. The phosphorylation status was confirmed through Phos-tag gel with Coomassie stain (Fig. 3c). 20 nM EPYC1-GFP was mixed with 2 μM Rubisco, a concentration at which phase separation was not observed. Fluorescent correlation spectroscopy was performed on the mixtures using a custom-built setup with a 488 nm excitation laser. Diffusion coefficients of EPYC1-GFP were extracted from fitting the fluorescence intensity correlation curves using a single-species analytical model. Details of the method and analysis are described in He et al., 2023[83].

Surface plasmon resonance experiments

All the surface preparation experiments were performed at 25 °C using a Biacore™ 8K+ SPR system (Cytiva Life Sciences). All the binding assays were performed using the Biacore PBS-P + Buffer (20 mM phosphate buffer, 2.7 mM KCl, 137 mM NaCl, and 0.05% Surfactant P20, pH 6.8) as a running buffer.

Purified Rubisco was immobilized on the experimental flow cell of each of the eight channels on a CM5 sensor chip using a Biacore Amine Coupling Kit (Cytiva Life Sciences) according to the manufacturer's instructions. Briefly, the chip surface was activated by an injection of 1:1 N-hydroxysuccinimide/1-ethyl-3-(3-dimethylaminopropyl)carbodiimide hydrochloride. Rubisco was diluted to ~50 μg ml^{-1} in 10 mM acetate (pH 4.5; this pH had been previously optimized using the immobilization pH scouting wizard) and was injected over the chip surface. Excess-free amine groups were then capped with an injection of 1 M ethanolamine. The immobilization levels were ~2,200 resonance units on all channels. The reference flow cell of each of the eight channels on this sensor chip was prepared in exactly the same manner as the experimental surfaces, except that no Rubisco was injected.

For the binding assay, the analyte, which is the RBM^{KEY1} peptide (LGFWRVDIEDQAAFI) synthesized by Genscript, was dissolved in the running buffer and diluted to 100 μM. The peptide was injected over the reference flow cell and experimental flow cell on each channel at a flow rate of 30 μl min^{-1} for 2 min, followed by 10 min of the running buffer alone to allow for dissociation. Analysis of the results was performed with the Biacore™ Evaluation Insight Software.

The signal of the change in refractive index at the sensor chip surface is recorded real-time in resonance units (RUs), which are proportional to the total mass and number of molecules bound to the surface. To measure binding between the peptide+buffer (or buffer alone) and the Rubisco bound to the surface, we subtracted the signal measured for binding between the peptide+buffer (or buffer alone) and the uncoated surface from the signal measured for binding of the peptide+buffer (or buffer alone) and the Rubisco bound to the surface. The single-subtracted binding signals of the peptide+buffer or buffer alone at the end of the injection time—when the binding signal had reached a steady-state phase—were plotted in Fig. 5d.

bioRxiv preprint doi: https://doi.org/10.1101/2025.10.09.681382; this version posted October 10, 2025. The copyright holder for this preprint (which was not certified by peer review) is the author/funder, who has granted bioRxiv a license to display the preprint in perpetuity. It is made available under a CC-BY 4.0 International license.

To account for the binding between the buffer and the Rubisco, we subtracted the single-subtracted buffer signals from the single-subtracted peptide+buffer signals to obtain the double-subtracted peptide binding to Rubisco signals shown in the Extended Data Fig. 7.

Mathematical model

To model the dynamics of the linker protein EPYC1 in the pyrenoid, we consider a continuum model in which the concentration of unphosphorylated (*sticky*) and phosphorylated (*non-sticky)* EPYC1 are denoted by $c_{\mathrm{s}}(\boldsymbol{r},t) = c_{\mathrm{max}}\phi_{\mathrm{s}}(\boldsymbol{r},t)$ and $c_{\mathrm{ns}}(\boldsymbol{r},t) = c_{\mathrm{max}}\phi_{\mathrm{ns}}(\boldsymbol{r},t)$, respectively, where $\boldsymbol{r}$ is position, t is time, c_{max} is the maximum possible molar concentration, and ϕ are the spatially-dependent volume fractions.

EPYC1 free energies and chemical potentials. We model EPYC1 and solvent interactions with the following Flory-Huggins free-energy density:

$$\frac{f}{k_{\mathrm{B}}T} = \sum_i \left(\phi_i \ln \phi_i + \sum_j \frac{\chi_{i\text{-}j}}{2}\phi_i\phi_j + \sum_j \frac{\kappa_{i\text{-}j}}{2}\boldsymbol{\nabla}\phi_i \cdot \boldsymbol{\nabla}\phi_j \right), \qquad (1)$$

where $i = \{\mathrm{s,ns,sol}\}$ denotes sticky EPYC1s, non-sticky EPYC1s, and solvent respectively, k_{B} is the Boltzmann constant, and T the absolute temperature. The first term in Equation 1 is the entropy of mixing, which tends to keep the system well mixed. The second term represents the interaction energy between the components of the mixture, where $\chi_{i\text{-}j}$ are Flory-Huggins interaction parameters. The third term reflects a surface energy that determine the width of the interface $\sqrt{\kappa_{i\text{-}j}}$ between phases. In Equation 1 we have assumed that the molecular volumes of EPYC1 and solvent molecules are the same, which is a reasonable approximation considering the crowded cytoplasm of the cell as solvent. In what follows, we also assume that non-sticky EPYC1s behave identically to solvent molecules, and therefore consider a single non-zero interaction parameter $\chi_{\mathrm{s\text{-}s}} \equiv \chi < 0$, stemming from the attractive interaction between the sticky unphosphorylated EPYC1s.

EPYC1 dynamics. To model the dynamics of EPYC1, we consider the following kinetic equations:

$$\partial_t \phi_i = \boldsymbol{\nabla} \cdot \left[\sum_j L_{i\text{-}j}\boldsymbol{\nabla}\left(\mu_j - \mu_{\mathrm{sol}}\right) \right] - J_{i\to j} + J_{j\to i}, \qquad (2)$$

where $i,j = \{\mathrm{s,ns}\}$. The first term describes diffusive fluxes driven by gradients of chemical potential μ_i, and $J_{i\to j}$ and $J_{j\to i}$ are the switching fluxes between sticky and non-sticky states. The total EPYC1 concentration is constant $c_{tot} = c_{max}(\phi_s + \phi_{ns})$. To derive Equation 2 we have assumed that the diffusive fluxes are linearly proportional to the gradients of the local chemical potentials μ, i.e., $\boldsymbol{j}_i = -\sum_j L_{i\text{-}j}\boldsymbol{\nabla}\mu_j$, where $L_{i\text{-}j}$ is a matrix of mobility coefficients that satisfies the Onsager reciprocal relations, $L_{i\text{-}j} = L_{j\text{-}i}$. Imposing an incompressibility condition $\sum_i \phi_i = 1$ implies $\sum_i \boldsymbol{j}_i = \boldsymbol{0}$ and thus $\sum_j L_{i\text{-}j} = 0$, which yields Equation 2. For simplicity, we assume that cross-terms are negligible, i.e., $L_{i\text{-}j} = 0$ for $i \neq j$ so that gradients of sticky enzyme chemical potential do not drive fluxes of non-sticky enzymes and vice versa, and $L_{i\text{-}i} = A_{i\text{-}i}\phi_i$. We further assume for

bioRxiv preprint doi: https://doi.org/10.1101/2025.10.09.681382; this version posted October 10, 2025. The copyright holder for this preprint (which was not certified by peer review) is the author/funder, who has granted bioRxiv a license to display the preprint in perpetuity. It is made available under a CC-BY 4.0 International license.

simplicity that the diffusivity of enzymes is independent of their configuration or density, i.e., $A_{\text{s-s}} = A_{\text{ns-ns}} = A \equiv D/(k_{\text{B}}T)$, where D is a constant diffusion coefficient.

The chemical potentials of sticky and non-sticky EPYC1 and solvent are obtained from the functional derivative of the free energy of the system with respect to each volume fraction. Thus, the chemical potential differences driving the diffusive fluxes read:

$$\frac{\mu_{\text{s}} - \mu_{\text{sol}}}{k_{\text{B}}T} = \ln\left(\frac{\phi_{\text{s}}}{1-\phi_{\text{s}}-\phi_{\text{ns}}}\right) + 2\chi\phi_{\text{s}} - \kappa'_{\text{s}}\boldsymbol{\nabla}^2\phi_{\text{s}} - \kappa'_{\text{s-ns}}\boldsymbol{\nabla}^2\phi_{\text{ns}}, \qquad (3)$$

$$\frac{\mu_{\text{ns}} - \mu_{\text{sol}}}{k_{\text{B}}T} = \ln\left(\frac{\phi_{\text{ns}}}{1-\phi_{\text{s}}-\phi_{\text{ns}}}\right) - \kappa'_{\text{s-ns}}\boldsymbol{\nabla}^2\phi_{\text{s}} - \kappa'_{\text{ns}}\boldsymbol{\nabla}^2\phi_{\text{ns}}, \qquad (4)$$

where $\kappa'_{\text{s}} = \kappa_{\text{s-s}} - 2\kappa_{\text{s-sol}} + \kappa_{\text{sol-sol}}$, $\kappa'_{\text{ns}} = \kappa_{\text{ns-ns}} - 2\kappa_{\text{ns-sol}} + \kappa_{\text{sol-sol}}$, and $\kappa'_{\text{s-ns}} = \kappa_{\text{s-ns}} - \kappa_{\text{s-sol}} - \kappa_{\text{ns-sol}} + \kappa_{\text{sol-sol}}$.

Switching rates. For simplicity, we assume that the kinase KEY1 is uniformly distributed throughout the pyrenoid and so we take the switching rates between sticky and non-sticky EPYC1 to be spatially uniform, and thus the switching fluxes are proportional to the volume fractions of EPYC1:

$$J_{i\to j} = k_{i\to j}\phi_i, \qquad (5)$$

where $k_{i\to j}$ are constant switching rates.

Boundary conditions. We impose periodic boundary conditions for the simulations in the square geometry, and no-flux boundary conditions in the geometry mimicking the cell's shape, i.e., $\boldsymbol{j}_{\text{s}} \cdot \boldsymbol{n} = 0$ and $\boldsymbol{j}_{\text{ns}} \cdot \boldsymbol{n} = 0$. Furthermore, in the latter geometry, to avoid wetting of condensates on the boundaries, we impose the following boundary conditions[103, 104]:

$$\boldsymbol{\nabla}\phi_{\text{s}} \cdot \boldsymbol{n} = \frac{\sqrt{2}}{2\kappa'_{\text{s}}}\cos(\theta_{\text{s}})\,(1-\phi_{\text{s}}^2), \qquad (6)$$

$$\boldsymbol{\nabla}\phi_{\text{ns}} \cdot \boldsymbol{n} = \frac{\sqrt{2}}{2\kappa'_{\text{ns}}}\cos(\theta_{\text{ns}})\,(1-\phi_{\text{ns}}^2), \qquad (7)$$

where θ_i is the contact angle of the condensate at the boundary. To prevent wetting, we impose a large angle, $\theta_i = 5\pi/6$.

Non-dimensionalization. We reduce the number of parameters of our model by non-dimensionalizing it. To this end, we choose $\sqrt{\kappa'_{\text{s-ns}}}$ as characteristic length scale, and $k^{-1}_{\text{ns}\to\text{s}}$ as characteristic time scale. The resulting dimensionless parameters are:

$$\widetilde{D} \equiv \frac{D}{\kappa'_{\text{s-ns}}k_{\text{ns}\to\text{s}}} = \frac{\text{EPYC1 diffusion rate}}{\text{EPYC1 switching rate}}, \qquad (8)$$

$$\tilde{k} \equiv \frac{k_{\text{s}\to\text{ns}}}{k_{\text{ns}\to\text{s}}} = \frac{\text{s}\to\text{ns switching rate}}{\text{ns}\to\text{s switching rate}}. \qquad (9)$$

Upon this choice of scales, the uniform solution of Equations 2-5 is $\phi_{\text{s},0} = \phi_{\text{tot}}/(1+\tilde{k})$, and $\phi_{\text{ns},0} = \phi_{\text{tot}}\tilde{k}/(1+\tilde{k})$, where ϕ_{tot} is the total EPYC1 volume fraction. The other governing dimensionless parameters are ϕ_{tot}, the EPYC1-EPYC1 attractive interaction strength χ, the ratio between interfacial parameters $\tilde{\kappa}_{\text{s}} = \kappa'_{\text{s}}/\kappa'_{\text{s-ns}}$ and $\tilde{\kappa}_{\text{ns}} = \kappa'_{\text{ns}}/\kappa'_{\text{s-ns}}$, and the dimensionless size of the system $\tilde{L} \equiv L/\sqrt{\kappa'_{\text{s-ns}}}$.

Linear stability analysis. To determine when EPYC1 will form clusters and whether coarsening of EPYC1 clusters will continue indefinitely or be arrested, we perform a linear stability analysis.

bioRxiv preprint doi: https://doi.org/10.1101/2025.10.09.681382; this version posted October 10, 2025. The copyright holder for this preprint (which was not certified by peer review) is the author/funder, who has granted bioRxiv a license to display the preprint in perpetuity. It is made available under a CC-BY 4.0 International license.

Specifically, starting from the uniform solution, the dynamical equations obtained above are linearized by introducing small-amplitude perturbations, which are decomposed into normal modes to obtain the relation between the growth rate $\tilde{\omega}$ and wavenumber $\tilde{q}$ of the perturbations, $L(\tilde{\omega}, \tilde{q}) = 0$, where tildes denote dimensionless quantities:

$$\frac{\tilde{\omega}(\tilde{\omega}+1+\tilde{k})}{\tilde{q}^4\tilde{D}} - \tilde{q}^2\tilde{D}\frac{\phi_{ns,0}[\tilde{\kappa}_{ns}(1-\phi_{ns,0})-\phi_{s,0}]+\phi_{s,0}[\tilde{\kappa}_s(1-\phi_{s,0})-\phi_{ns,0}]+2\chi\phi_{s,0}\phi_{ns,0}\tilde{\kappa}_{ns}(\phi_{tot}-1)}{\phi_{tot}-1} -$$

$$\frac{\tilde{\omega}[2-\phi_{tot}+2\chi\phi_{s,0}(\phi_{tot}-1)]+1+\tilde{k}+2\chi\phi_{s,0}(\phi_{tot}-1)}{\tilde{q}^2(\phi_{tot}-1)} + \phi_{ns,0}[1+\tilde{\kappa}_{ns}(\tilde{\omega}+\tilde{k})] + \phi_{s,0}[\tilde{k}+\tilde{\kappa}_s(\tilde{\omega}+1)] -$$

$$\frac{\tilde{D}[1+2\chi\phi_{s,0}(\phi_{s,0}-1)]}{\phi_{tot}-1} + \tilde{q}^4\tilde{D}\phi_{s,0}\phi_{ns,0}(\tilde{\kappa}_s\tilde{\kappa}_{ns}-1) = 0. \qquad (10)$$

By solving Equation 10, we can obtain the most unstable perturbation with maximum growth rate $\tilde{\omega}_{max}$, and corresponding wavenumber $\tilde{q}_{max} = 2\pi/\tilde{\lambda}_{max}$, where $\tilde{\lambda}_{max}$ is the most-unstable wavelength of perturbations. To infer whether the system exhibits continued or arrested coarsening for a given set of parameter values ($\phi_{tot}, \tilde{\kappa}_s, \tilde{\kappa}_{ns}, \chi, \tilde{D}, \tilde{k}$), we analyze the amplification curve $\tilde{\omega}(\tilde{q})$. Specifically, when small-wavenumber modes are suppressed (i.e., $\tilde{\omega} < 0$), coarsening might be arrested in the nonlinear regime. In the limit $\tilde{q} \to 0$, Equation (10) yields $\tilde{\omega} \to 0$ and $\mathrm{d}\tilde{\omega}/\mathrm{d}\tilde{q} \to 0$. Therefore, to determine the parameter values under which coarsening might be arrested, we identify cases where $\tilde{\omega}(\tilde{q})$ is negatively convex, i.e., $d^2\tilde{\omega}/\mathrm{d}\tilde{q}^2 < 0$ at $\tilde{q} = 0$, while the system still exhibits at least one unstable mode, $\tilde{\omega}_{max} > 0$, which implies phase separation at a finite wavelength.

Model parameter values. In all simulations shown in Fig. 6a-f of the Main Text, we use $\tilde{D} = 10$, $\phi_{tot} = 0.1$, $\tilde{\kappa}_s = 5$, $\tilde{\kappa}_{ns} = 1$, and $\chi = 7$. The dimensionless minor and major semiaxes of the ellipse corresponding to the outer boundary are 29.17 and 35, respectively, and the radius of the inner circle is 16.67. These dimensionless parameter values correspond to: $D = 60\ \mu m^2 s^{-1}$, $k_{ns\to s} \simeq 294\ s^{-1}$, $\kappa'_{s\text{-}ns} \simeq 0.02\ \mu m^2$, and a major semiaxes of the ellipse of $5\ \mu m$. Additionally, $\tilde{k} = 0.14$ in Fig. 6d and f, and $\tilde{k} = 0.01$ in Fig. 6e. In Fig. 6g, we use $\tilde{k} = 10^{-3}$ and $\chi = 5.5$ to model low KEY1 activity and EPYC1 normally sticky (top snapshot), and $\tilde{k} = 0$ and $\chi = 8$ to model no KEY1 activity and EPYC1 overly sticky.

Simplified droplet model. To better understand the selection of finite-size clusters when EPYC1 switches between the sticky and non-sticky state, we simplify our model. First, we assume that the system is a two-component system composed of unphosphorylated, sticky EPYC1, with volume fraction ϕ, and a bath of solvent plus phosphorylated EPYC1, with total volume fraction $1-\phi$ due to incompressibility. Neglecting terms related to interfacial tension, the conservation equation of sticky EPYC1 reads:

$$\partial_t\phi = D\boldsymbol{\nabla}\cdot\left(\boldsymbol{\nabla}\phi + \frac{\phi}{1-\phi}\boldsymbol{\nabla}\phi + 2\chi\phi\boldsymbol{\nabla}\phi\right) - k_{s\to ns}\phi + k_{ns\to s}(1-\phi). \qquad (11)$$

We consider the case where a dense condensate, primarily composed of sticky EPYC1, forms with an equilibrium concentration ϕ_+ within the condensate, and a dilute bath with an equilibrium concentration $\phi_- < \phi_+$. We linearize Eq. (11) inside and outside the condensate around these equilibrium concentrations. For simplicity, we assume that the effective diffusivities of sticky EPYC1 are identical both inside and outside the condensate. Furthermore, we assume the cluster is in a quasi-steady state, meaning its growth or shrinkage occurs much more slowly than the time

bioRxiv preprint doi: https://doi.org/10.1101/2025.10.09.681382; this version posted October 10, 2025. The copyright holder for this preprint (which was not certified by peer review) is the author/funder, who has granted bioRxiv a license to display the preprint in perpetuity. It is made available under a CC-BY 4.0 International license.

it takes for EPYC1 to diffuse or switch between states. These assumptions lead to the following simplified equation:

$$0 = \boldsymbol{\nabla}^2\phi_i - \phi_i + \tilde{k}(1-\phi_i) \qquad (12),$$

where $i = (\mathrm{in}, \mathrm{out})$, and $\tilde{k} = k_{\mathrm{ns}\to\mathrm{s}}/k_{\mathrm{s}\to\mathrm{ns}}$. We have non-dimensionalized Eq. (12) by choosing $\ell = \sqrt{D/k_{\mathrm{s}\to\mathrm{ns}}}$ as characteristic length scale, which stems from a balance between EPYC1 diffusion and the sticky to non-sticky switching rate. We solve Eq. (12) considering a spherically symmetric cluster of dimensionless radius $\tilde{R} = R/\ell$:

$$\phi_{\mathrm{in}}(r) = \frac{\tilde{k}}{1+\tilde{k}} + \frac{\tilde{R}\left[\tilde{k}(\phi_+ - 1) + \phi_+\right]\operatorname{csch}\left(\sqrt{1+\tilde{k}}\,\tilde{R}\right)\sinh\left(\sqrt{1+\tilde{k}}\,\tilde{r}\right)}{\left(1+\tilde{k}\right)\tilde{r}}, \qquad (13)$$

$$\phi_{\mathrm{out}}(r) = \frac{\tilde{k}}{1+\tilde{k}} + \frac{\tilde{R}\left[\tilde{k}(\phi_- - 1) + \phi_-\right]\exp\left[\sqrt{1+\tilde{k}}\,(\tilde{R}-\tilde{r})\right]}{\left(1+\tilde{k}\right)\tilde{r}}, \qquad (14)$$

where we have imposed regularity of the solution at $\tilde{r} = 0$, zero EPYC1 flux far from the cluster at $\tilde{r} \to \infty$, and fixed equilibrium concentrations, $\phi_{\mathrm{in}} = \phi_+$ and $\phi_{\mathrm{out}} = \phi_-$, at the cluster interface $\tilde{r} = \tilde{R}$, disregarding any contribution from Laplace pressure. The evolution of the cluster is determined by the following kinematic equation:

$$\frac{d\tilde{R}}{d\tilde{t}} = \boldsymbol{n}\cdot\frac{\tilde{\boldsymbol{j}}_{\mathrm{in}} - \tilde{\boldsymbol{j}}_{\mathrm{out}}}{\phi_{\mathrm{in}} - \phi_{\mathrm{out}}} = \frac{1}{\tilde{R}} - \frac{\tilde{k}(\phi_- - 1) + \phi_- + \left[\tilde{k}(\phi_+ - 1) + \phi_+\right]\coth(\sqrt{1+\tilde{k}}\tilde{R})}{\sqrt{1+\tilde{k}}(\phi_+ - \phi_-)}, \qquad (15)$$

where we have chosen $t_{\mathrm{c}} = \ell^2/D$ as characteristic time scale, and $\tilde{\boldsymbol{j}}_i = -\boldsymbol{\nabla}\phi_i$ are dimensionless diffusive fluxes, where $\tilde{\boldsymbol{j}}_{\mathrm{in}}$ is the flux density just inside the surface of the cluster and $\tilde{\boldsymbol{j}}_{\mathrm{out}}$ is the flux density just outside the surface of the cluster. In the absence of activity, i.e. without switching rates, $\tilde{\boldsymbol{j}}_{\mathrm{in}} = \boldsymbol{0}$ and $\tilde{\boldsymbol{j}}_{\mathrm{out}} = -4\pi(\phi_\infty - \phi_-)\tilde{R}$, implying that the condensate grows unboundedly in a diffusive manner by adsorbing material. This leads to the following growth law: $\tilde{R} = \tilde{R}_{\mathrm{init}} + \sqrt{2(\phi_\infty - \phi_-)/(\phi_+ - \phi_-)t}$, where ϕ_∞ is the far-field volume fraction of sticky EPYC1. When reactions are turned on, there is a critical ratio of switching rates $\tilde{k}_{\mathrm{c}} = f(\phi_+, \phi_-)$, below which Eq. (15) has a stable fixed point (i.e., $\mathrm{d}\tilde{R}/\mathrm{d}\tilde{t} = 0$), implying an equilibrium radius $\tilde{R}_{\mathrm{eq}}$. Above this critical point, no stable fixed points exist, and the cluster grows unboundedly. Close to the transition region, $\tilde{R} \gg 1$. Thus, taking this limit in Eq. (15) and solving $\mathrm{d}\tilde{R}/\mathrm{d}\tilde{t} = 0$ for $\tilde{k}$ yields the critical ratio of switching rates, $\tilde{k}_{\mathrm{c}} \simeq \frac{\phi_+ + \phi_-}{2 - \phi_+ - \phi_-}$, in excellent agreement with numerical solution of Eq. (15).

Below the critical switching ratio, $\tilde{k} < \tilde{k}_{\mathrm{c}}$, EPYC1 diffusion and reactions result in the internal and external fluxes of sticky EPYC1 across the condensate surface scaling differently with cluster radius: $\tilde{\boldsymbol{j}}_{\mathrm{in}} \sim \frac{4\pi\tilde{R}^3[\tilde{k}(1-\phi_+) - \phi_+]}{3}$ and $\tilde{\boldsymbol{j}}_{\mathrm{out}} \sim \frac{4\pi\tilde{R}^2[\tilde{k}(\phi_- - 1) + \phi_-]}{\sqrt{1+\tilde{k}}}\left(1 + \frac{1}{\sqrt{1+\tilde{k}}\,\tilde{R}}\right)$, leading to a stable cluster size, where we have expanded $\tilde{\boldsymbol{j}}_{\mathrm{in}}$ and $\tilde{\boldsymbol{j}}_{\mathrm{out}}$ in powers of $\tilde{R}$. Above the critical switching ratio, $\tilde{k} > \tilde{k}_{\mathrm{c}}$, most EPYC1 are sticky, and the external diffusive flux, scaling as $\sim 4\pi\tilde{R}^2$, dominates, causing the condensate to grow unboundedly. In the former case, well below the critical switching ratio, equating $\tilde{\boldsymbol{j}}_{\mathrm{in}} = \tilde{\boldsymbol{j}}_{\mathrm{out}}$ (which implies $\mathrm{d}\tilde{R}/\mathrm{d}\tilde{t} = 0$), yields a reasonable approximation for the

bioRxiv preprint doi: https://doi.org/10.1101/2025.10.09.681382; this version posted October 10, 2025. The copyright holder for this preprint (which was not certified by peer review) is the author/funder, who has granted bioRxiv a license to display the preprint in perpetuity. It is made available under a CC-BY 4.0 International license.

equilibrium radius $\tilde{R}_{\mathrm{eq}}$. In particular, in the limit $\phi_+ \gg \phi_-$, the equilibrium radius $R_{\mathrm{eq}} \simeq \sqrt{\frac{D}{k_{\mathrm{s}\to\mathrm{ns}}}}\frac{3\tilde{k}+\sqrt{3\tilde{k}(4+3\tilde{k})}}{2\sqrt{1+\tilde{k}}}$.

Data Availability

Data is available upon request from M.C.J.

Code Availability

Code is available on GitHub (https://github.com/linnealemma/KEY1_He-Lemma-etal and https://github.com/amcalv/2025-Simulations-Kinase-KEY1-paper).

bioRxiv preprint doi: https://doi.org/10.1101/2025.10.09.681382; this version posted October 10, 2025. The copyright holder for this preprint (which was not certified by peer review) is the author/funder, who has granted bioRxiv a license to display the preprint in perpetuity. It is made available under a CC-BY 4.0 International license.

Supplementary Tables

Supplementary Table 1. Immunoprecipitation-mass spectrometry (IP-MS) dataset, related to Fig 1. The full dataset was used to generate Fig. 1b, c. EPYC1-Venus-3×FLAG or KEY1-Venus-3×FLAG were used as baits, and Venus-3×FLAG was used as a control bait to test for non-specific interactions. Attached as Excel.

Supplementary Table 2. Oligonucleotides used in this work, Related to Methods.

Primer name	Sequence
CIB_3'_F	GACGTTACAGCACACCCTTG
CIB_5'_R	GCACCAATCATGTCAAGCCT
3673_F	GTGGTACTTGATGGTCAGCC
3676_F	GTACTTGATGGTCAGCCGG
3785_R	CGCAGAACCCGAAGTCAG
3809_R	CCCAAGCCCCCAAAATACC
949_CLiP_F	TGCTACGACCCCAGCTACTT
949_CLiP_R	CCAGATCCACCACTTCACCT
4859-5018_F	ACCGAGCCTCCACCCCTAAC
4859-5018_R	TAGGGCAGCCCCAGCATCAC
KEY1_473-491_adapter_F	GCTACTCACAACAAGCCCAGTTATGCGGCAAGCCACTCTTG
KEY1_5967-5984_adapter_R	GAGCCACCCAGATCTCCGTTCTTGGGCGAGCGGTAGCG
KEY1_US-2141_BstBI_F	GAGCAGGCGGCCTGGCTGTTCTACACACTTCCACACCACCAACC
KEY1_584_AgeI_R	GCGAGCGGATTTGACCGG
Key1_P1Fw	ACCGGGCAGGTGCTGTTC
Key1_p1Rv	CGTCGCGCTCGTACACTCG
CBLP FW	CAAGATCTGGGACCTGGAGAGC
CBLP RV	CTGGGCATTTACAGGGAGTGG

Supplementary Table 3. Plasmids used for transformation into Chlamydomonas and their resources, see also Methods.

Plasmid name	Gene	Promoter	Tags	Antibiotic Resistance in *E.coli*	Antibiotic Resistance in *Chlamydomonas*	Source
pLM005-EPYC1	*EPYC1* (genomic DNA)	*psad*	Venus-3xFLAG	Ampicillin	Paromomycin	Mackinder et al., 2016
pRAM118-pro+KEY1	*KEY1* (genomic DNA)	*KEY1* (2kb upstream of ATG)	Venus-3xFLAG	Ampicillin	Hygromycin	This paper; submitted to Chlamydomonas Resource Center
pRAM118-pro+KEY1-SNAP	*KEY1* (genomic DNA)	*KEY1* (2kb upstream of ATG)	SNAP-3xFLAG	Ampicillin	Hygromycin	This paper; submitted to Chlamydomonas Resource Center

bioRxiv preprint doi: https://doi.org/10.1101/2025.10.09.681382; this version posted October 10, 2025. The copyright holder for this preprint (which was not certified by peer review) is the author/funder, who has granted bioRxiv a license to display the preprint in perpetuity. It is made available under a CC-BY 4.0 International license.

pRAM118-pro+KEY1_ΔRBM-SNAP	*KEY1* (genomic DNA with mutated Rubisco-binding motif encoded sequence)	*KEY1* (2kb upstream of ATG)	SNAP-3xFLAG	Ampicillin	Hygromycin	This paper; submitted to Chlamydomonas Resource Center
pRAM118-proEPYC1-EPYC1-Venus	*EPYC1* (genomic DNA)	*EPYC1* (2kb upstream of ATG)	Venus-3xFLAG	Ampicillin	Hygromycin	This paper; submitted to Chlamydomonas Resource Center
pRAM118-proEPYC1-EPYC1-Astring-Venus	*EPYC1* (genomic DNA with all the Serine or Threonine encoding sequences changed to Alanine encoded sequences)	*EPYC1* (2kb upstream of ATG)	Venus-3xFLAG	Ampicillin	Hygromycin	This paper; submitted to Chlamydomonas Resource Center

Supplementary Table 4. Chlamydomonas strains used in this study and their resources, see also Methods.

Chlamydomonas Resource Center ID	Strain description	Antibiotic Resistance	Plasmid used	Source
CC-4533	cMJ030 (wild type)	none	none	Wildtype and parent strain to CLiP library
CC-1690	Wild type mating type +	none	none	Chlamydomonas Resource Center
LMJ.RY0402.107748	*key1-1*	Paromomycin	pMJ013b	CLiP mutant library
LMJ.RY0402.168949	*key1-2*	Paromomycin	pMJ013b	CLiP mutant library
CC-6226	*key1-1;RBCS1-Venus*	Paromomycin	pLM005-RBCS1	This paper; by mating the strains key1-1 (mt-) and RBCS1-Venus (mt+), which is generated by mating the strain RBCS1-Venus (mt-) in a cMJ030 background with the wild-type strain CC-1690 (mt+).
CC-6227	*key1-1;EPYC1-Venus*	Paromomycin, Hygromycin	pLM005-EPYC1	This paper; by transformating the plasmid pLM005-EPYC1 into *key1-1* strain.

bioRxiv preprint doi: https://doi.org/10.1101/2025.10.09.681382; this version posted October 10, 2025. The copyright holder for this preprint (which was not certified by peer review) is the author/funder, who has granted bioRxiv a license to display the preprint in perpetuity. It is made available under a CC-BY 4.0 International license.

CC-6228	*key1-1;KEY1-Venus*	Paromomycin, Hygromycin	pRAM118-pro+KEY1	This paper; by cloning and transformating the plasmid pRAM118-pro+KEY1 into *key1-1* strain.
CC-6229	*key1-1;KEY1-SNAP*	Paromomycin, Hygromycin	pRAM118-pro+KEY1-SNAP	This paper; by cloning and transformating the plasmid pRAM118-pro+KEY1-SNAP into *key1-1* strain.
CC-6230	*key1-1;RBCS1-Venus;KEY1-SNAP*	Paromomycin, Hygromycin	pRAM118-pro+KEY1-SNAP	This paper; by transformating the plasmid pRAM118-pro+KEY1-SNAP into *key1-1;RBCS1-Venus* strain.
CC-6231	*key1-1*;*RBCS1-Venus;KEY1$^{\Delta RBM}$-SNAP*	Paromomycin, Hygromycin	pRAM118-pro+KEY1_ΔRBM-SNAP	This paper; by cloning and transformating the plasmid pRAM118-pro+KEY1_ΔRBM-SNAP into *key1-1;RBCS1-Venus* strain.
CC-6232	*epyc1;EPYC1-Venus*	Paromomycin, Hygromycin	pRAM118-proEPYC1-EPYC1-Venus	This paper; by cloning and transformating the plasmid pRAM118-proEPYC1-EPYC1-Venus into *epyc1* strain.
CC-6233	*epyc1*;*EPYC1^{phosphonull}-Venus*	Paromomycin, Hygromycin	pRAM118-proEPYC1-EPYC1-Astring-Venus	This paper; by cloning and transformating the plasmid pRAM118-proEPYC1-EPYC1-Astring-Venus into *epyc1* strain.

1919